SEGMENTATION OF HUMAN MUSCLES OF

MASTICATION FROM

MAGNETIC RESONANCE IMAGES

NG HSIAO PIAU

NATIONAL UNIVERSITY OF SINGAPORE

2008

SEGMENTATION OF HUMAN MUSCLES OF

MASTICATION FROM

MAGNETIC RESONANCE IMAGES

NG HSIAO PIAU

(B. Eng. (Hons.), National University of Singapore)

A THESIS SUBMITTED

FOR THE DEGREE OF DOCTOR OF PHILOSOPHY

NUS Graduate School for Integrative Sciences and Engineering

NATIONAL UNIVERSITY OF SINGAPORE

2008

Acknowledgements

I would like to express my gratitude and sincere thanks to my supervisors and members of my Thesis Advisory Committee, Assoc. Prof. Kelvin Foong Weng Chiong, Assoc. Prof. Ong Sim Heng, Prof. Wieslaw Lucjan Nowinski and Dr. Goh Poh Sun for their guidance and support, without which my research work would not have been initiated and developed.

I would also like to express my sincere thanks to the staff at the Department of Diagnostic Imaging, National University Hospital (NUH) for the kind assistance and advice in the data acquisition process. In particular, I would like to thank Mr Christopher Au C.C., principal radiographer at NUH, for his guidance and support during my internship at the hospital. Many thanks are extended to Mr. Francis Hoon, laboratory officer at Vision and Image Processing Laboratory, and Ms. Aminah Bivi, secretary to Prof. Nowinski, for the assistance rendered during my candidature.

Finally, I would like to express my gratitude to Agency for Science, Technology and Research, Singapore (A*STAR) for awarding me the A*STAR Graduate Scholarship and providing me with the financial support throughout my candidature. Special thanks goes to the directors and staff at A*STAR Graduate Academy for their support and encouragement.

Table of Contents

Summary

With rapid advances in medical imaging technology, the use of magnetic resonance (MR) and computer tomography (CT) image data for maxillofacial surgery has become increasingly common. CT data permit clinicians to study the jaws while MR data allow clinicians to study and quantify the human masticatory muscles which are of interest as they directly affect one's ability to chew effectively and efficiently. Despite their importance, it has been observed that many currently available pre-surgical facial models do not provide information such as the actual shape, size and location of the human masticatory muscles.

Segmentation is an essential step in image processing and analysis. Before quantification can be carried out, segmentation of the targeted object has to be performed. Furthermore, numerous segmentations would have to be done before accurate statistical models can be built. A common practice by clinicians is to manually segment all the image slices in the MR datasets before carrying out quantification and analysis of the human masticatory muscles. However this is a highly time-consuming and inefficient process.

The main focus of this thesis is to present methods for segmenting the human masticatory muscles from MR images. Segmenting them is a challenging task due to the close proximity between the muscles and their surrounding soft tissue, as well as the complicated structure of the muscles. Hence we studied 2D followed by 3D segmentation techniques for the masticatory muscles.

An improved watershed segmentation algorithm with unsupervised clustering was first introduced to address the drawbacks of the conventional watershed algorithm. The improved watershed segmentation algorithm addresses the over-segmentation problem posed by the conventional algorithm by performing thresholding on the gradient magnitude image and post-segmentation merging to merge the initial partitions formed by the watershed transform. The use of GVF snake was also studied in a proposed model-based method which comprises of a process to provide good initializations to the GVF snake automatically, while in another proposed method, adaptive morphology was introduced to preserve the muscle structure. The proposed methods were implemented and the consistencies between segmentation results and ground truth were checked.

In a 3D MR dataset, there are image slices where no clear boundary exists between the muscle and the surrounding tissue. As such, we will need to make use of the neighbouring slices which provide additional information. Dominant slices which together best capture the shape and area features of the muscles were determined and patient-specific muscles models were built using them. 2D segmentations of the muscles are carried out only on the dominant slices before shape-based interpolation is used to build the patient-specific models. The segmentation results were validated against ground truth provided by an expert radiologist who has more than 15 years of clinical experience. Quantifications of the segmented muscles volume were also carried out.

List of Tables

List of Figures

Chapter 1

Introduction

1.1 Introduction

This thesis presents methods for segmenting the human masticatory muscles from magnetic resonance (MR) images of the human head. In general, maxillofacial surgeries are carried out to provide patients a better quality of life by correcting facial anatomic abnormalities. Maxillofacial surgery combines orthodontic treatment with surgery of the jaw to correct or establish a stable, functional balance between the teeth, jaws, and facial structures. The facial bones commonly corrected during maxillofacial surgeries are the mandible (lower jaw) and maxilla (upper jaw). The muscles of interest are the masticatory muscles, which include the masseter, lateral and medial pterygoids, as well as the temporalis.

The masticatory muscles [1] directly affect one's ability to chew. The large masseter muscle is the strongest jaw muscle and acts to raise the jaw and clench the teeth. The masseter's broad origin and insertion allow it to apply chewing force over a broad area. When the masseter muscle is functioning, its fibers shorten and help to shift the mandible upwards during the chewing cycle. When the masseter muscle contracts, it elevates the mandible, closing the mouth. The pterygoid muscles, used in various combinations, can elevate, depress, or protract the mandible, or slide it from side to side. At the base of the skull, a part of the sphenoid bone (which houses the sinuses) are the pterygoid plates. The pterygoid muscles are attached to them. The lateral

pterygoid muscle originates on the lateral side of the lateral pterygoid plate. The inferior head pulls the condyle forward and helps protrude and depress the mandible while the superior head of the lateral pterygoid functions primarily in the biting action. Unlike the lateral pterygoid, the medial pterygoid originates on the medial side of the medial pterygoid plate, and it provides the slight lateral shift of the mandible during chewing. When the medial pterygoid contracts, the mandible is elevated and the mouth is closed. Other than the masseter and the pterygoids, human masticatory muscles also comprise the temporalis muscle. This muscle has a very wide origin from the entire temporal fossa and the fascia covering the muscle. Its fibers insert into the coronoid process of the mandible. When the entire muscle contracts, the overall action pulls up on the coronoid process, which results in the mandible being elevated and the mouth closed.

Traditional pre-surgical planning for maxillofacial surgeries was carried out using profile tracings (Figure 1.1(a)), photographs and lateral cephalograms (Figure 1.1(b)). These records are 2D in nature and do not allow clinicians to visualize the human masticatory muscles. With rapid advances in medical imaging technology in recent years, the use of 3D maxillofacial image data has become increasingly common. Computed tomography (CT) and magnetic resonance (MR) data are currently available to aid clinicians in their pre-surgical planning. CT and MR data are volumetric data, and comprise a stack of 2D sequential images. The main advantage which volumetric data has over surface data is that it delivers internal information of an object and allows clinicians to perform 3D analysis. For example, a CT data set which comprises a series of 2D cross-sectional images of the head will provide clinicians with information on the jaws of the patient.
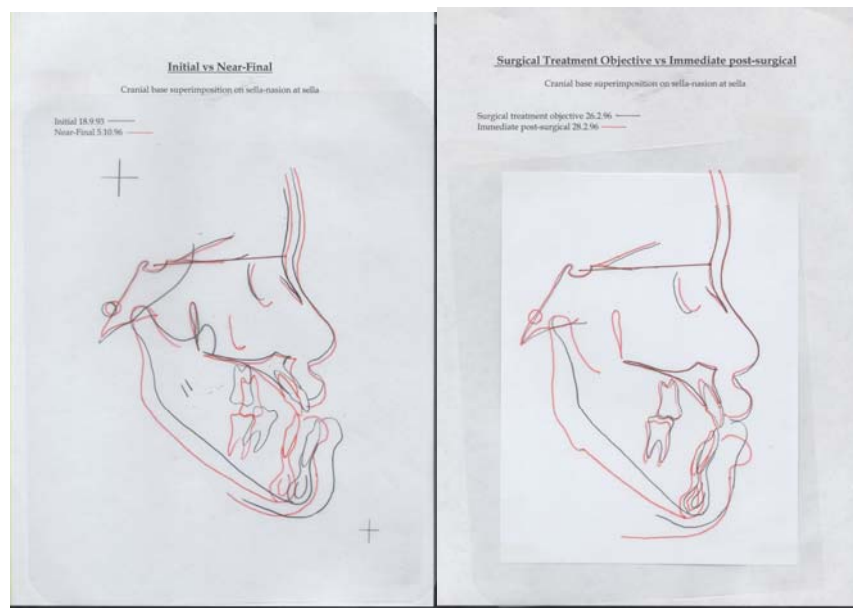
(a)
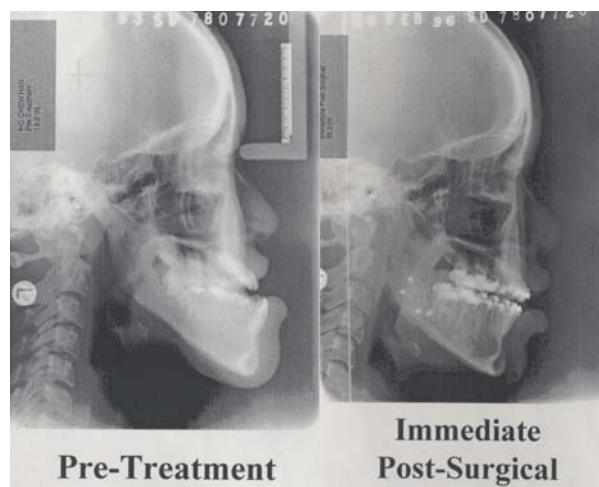
(b)

Figure 1.1: (a) Cephalometric tracings, (b) Lateral cephalogram of patient.

Along with the availability of volumetric data, clinicians are now able to visualize the facial bones and human masticatory muscles in 3D during pre-surgical planning. They are also able to carry out quantifications such as measurements of the volume and

surface area. Manual contour tracing, which can be a time-consuming process, is carried out by clinicians before quantifications are done. To aid clinicians in their diagnosis of patients and surgical planning, computerized systems are designed to facilitate the analysis of 3D data and pre-surgical simulations.

In the following sections of this chapter, examples on current facial models and description of their drawbacks are provided. A description on the contributions of the work presented in this thesis is also provided.

1.2   Previous work on pre-surgical planning

Early research work on facial models was based on geometric deformations using parametric surfaces and aimed primarily at facial animation. Physically based simulation paradigms were then adopted to model the physical properties of the elastic materials more accurately. Physically based facial models have been known to provide more realistic face models and better accuracy than pure geometric models because they express the human face as an elaborate biomechanical system. The use of such physically based models has made it possible to synthesize more natural facial models from dynamics or kinetics evaluation.

Example of an early work on physically based facial model is one which combines, unifies, and extends various methods from geometric modeling, finite element analysis, and image processing to render highly realistic models [2]. Facial surface and soft tissue data are extracted from CT scans of individuals. After which, a finite element model of the facial surface and soft tissue is provided, which is based on

triangular finite elements. Another physically based facial model can be found in [3] which present a prototype of a facial surgery simulation system for surgical planning and the prediction of facial deformation. Similar to [2], the head model consists of soft tissue and the skull, constructed from the 3D CT patient data. The skull layers are segmented from 3D CT data by thresholding. The skin layer is a wire-frame model which is regarded as an elastic body. The soft tissue is modelled using nonlinear springs, which are attached from the skull layer to the skin surface.

More realistic physically based facial models have been proposed more recently. A biomechanical model of the human face, which comes with a multi-layer structure, incorporating a physically based approximation to facial skin, a set of facial muscle actuators, and underlying skull structure, was presented in [4]. The skin model uses a kind of non-linear spring to directly simulate the dynamic deformation of the facial skin. Force-based facial muscle models are created to simulate the distribution of the muscle force applied on the skin surface. This facial model is more realistic as compared to previous facial models, and is efficient in facial animation and expression synthesis applications. Along with the improvements in facial animation models, there were also advancements in the area of pre-surgical facial models. Koch et al. constructed a 3D physically based facial model from CT and laser range scans [5]. The concept of 3D volumetric elasticity is being applied in the construction of the model to allow the representation of important volumetric effects such as incompressibility in a natural and physically accurate manner. Another recent physically based facial model used for pre-surgery simulation was developed by Gladilin *et al.* and used for static soft tissue prediction and muscle simulation [6]. This model uses the linear elastic

modeling approach to simplify the highly complicated biomechanical behavior of different tissue types. In this model, it has been assumed that different tissue groups have similar properties. Another model developed using similar concepts can be found in [7].

A more recent pre-surgical facial model is in [8], where a laser range scan provides a photorealistic 3D model of the patient's face and a CT scan provides a 3D representation of the patient's skull. These data sets are used to generate triangulated models of the patient's face and bone structure. A mesh is generated for both the bone and soft-tissues using the Marching Cubes algorithm [9]. Both the CT and laser data sets are registered via the selection of corresponding cephalometric landmarks of the phtotorealistic face surface obtained by the laser range scanner and the untextured face surface taken from the CT scanner. Basic components of the soft-tissue model are mass points and springs, which connect these mass points. The model enables the representation of multi-layer soft tissue with differential elasto-mechanical properties. At any instant of time, the motion and deformation of the mesh is described by a system of second-order differential equations, each expressing the motion of a node. In surgical simulation, the external forces are applied at these nodes by simulating interactions with surgical instruments. Another example of a facial model which made use of CT data is in [10]. A 3D reconstruction of the whole skull was established from CT data, together with a mesh representing the CT soft tissues. Laser scanned images provide a textured surface for the model. The soft tissue mesh is deformed correspondingly as the bone segments are being shifted. This model did not take into consideration the anatomy of the masticatory muscles. The same situation was

encountered in the surgical model used for correction of facial asymmetry which was presented in [11]. The emphasis in this surgical model has been placed on the skull.

Many pre-surgical facial models incorporated information from CT data. An example of a pre-surgical facial model which does not make use of CT data is in [12]. This simulation system integrated the morphological data of a patient's teeth, jaw and face. It combines laser scanned data of face and teeth onto the coordinate system of the cephalogram using the projection matching technique. The patient's mandibular shape was simulated on the computer display by transforming a generic model, used as a template, till it matches that of the patient's cephalogram.

1.3   Problem statement

The primary inadequacy with existing pre-surgical facial models is that they do not incorporate the actual location, shape and size of the masticatory muscles. This could be because the models were constructed using mainly CT data which does not clearly display the anatomy of the human masticatory muscles as we will see in Chapter 2. Segmentation is a key step to the building of accurate muscles models. The focus of the work presented in this thesis is to provide computerized techniques for segmentation of human masticatory muscles which will facilitate the building of accurate muscles models for future integration into current available pre-surgical facial models.

In the process of a maxillofacial surgery, surgeons will first detach the masticatory muscles from the bone before making adjustments to the bone. After which, they will

attach the masticatory muscles back on to the bones. Hence the availability of information on actual location, shape and size of the masticatory muscles would be instrumental in helping maxillofacial surgeons to have a better understanding of the mastication system of the patient during surgical procedures concerning the jaws.

In many medical imaging applications, various parts of the anatomy have to be segmented from medical image sets and segmentation plays an important role in biomedical image processing [13]. Though the masticatory muscles may be seen in MR scans of the patient, segmentation of them have to be carried out before clinicians can visualize them in 3D and measure important quantities such as their volume and surface area. As mentioned earlier, there is also a need to carry out segmentation before models of the masticatory muscles can be built. Currently, the segmentation process is done manually and clinicians have to go to every image slice and mark out the boundaries of the muscles [14 – 18]. This is an extremely time-consuming process. We seek to develop segmentation techniques to aid clinicians in the segmentation of human masticatory muscles and reduce the amount of time taken. To our knowledge, though techniques for segmenting limb muscles are available [19], segmentation techniques for the masticatory muscles are currently unavailable. A key challenge here is the close proximity and fuzzy boundaries between the masticatory muscles and surrounding soft tissue.

1.4   Objectives

The main focus of our research work is on developing techniques for segmenting the human masticatory muscles from MR data. But before that, we carried out research work on the extraction of both skull and surface information from CT data, as it was

observed that many facial models make use of CT data for skull information and laser scans for surface information [8 – 10]. This is inefficient and the facial and CT scans may have different resolution which may hinder the integration and accurate diagnosis. Though this is not the main focus of our thesis, introducing this method will facilitate future work of creating a more realistic pre-surgical facial model which incorporates the information of the human masticatory muscles with the skull and surface information.

The segmentation of the skull, and in particular the mandible, is an important step for maxillofacial surgery. For instance, the comparison of pre- and post-surgical assessment of mandibular asymmetry is considered to be an appropriate means of determining the effectiveness of maxillofacial surgery [20].

After designing a method which allows clinicians to extract skull and surface information from CT data, we looked into developing techniques for segmenting masticatory muscles from MR data. This is a challenging task due to the close proximity between the muscles and their surrounding soft tissue, as well as the complicated structure of the muscles. Hence we studied 2D followed by 3D segmentation techniques for the masticatory muscles.

As such, the second objective of this thesis is to perform segmentation of the masticatory muscles from 2D MR images. For this purpose, we first explore the use and improve the watershed segmentation algorithm [21]. The watershed segmentation technique has many applications in medical image segmentation [22] and is useful for segmenting objects which do not have clear boundaries between them [23]. Despite the

usefulness of the watershed segmentation algorithm, there is presence of over-segmentation in the segmentation results produced using it. In the process of our work, we aim to minimize this problem. In addition to the watershed segmentation algorithm, we studied the use of the snake model, which is another popular technique that has been used extensively and found to be suitable for MR image segmentation [24, 25]. We explore the use of the gradient vector flow (GVF) snake [26] to segment the masticatory muscles from 2D MR images. GVF snake has its own disadvantages. When a poor initialization to GVF snake is used, it may not converge to the desired boundaries. Another concern is the computation time required for the GVF snake to arrive at its final convergence. Hence in our work, we aim to provide good initializations to the GVF snake automatically and reduce the amount of computation time. We also experimented with the use of GVF snake for segmentation of the temporalis. As the results were less than ideal, another method, which comprises of various image processing techniques, was proposed to perform the task.

The structures of human masticatory muscles are generally complex and the close proximity between the muscles and their surrounding soft tissue, which has relatively similar gray levels, make the task of 3D segmentation of the muscles a difficult one. We make use of patient-specific models to facilitate the segmentations. Hence, the third objective in this thesis is to create patient-specific masticatory muscles models. Shape-based interpolation [27, 28] is one of the popular techniques commonly used for modelling in medical imaging applications and we will make use of it to build patient-specific masticatory muscles models. It is extremely time-consuming if the clinician has to manually segment the muscles from most, if not all, of the all slices in a MR data set. Hence the key issue which we are addressing under this objective is to devise

a method to identify the slices where manual segmentations have to be carried out in order for accurate models to be built. Depending on the complexity of the structure, the number of slices required may be a small fraction of the total number of slices in the data set.

Having built the patient-specific masticatory muscles models, the fourth objective of the thesis is to develop a technique which incorporates the information from the models to facilitate the segmentation of the muscles. Model-based segmentation is increasingly being adopted in medical image segmentation as they incorporate prior knowledge which facilitates segmentation [29 – 31].

The last objective of this thesis is to perform quantification of the segmented masticatory muscles. MR data sets from normal subjects are used in our work.

1.5   The thesis

In this section, an overview of the thesis is provided in order to give the scope of each chapter. The thesis consists of 7 chapters, including this introductory chapter.

In Chapter 2, we introduce the imaging modalities used in our work. We segment the skull and surface information for CT data. However, there is hardly any visible boundary between the masticatory muscle regions and the surrounding soft tissue in CT data. Hence we made use of MR data for segmentation of the masticatory muscles. There are various sequences and parameters involved in MR data acquisition. We

provide sample MR images acquired using different parameters and we introduce the selected imaging sequence used in our work.

In Chapter 3, we introduce our proposed method which facilitates the extraction of the skull and surface information from CT data. Clinicians commonly depend on facial scans for the surface information and CT data for skull information. This is unlike our proposed method which is able to extract skull and surface information from CT data.

In Chapter 4, we introduce an improved watershed segmentation algorithm which addresses the over-segmentation problem posed by the conventional algorithm by performing thresholding on the gradient magnitude image and post-segmentation merging to merge the initial partitions formed by the watershed transform. We further addressed the problem by making use of K-means clustering to reduce the presence of fine textures in the image before applying the improved watershed algorithm to the resulting image. Besides the watershed segmentation algorithm, GVF snake is also applied to segment the human masticatory muscle from MR slices. Anisotropic diffusion [32] was used to smoothen the highly textured image. Correlation between a template of the targeted muscle, which was obtained from the manual tracings, and the smoothened image is then checked. This provides an initial segmentation. It serves as initialization to the GVF snake which iterates to arrive at the final segmentation. For segmentation of the temporalis, thresholding is employed to roughly remove the unwanted components. Adaptive morphological operations are then applied to first remove the brain tissue, followed by the removal of the other soft tissues surrounding the temporalis.

In Chapter 5, we propose a method for determining dominant slices of each masticatory muscle in a MR data set. We define dominant slices to be the MR slices that together are representative of the muscle shape. In the training sets, the masticatory muscles were first manually segmented by an expert radiologist. From these training sets, we determine the locations of the dominant slices for each of the muscles using a set of criteria which best captures the main features of the muscle shape. Given a test set, we obtain patient-specific models for each of the muscles by carrying out 2D manual segmentation of the muscle from the dominant slices and using shape-based interpolation to create the muscle model from them.

In Chapter 6, we present methods which incorporate information from the patient-specific models to segment the human masticatory muscles from MR data sets. The patient-specific models serve as coarse segmentations which we refine by matching distributions of the pixels' intensity values. The segmentation results were validated against ground truth provided by an expert radiologist who has more than 15 years of clinical experience. Quantifications of the segmented muscles volume were then carried out.

Finally, in Chapter 7, we give an overview of our achievements together with recommendations for future work.

Chapter 2

Data Acquisition

2.1 Introduction

CT data has been widely employed for craniofacial and maxillofacial surgery. It provides 3D information of the jaw without geometrical distortion [33]. It can be used for computation of geometric parameters of movement to determine the curvilinear distractor dimensions required to correct mandibular deformities [34]. It is also commonly used in pre-surgical planning as well as for navigation purposes during surgery [35 – 37].

MR imaging is increasingly being used in clinical treatment for dental patients. For example, MR imaging was used in the evaluation of patients with occult submucous cleft palate and information obtained was used to aid in the treatment decision [38]. In another example, MR imaging was used in the clinical diagnosis for a patient who suffers from malocclusion and who had been diagnosed with Simpson-Golabi-Behmel syndrome, which causes general overgrowth in height and weight [39]. In a more recent clinical study [40], it was suggested that MR imaging is useful in the evaluation of soft tissue changes that occur in the temperomandibular joint after acute condylar trauma.

The data used in our work was acquired at National University Hospital Department of Diagnostic Imaging using CT and MR (symphony maestro class with quantum gradients) scanners from Siemens (Figures 2.1 and 2.2).

Figure 2.1: CT scanner.

Figure 2.2: MR scanner.

2.2 Selection of imaging modalities

CT data is commonly used by clinicians who wish to analyze the jaws and skull of the patients [33 – 37]. Comparing the CT image in Figure 2.3 and the MR image in Figure 2.4, it can be observed that the bony regions in a CT image are easily visible as they have higher gray levels. In contrast, it is difficult to accurately delineate the bony regions in a MR image. Hence in the work presented in this thesis, we make use of CT data for extracting the skull.
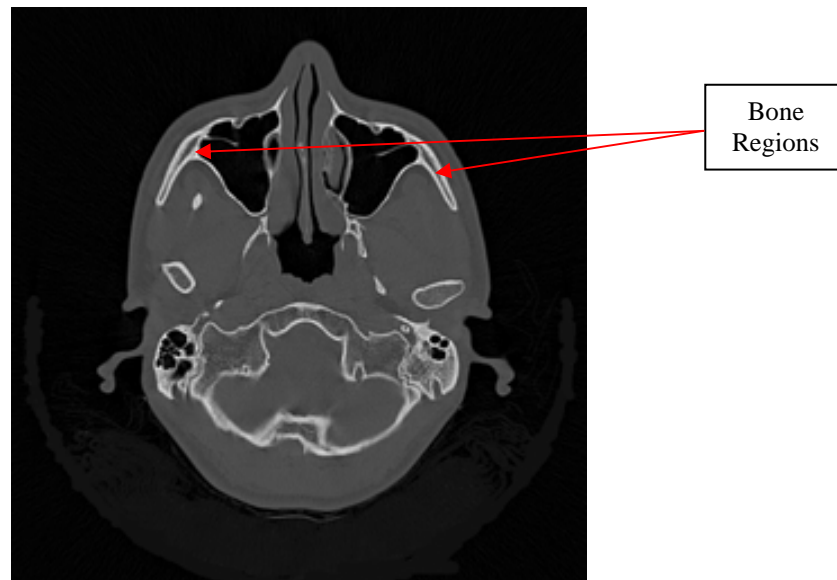
Figure 2.3: CT image with identified bone regions.

Figure 2.4: MR image with identified bone regions.

In some clinical studies such as [16], clinicians make use of CT data to carry out their studies on the volume and shape of the masticatory muscles. However, it can be observed that in a CT image (Figure 2.5), the masticatory muscles hardly have visible boundaries with the surrounding soft tissue. In contrast, it can be observed in a MR image (Figure 2.6) that there are visible boundaries between the masticatory muscles.

Clinicians who used CT data to analyze the masticatory muscles have to make use of manual contour tracing to segment the muscles and this is very time-consuming. Furthermore, it was reported in [41] that MR imaging is able to provide accurate 3D images which allow diagnosis of lesions within the masseter muscle. In contrast, these clinicians found it difficult to diagnose on CT data. Therefore, in our work here, we make use of MR images for segmentation of the human masticatory muscles.

Figure 2.5: CT image with identified masseter regions.

Having decided on MR imaging as the imaging modality for human masticatory muscles in our work, we have to decide on the imaging sequence to use. We explored a number of imaging sequences which included fast spin echo (FSE), gradient recall echo (GRE), spoiled gradient recall (SPGR) and fast low angle shot (FLASH). Figures 2.4 and 2.6 show MR images acquired using the T1 FLASH sequence and Figure 2.7 the images acquired using FSE, GRE and SPGR sequences. The T1 FLASH images are clearly superior in displaying the anatomy of the human masticatory muscles. Hence, in our work here, we acquired MR data using T1 FLASH (240mm FOV, TR=9.93ms, TE=4.86ms). This was done using a 1.5T MR scanner.
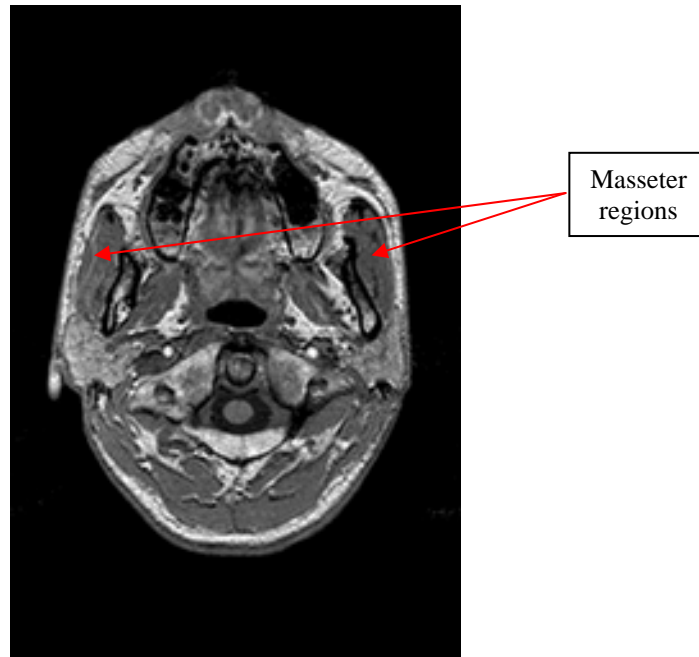
Figure 2.6: MR image with identified masseter regions.

Though the selected MR imaging protocol is capable of displaying the anatomy of the human masticatory muscles, it should be noted that geometric distortion of the anatomy might be present in the MR data. Such distortion can occur due to magnetic susceptibility artifacts [42] and partial volume effects [43], among other factors. Magnetic susceptibility artifacts occur due to the different magnetic susceptibilities of different tissues which cause de-phasing and frequency shifts that result in image artifacts. Partial volume effects are due to the limited spatial resolution during imaging and the size of the image voxel is larger than the size of the feature to be imaged. Further description on the physical background and reduction strategies for MR image artifacts is in [44]. In addition, there are earlier works which ascertain the geometric accuracy of MR data. A previous study was carried out to determine whether MR data has sufficient geometric accuracy to allow implant planning based on it [45] and in another study, morphometric measurements of cadeveric lumbar spine obtained from MR data were compared against those obtained from the physical specimen [46]. As the emphasis of this thesis is on development of segmentation techniques for

segmenting the masticatory muscles, no experiments are performed to ascertain the geometric accuracy of the MR data here.
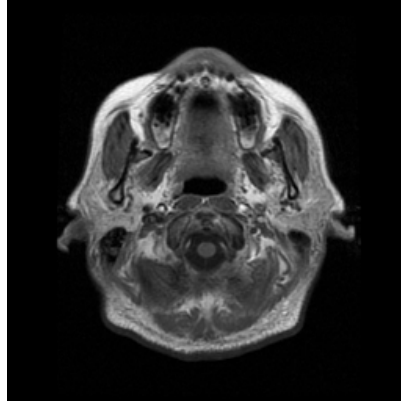
(a)
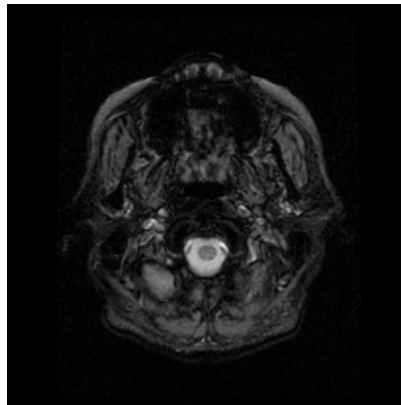
(b)
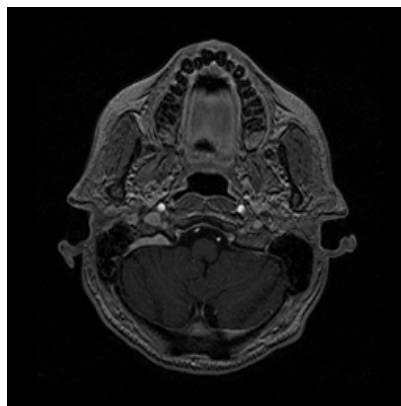
(c)

Figure 2.7: MR images acquired using (a) T1 weighted FSE,

(b) T2* weighted GRE, (c) T1 weighted SPGR.

2.3   Data acquisition time

The time taken to acquire each MR data set is a factor which we took into account in the data acquisition process as human subjects are involved. A longer scan time meant that there is a higher possibility of the subject moving thus resulting in motion artifacts. It took around ten minutes to acquire a MR data set from the mandible to the region just cephalad to the pinna and in order to scan the entire head, which includes the mandible and the entire brain, it took about fifteen minutes. The fifteen minute scan captures four masticatory muscles: masseter, lateral pterygoid, medial pterygoid and temporalis. But it is difficult for the subjects to remain stationary for the entire fifteen minutes. Using the ten minute scan, we were unable to capture the entire temporalis. However, the image quality was better with fewer motion artifacts. In our work here, we make use of data sets acquired using ten minute scans.

Chapter 3

Analysis of CT data

3.1   Introduction

In this chapter, we deal with three-dimensional volumetric CT. The CT data used in our work here comprises a series of 2D images that exhibit axial cross-sections of the head. A CT image is a pixel map of the X-ray attenuation coefficient of the tissue within a cross-sectional plane. CT data is especially suitable for visualizing high-density objects such as bones and clinicians commonly make use of it to extract skull information. A skull has to be extracted from CT data for the applications in craniofacial surgery that are concerned with the anomalies of the head and facial bones.   In addition to skull information, clinicians have to analyze the surface information of patients during diagnosis.

It is observed that most clinicians commonly rely on facial scans and CT images, for surface and skull data respectively, in their diagnosis of patients. Such a practice may not be efficient. After identifying the area of interest from the facial scan, medical practitioners will still have to go through the process of locating the corresponding CT slices from the CT set. Furthermore, the facial and CT scans may have different resolution and this may hinder accurate diagnosis.

We introduce a process which includes extraction of both the skull and surface data from the CT slices, and construction of 3D geometric model which medical practitioners can depend on in their diagnosis of patients.

3.2 Overview of proposed method

Our proposed method (Figure 3.1) involves the use of thresholding for extracting the skull. For extraction of the surface data, thresholding is first used to extract the background followed by edge detection to extract the surface data. An arithmetic addition is performed to add the extracted skull data and extracted surface data together before applying volume rendering to construct the 3D model.
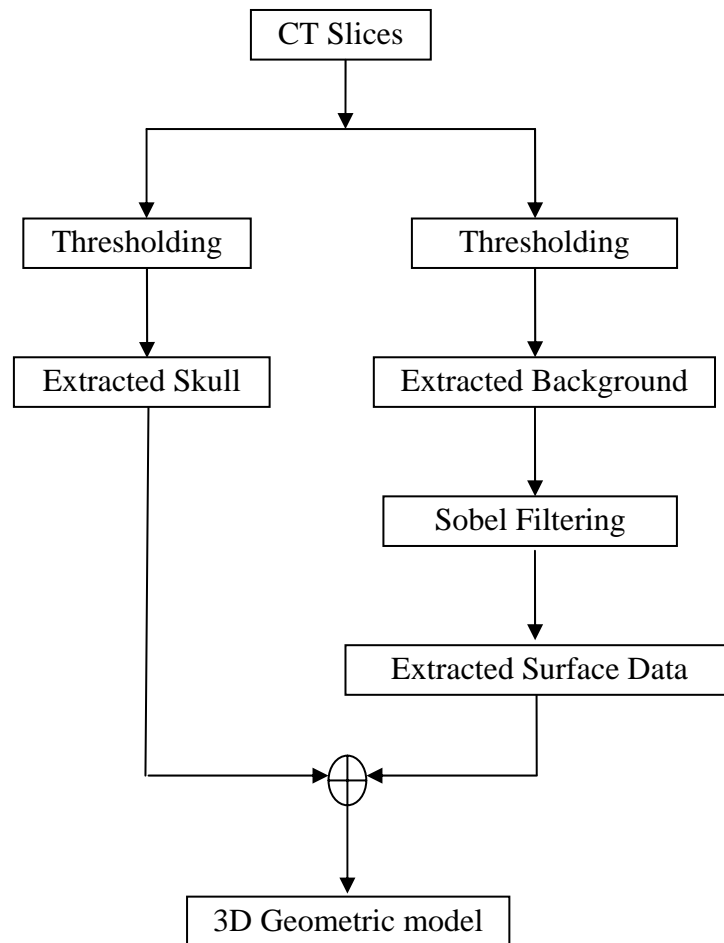
Figure 3.1: Flow-chart of proposed method.

3.3   Extraction of skull

Extraction of the skull in our proposed method is done using thresholding. Thresholding is traditionally used for extraction of a skull [47] and it is effective because the bone has higher Hounsfield number than the muscles, fats and tissues. A CT slice with its corresponding histogram are as displayed in Figure 3.2.

(a)
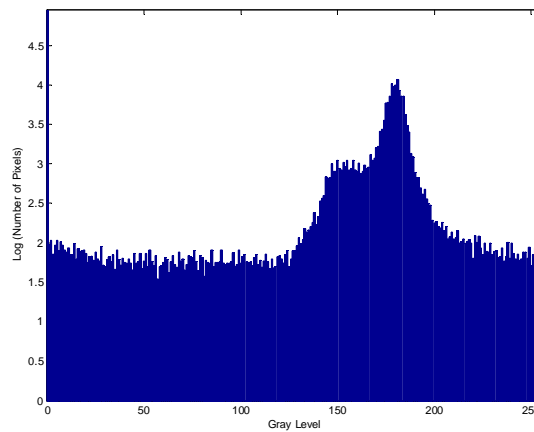
(b)

Figure 3.2: (a) A sample CT image, (b) Corresponding histogram of image.

From the histogram in Figure 3.2(b), it can be observed that the CT image consists of pixels with relatively low intensity values and relatively high intensity values, which implies that these pixels belong to the background and the bone respectively. In our early work [48], we did a manual selection of the threshold value after observing the histogram and successfully extracted the skull. The Otsu method is able to produce similar results. A sample of the extracted skull from the CT slice in Figure 3.2(a) is in Figure 3.3.

Figure 3.3: Extracted skull of CT slice.

We did a simple test to check if the skull has been satisfactorily extracted. An arithmetic subtraction is performed to subtract the extracted skull data (Figure 3.3) from the original CT slice (Figure 3.2) and the result is as displayed in Figure 3.4. Comparing Figure 3.4 with Figure 3.2 visually, it can be observed that the bright regions (skull data) in Figure 3.2 have been fully subtracted away, leaving behind only the darker regions.

Figure 3.4: CT slice with skull data subtracted.

3.4   Extraction of surface information

Instead of making using facial scans to obtain the surface data, which is usually done, we will extract the surface facial data from the CT scan in a two-step process. The first step involves using the extraction of the background using thresholding. There are a number of techniques to determine a proper threshold value [49]. We have employed the Otsu method because of its reliability and computational efficiency [50]. The otsu threshold value determined by the method for the CT slice in Figure 3.2 is 93 and the extracted background is as shown in Figure 3.5.
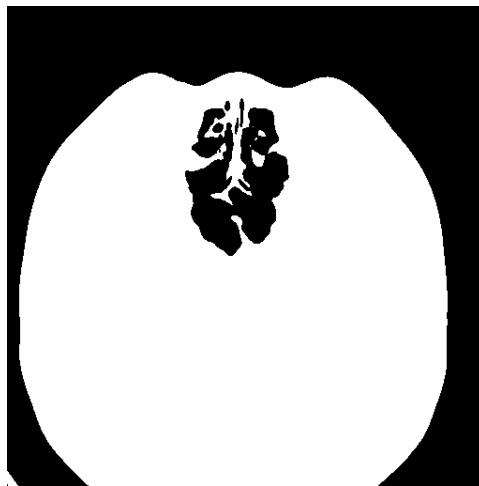
Figure 3.5: Extracted background of CT slice.

After extracting the background of the CT slice, the next task will be to obtain the surface data from the extracted background. This is achieved by making use of the 3×3 Sobel filter to obtain the edges of the extracted background. Sobel filtering is preferred because the Sobel operstors have the advantage of providing both a differencing and a smoothing effect [51]. Since derivatives enhance noise, the smoothing effect is a particularly attractive feature of the Sobel operators. The extracted surface data obtained after performing Sobel filtering on the image in Figure 3.5 is displayed in Figure 3.6.
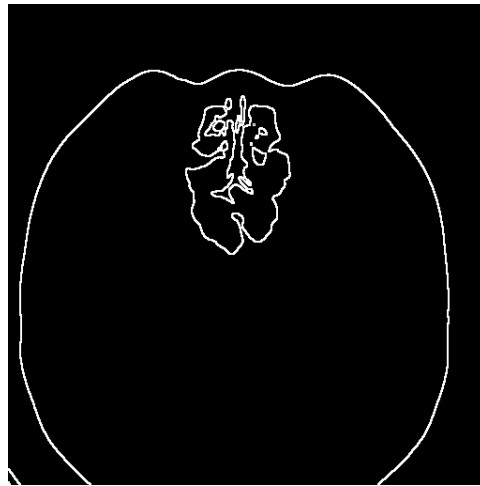
Figure 3.6: Extracted surface data of CT slice.

An arithmetic addition is performed to add the extracted skull data (Figure 3.3) and extracted surface data (Figure 3.6) together. The resulting image is in Figure 3.7.

Figure 3.7: Extracted skull and surface data of CT slice.

3.5   3D Reconstruction

Surface rendering and volume rendering are two popular techniques to render objects in 3D. Surface rendering treats the object as having a surface of a uniform colour, while volume rendering directly displays a sampled 3D scalar field without first fitting geometric primitives to the sample. Volume rendering [52] is preferred to surface rendering here because the latter requires high quality scan and excellent skull extraction to show clean edges. An example of a reconstructed 3D volumetric model obtained through volume rendering is as displayed in Figure 3.8.
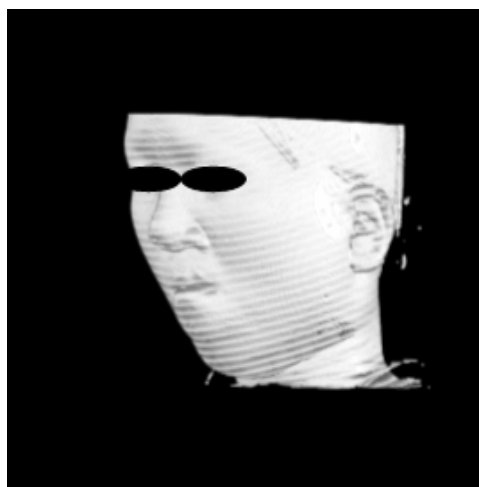
Figure 3.8: Reconstructed 3D geometric model.

3.6 Results and discussion

The CT data set (512 x 512; 1mm thickness) of a patient is being used to validate the effectiveness of the proposed process. The skull and surface data is first extracted from all the CT slices, after which, the 3D volumetric model is constructed. The resulting 3D model is as presented in Figure 3.9, with increasing opacity. The actual profile of the patient is as shown in Figure 3.10.
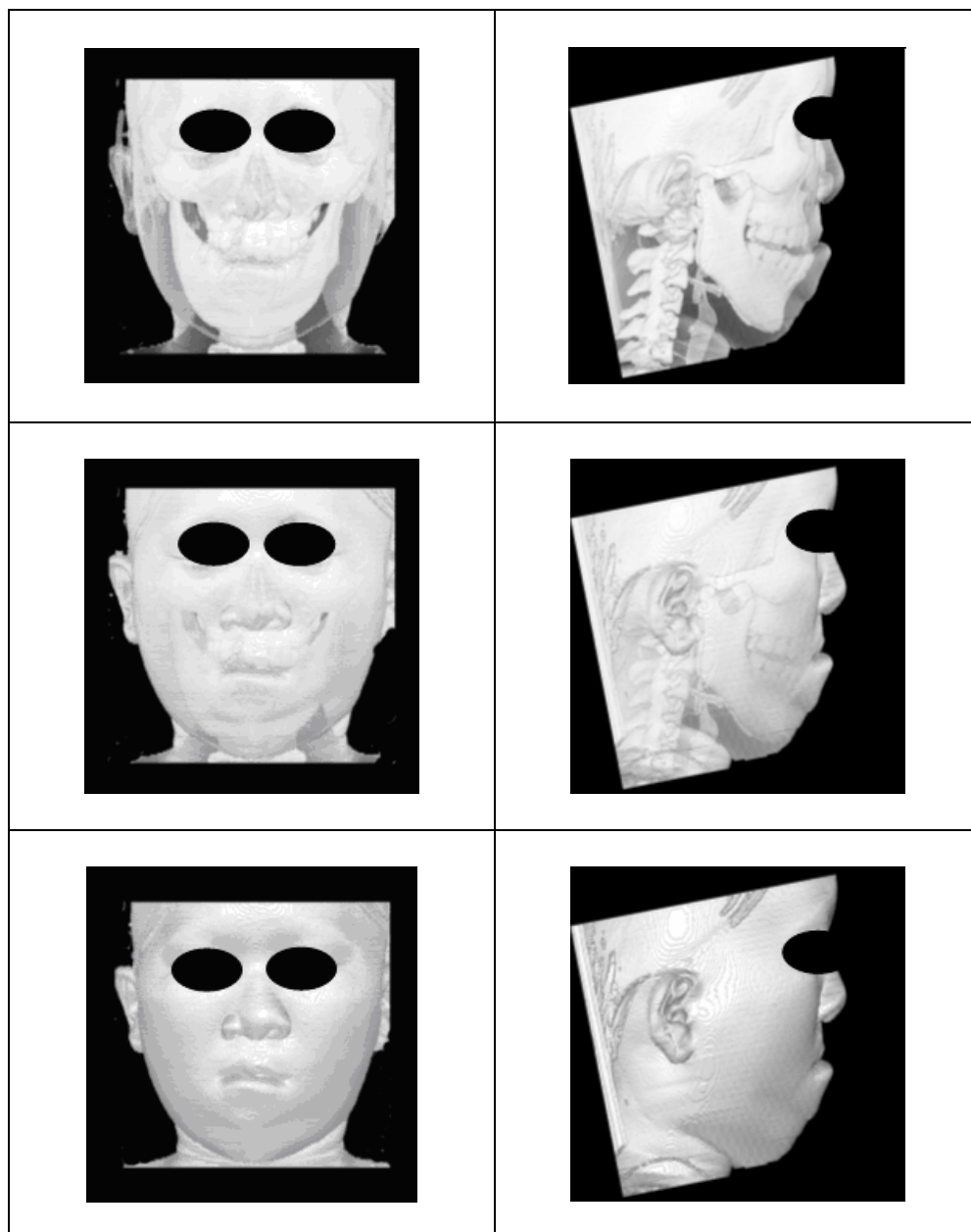
Figure 3.9: 3D Geometric models with varying opacity.

By varying the opacity of our 3D volumetric model, medical practitioners can choose to view the data of interest more clearly. With low opacity, the skull can be observed clearly but not the surface data, and when set to high opacity, the surface data can be observed clearly but not the skull.

(a)   (b)
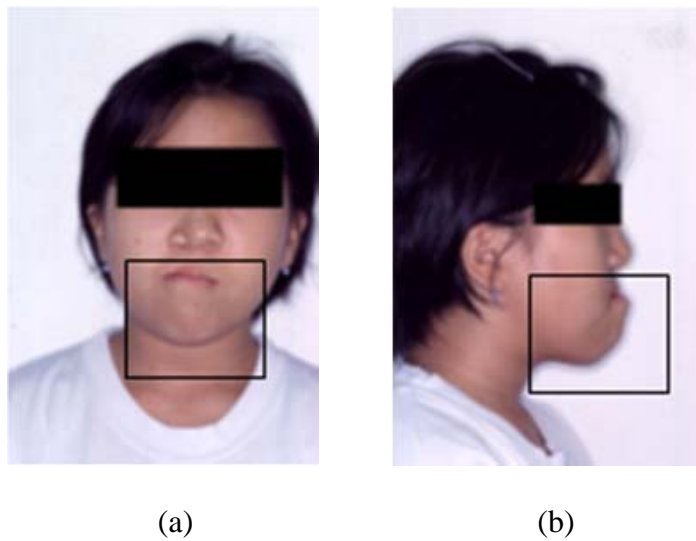
Figure 3.10: (a) Frontal and (b) Profile photos of a patient.

We make a comparison between the 3D virtual human head in Figure 3.9 and the actual profile of the patient in Figure 3.10 visually, to determine if the 3D model constructed is accurate. It is observed that 3D model that we constructed is similar to the actual profile of the patient. From the profile, it can be observed that the patient is suffering from facial problem, but it is not possible to view the area of interest of the skull. However, based on the 3D model that we constructed, we are able to observe that this patient suffer from restriction of growth in the upper jaw that give rise to flattened facial appearance. The growth of the lower jaw however is normal.

From the 3D model that we have reconstructed, it is possible to observe both the skull and surface data. However, this may still not be a true representation of the human head because the human head also consists of various muscle groups and tissues. Medical practitioners will need to make use of Magnetic Resonance Imaging (MRI), which uses a magnetic field and pulses of radio wave energy, to provide images of the masticatory muscles and facial tissues.

There has been on-going research to develop physical models of facial tissue and muscle articulation. One of the earliest facial models was developed by Waters and Terzopoulus [53]. Under that facial model, a tissue model is represented by a lattice of non-linear spring units with carrying visco-elastic properties. In more recent research [54], a generic 3D Finite Element Model of the face soft tissues was developed to describe the continuous mechanical behavior of the soft tissues. Despite continued efforts in development of pre-surgical facial models, it can be observed that there is a primary inadequacy in that these models do not take into account the location, shape and size of the human masticatory muscles which play a key role in one's ability to chew and smile.

The importance of the human masticatory muscles provides us with motivation to develop techniques for patient-specific modelling and segmentation of the human masticatory muscles which we will introduce in subsequent chapters.

Chapter 4

Segmentation techniques for MR slices

4.1 Introduction

Segmentation is an important component of image analysis. It is essential for successful automated analysis of biomedical images and is a crucial step in numerous clinical and research applications, including three-dimensional visualization, volumetric measurement, image-guided surgery, radiotherapy planning and detection of changes over time. The detection of lesions and abnormalities is important for medical diagnosis, e.g., the segmentation of tumors from MR images.

There are several common approaches for medical image segmentation and some examples are provided here. Thresholding is a simple yet often effective means for segmentation of images in which different structures have contrasting intensities. Connectivity-based thresholding finds a boundary between two regions using the path connection algorithm and changing the threshold adaptively [55, 56]. A major limitation of thresholding is that it does not take into account the spatial characteristics of an image and thus is sensitive to the noise, artifacts and intensity inhomogeneities that can occur in MR images. A recent approach, supervised range-constrained thresholding, uses prior knowledge to confine the analysis to the histogram of the region of interest (ROI). It has been applied to MR images and is able to give a good solution despite poor image quality [57]. Other examples of thresholding being instrumental in medical imaging include a local thresholding algorithm that determines

marrow intensity value in the neighborhood of each voxel based on nearest-neighbor statistics [58] and a multilevel thresholding technique that generates a contour map used for the identification of coherent regions [59].

Another popular technique for medical image segmentation is the active contour model which involves the use of an energy minimizing spline whose energy depends on its shape and location within the image. The traditional active contour model [60] has two primary drawbacks. Firstly, the initialization of the snake must be close enough to the desired contour in the image in order for the snake to evolve correctly towards the desired contour. A poor initialization will mean that the snake may be trapped in local minima. Secondly, the traditional snakes have difficulty evolving to concavities and sharp corners. The gradient vector flow (GVF) [26] was proposed as a new external force for snakes to solve the drawbacks of traditional snakes. As the GVF field is calculated as a diffusion of the gradient vectors of an edge map derived from the image, it greatly increases the capture range of the snake and the ability to move into boundary concavities. The GVF snake has been applied in numerous medical image analyses. It was used for surface extraction and thickness measurement of the articular cartilage from MR images. Gradient direction information was incorporated into the GVF model to make the snake more stable and converge to the correct surface, hence tracking the cartilage surfaces effectively [61]. In another application, the GVF snake was modified to contain both the local and global information of the contour, which made the snake more accurate and robust to blood vessel occlusions [62].

Another segmentation technique used in the work here is the watershed algorithm [21, 63] which is a technique that has been widely used in medical image segmentation [64

- 66] due to its inherent advantages. Besides being a simple and intuitive method, it is able to produce a complete division of the image into distinct regions even when the contrast is poor, thus obviating the need to carry out any post-processing work such as contour linking [23]. In the watershed algorithm, the image is treated as a topographical surface in which the height of each point on the surface is given by its corresponding gray level. The set of pixels with the lowest regional elevation corresponds to the regional minimum. The minima of an image are the groups of connected pixels whose grey levels are lower than those of their neighbors. Based on the rainfall simulation approach of the watershed algorithm, a drop of water that falls onto any point of the surface will flow downwards along the path of steepest slope, eventually ending in a minimum. This is the catchment basin. Watersheds are the boundaries of the different catchment basins. In image processing terms, the catchment basins are the image partitions that we seek to obtain, while the watersheds are the boundaries of the partitions. A graphical representation is in Figure 4.1.
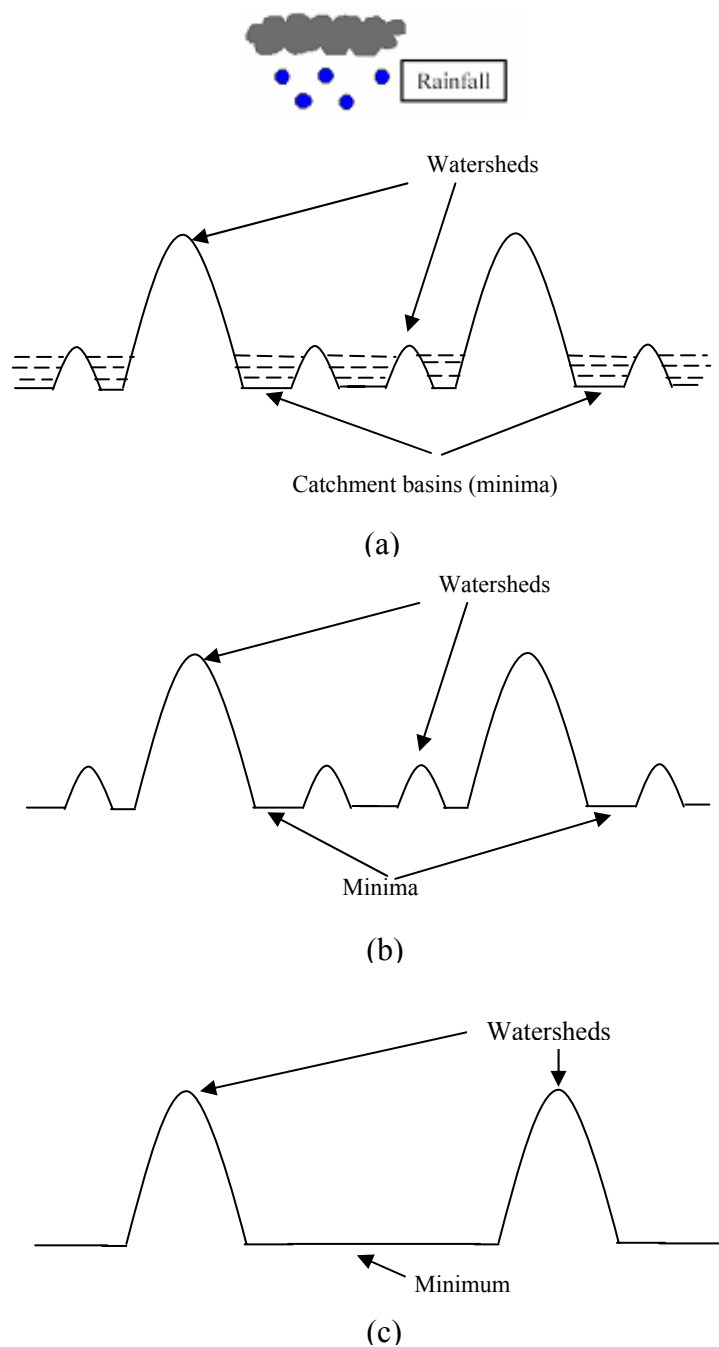
Figure 4.1: (a) Topographical analogy of rainfall simulation by watershed algorithm,

(b) Topographical representation of edge map when clustering is not carried out,

(c) Topographical representation of edge map when clustering is carried out.

Despite its many advantages, the watershed technique has some drawbacks, such as over-segmentation and sensitivity to noise [23]. The result of watershed segmentation is a large number of small regions, which reduces its usefulness due to the severe over-segmentation. In addition, the results obtained using the watershed transform are sensitive to local variations of the image, noise and false edges.

Though numerous techniques have been proposed for medical image segmentation, there is currently none for the segmentation of the human masticatory muscles. This is a challenging task due to the close proximity between the muscles and their surrounding soft tissue, as well as the complicated structure of the muscles. Hence 2D followed by 3D segmentation techniques for the human masticatory muscles were studied.

4.2   MR image segmentation using watershed algorithm

4.2.1 Overview of proposed method

The objective of our work here is to reduce the problem of over-segmentation posed by the watershed algorithm. In our improved watershed algorithm, we address the above drawbacks by (i) performing thresholding on the gradient magnitude image, and (ii) post-segmentation merging to merge the initial partitions formed by the watershed transform. When we applied our improved watershed algorithm to MR images, we observed that the problem of over-segmentation in MR images was due mainly to presence of fine textures irrelevant to the given segmentation task. We use clustering to address this problem.

One commonly used clustering algorithm is the fuzzy C-means (FCM) which is a soft-segmentation method [67 – 69] that has been used extensively [70]. Under soft segmentation method, voxels may be classified into multiple classes with a varying degree of membership. The FCM employs fuzzy partitioning such that a data point can belong to all clusters with different membership grades between 0 and 1. It is an iterative algorithm and its aim is to find cluster centers that minimize a dissimilarity function. Another commonly used clustering algorithm is the K-means clustering algorithm [71, 72]. The clusters produced by K-means clustering do not overlap, which is unlike those produced by FCM that employs soft partitioning. The K-means algorithm partitions data points into their respective clusters by minimizing a distance function. As compared to FCM, K-means clustering has a lower computational complexity. The performance of FCM also degrades significantly with increased noise.

In our proposed approach (Figure 4.2), we use K-means clustering (because of its lower computational complexity) to provide an initial coarse segmentation of the highly textured image before applying the improved watershed segmentation algorithm. Experiments are conducted using this proposed method.

```
                    ┌─────────────────┐
                    │   Input Image   │
                    └─────────────────┘
                             │  Gaussian Filtering
                             ▼
                    ┌─────────────────┐
                    │  Filtered Image │
                    └─────────────────┘
      ┌ ─ ─ ─ ─ ─ ─ ─ ─ │ ─ ─ ─ K-Means Clustering ─ ─ ─ ─ ┐
      ┆                  ▼                                   ┆
      ┆         ┌─────────────────┐                          ┆
      ┆         │ Clustered Image │                          ┆
      ┆         └─────────────────┘                          ┆
      └ ─ ─ ─ ─ ─ ─ ─ ─ │ ─ ─ ─ ─ ─ ─ ─ ─ ─ ─ ─ ─ ─ ─ ─ ─ ─┘
                             │  Sobel Filter
                             ▼
                    ┌─────────────────┐
                    │ Original Edge Map│
                    └─────────────────┘
                             │  Automated Thresholding
                             ▼
                    ┌─────────────────┐
                    │ Improved Edge Map│
                    └─────────────────┘
                             │  Watershed Segmentation
                             ▼
                    ┌─────────────────────┐
                    │Initial Segmentation Map│
                    └─────────────────────┘
                             │  Post-Segmentation Merging
                             ▼
                    ┌─────────────────────┐
                    │ Final Segmentation Map│
                    └─────────────────────┘
```
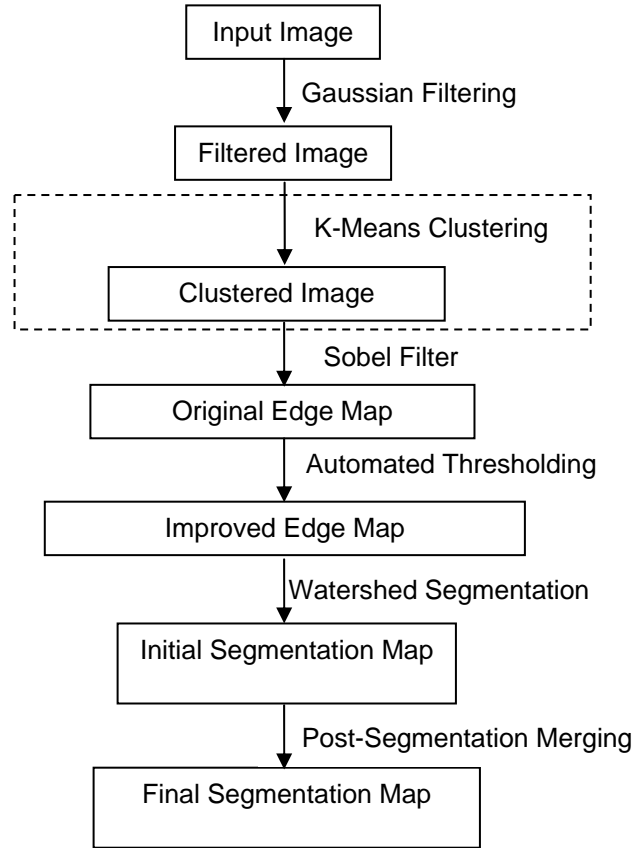
Figure 4.2: Flowchart of proposed improved watershed segmentation algorithm.

(The optional integration of K-Means clustering is in the dotted box.)

4.2.2 The proposed method

4.2.2.1 Obtaining the improved gradient magnitude image

In our improved watershed segmentation algorithm, Gaussian filtering is applied as a pre-processing step for image smoothing and to reduce presence of noise. The gradient magnitude image is obtained by applying the Sobel operator to the Gaussian-filtered image. We have also experimented with the Canny edge detector, and found that the results obtained by both methods are comparable.

The total number of partitions that result from segmentation is dependent on the number of edges. Unlike the conventional watershed algorithm, false edges are

discarded by thresholding the gradient magnitude image to reduce the number of false edges. The threshold is selected to be the mean magnitude of all the edge pixels. Pixels whose gradient magnitudes are greater than the threshold retain their original values, while those with values less than the threshold are set to zero.

4.2.2.2   Watershed segmentation: Initial partitioning

The rainfall analogy states that any drop of water that falls onto the topographical surface will flow along the path of steepest descent to a minimum. On the image, a $3{\times}3$ window is centered on each pixel and the steepest gradient direction computed. The center of the window is then shifted in the steepest gradient direction to the neighboring pixel. If there is more than one direction with the steepest gradient, the direction which was first computed is selected. This process is repeated until the path reaches a minimum. The pixels constituting the path adopt the label of that minimum. By scanning the image in a raster fashion, we repeat the rainfall simulation by tracing a path for all the pixels that are unlabelled. The paths reaching a common minimum adopt the same label as that minimum, and constitute the catchment basin, which is a partition in the image.

4.2.2.3   Post-segmentation merging

The initial segmentation map provides a complete division of the image with no under-segmentation but there is a problem of over-segmentation. A segmentation map with fewer partitions is generally preferred because it will provide a better representation of the original image. Hence, we implement a post-segmentation merging step, based on spatial criteria, to reduce the number of partitions significantly. When segmenting the masticatory muscles, which are relatively large compared to smaller objects of interest

such as blood vessels, the reduction of over-segmentation by merging produces segmentation maps that are more representative of the targeted anatomical objects.

Let the intensity value at point (x, y) in the original image be $I(x, y)$ and the initial partitions obtained from the watershed segmentation be $R = \{R_1, R_2, R_3, ..., R_N\}$, where R_i denotes the ith partition and N the total number of partitions. Let the number of pixels in each partition R_i be denoted by N_i. The mean intensity of each partition R_i is denoted by

$$M_i = \frac{1}{N_i} \sum_{(x,y) \in R_i} I(x, y) \tag{4.1}$$

Two measures are defined for neighbouring partitions R_i and R_j. The first measure is the difference in the mean intensities between partition R_i and partition R_j:

$$M_{ij} = |M_i - M_j| \tag{4.2}$$

The second measure is the difference in the intensity values between the 8-connected neighbours of the boundary pixels belonging to partition R_i and partition R_j. We first let m represent a pixel which lies on the boundary of a region R_i and the set neighs(m) represents its 8-connected neighbors. We further define a set of pixels of the neighbors of all boundary pixels of a partition R_i:

$$W_{im} = \{v | v \in \text{neighs}(m), m \in \text{boundary}(R_i)\} \tag{4.3}$$

The second measure is defined as:

$$B_{ij} = \left| \frac{1}{N_i^b} \sum_{m=1}^{N_i^b} \left[\frac{1}{k_i} \sum_{P \in W_{im}} I(P) \right] - \frac{1}{N_j^b} \sum_{m=1}^{N_j^b} \left[\frac{1}{k_j} \sum_{P \in W_{jm}} I(P) \right] \right| \tag{4.4}$$

where pixel $P \in W_{im}$, k is the number of pixels in W_{im} and N_i^b is the number of boundary pixels in partition R_i. The second measure differs from the first in that it takes into consideration only the boundary pixels of the partitions. This measure is introduced based on the assumption that two regions which have pixels with similar intensities surrounding the boundary pixels should be merged.

In addition, we introduce a criterion C_{ij}, which is a measure of similarity in intensity values between two partitions R_i and R_j, and define it as the sum of M_{ij} and B_{ij}:

$$C_{ij} = M_{ij} + B_{ij} \tag{4.5}$$

After determining C_{ij} for all partitions R_i and R_j, we calculate its mean and set it to be the threshold:

$$T_c = \frac{1}{\displaystyle\sum_{R_i \in R} \Theta\!\left(V_{R_i}\right)} \sum_{i=1}^{N} \sum_{j \in S_{R_i}} C_{ij} \tag{4.6}$$

where $\Theta\!\left(V_{R_i}\right)$ is the number of neighboring partitions surrounding partition R_i. The indices of the partitions surrounding partition R_i define the set S_{R_i}. If C_{ij} is less than T_c, partitions R_i and R_j are similar based on the spatial criterion and hence should be merged.

The size of a partition was also considered before deciding whether we should merge it with another partition. When segmenting relatively large objects such as masticatory muscles, it is reasonable to merge only small regions because larger regions are, in general, representative of individual objects and hence should not be merged. The size

threshold is set to be the average size (in terms of number of pixels) of all the partitions:

$$T_{size} = \frac{1}{N}\sum_{i=1}^{N} N_i \qquad (4.7)$$

If the partition size is less than T_{size}, the partition is small and not representative of an individual object, and should be considered for merging. Each partition whose size is smaller than T_{size} is compared with its neighboring partitions in terms of similarity in intensity.

The post-segmentation merging procedure is summarized as follows:

Step 1: Find the total number of partitions, N_i.

Step 2: Calculate C_{ij} for all partitions and determine T_c.

Step 3: Calculate size of each partition and determine T_{size}.

Step 4: Go to each partition in the image (left to right, top to bottom).

Step 5: If partition size $< T_{size}$ and if $C_{ij} < T_c$, mark the two partitions for merging.

Step 6: Merge all marked partitions and find the total number of partitions, N_{i+1}.

Step 7: Iterate the entire procedure till $N_{i+1} = N_i$.

4.2.2.4 K-means clustering with improved watershed algorithm

It can be observed that MR images of the head are highly textured especially in the muscles regions where there is presence of muscle fibres. We apply K-means clustering to the histogram to obtain a coarse segmentation of the highly textured MR image.

K-means clustering is suitable for biomedical image segmentation when the number of clusters (K) is known [73]. An MR image of the head typically consists of regions representing bone, soft tissue, fat and air. A suitable value of K would be 4 for such images. It should be stressed that the number of clusters may not be equal to the number of partitions obtained after clustering because in our work, the K-means clustering algorithm operates on the histogram of the image. It classifies the pixels in the image with the number of clusters fixed *a priori*. The centroids of the clusters are initially placed at equal intervals away from each other. Next, we take each data point and associate it with the nearest centroid according to its Euclidean distance from the cluster means. When all points have been assigned to their respective clusters, an initial clustering has been obtained. The new centroids are calculated, from which we determine the new distance measure, in the form of a squared error function, between the same data points and the nearest new centroid. This process is carried out iteratively and terminates when the cluster means do not shift by more than a given cut-off value or the iteration limit is reached.

In the resulting image after K-means clustering is applied, the highly textured areas are smoothened as neighbouring pixels with similar intensities are clustered. After clustering, all pixels within the same cluster are then assigned a common intensity value (the cluster centroid), and we have only K different intensity values compared to 256 different intensity values in the original image. A graphical representation of the proposed method is in Figure 4.1.

In image processing terms, the catchment basins are the image partitions that we seek to obtain, while the watersheds are the boundaries of the partitions (Figure 4.1(a)).

Without clustering, there is a total of 256 different intensity values (0-255) in the image. The presence of highly textured surfaces means that there are many local minima in the image, resulting in the formation of a larger number of watersheds when the rainfall simulation is applied (Figure 4.1(b)). After clustering, when the highly textured surfaces have been smoothened, there are fewer local minima on the edge map, and hence a smaller number of watersheds (Figure 4.1(c)).

4.2.3 Experiments

We compute the number of partitions in the segmentation maps obtained using (i) conventional watershed algorithm, (ii) improved watershed algorithm and (iii) K-means clustering with improved watershed algorithm. We use $\sigma = 1$ in the Gaussian filtering process. The Sobel edge filter used is a 3×3 mask. When comparing the Sobel filter against the Canny filter, the parameters for the latter are: $\sigma = 1$, 3×3 edge detector, upper threshold = 0.5, lower threshold = 0.05.

The above algorithms are applied to 60 MR images, with image size of 100×64 pixels, to segment the masseter. The number of partitions in the final segmentation maps produced by (i) conventional watershed algorithm, (ii) improved watershed algorithm and (iii) K-means clustering with improved watershed algorithm are compared to evaluate the effectiveness of our proposed method in reducing over-segmentation. Results obtained using our proposed method are also compared with those obtained using the gradient vector flow (GVF) snake and K-means clustering alone. The values of the parameters used in our GVF snake are: elasticity parameter = 0.5, rigidity parameter = 0.5, viscosity parameter = 0.1, external force weight = 1.

The manual segmentations (Figure 4.3), which serve as the ground truth in the evaluation of our proposed method, are provided by an expert radiologist who has more than 15 years of clinical experience.
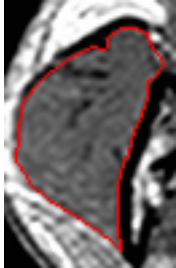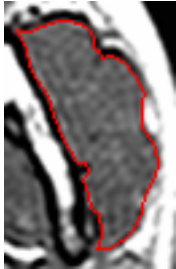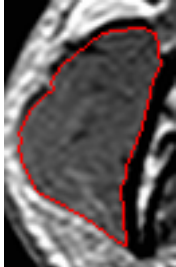

Figure 4.3: Original MR images and their corresponding ground truths.

To evaluate the consistency between our computerized segmentations and the manual segmentations, we use the κ index [74]:

$$\kappa = 2 \times \left(\frac{N(M \cap S)}{N(M) + N(S)} \right) \times 100\% \qquad (4.8)$$

where M and S denote the masseter regions obtained by manual segmentations and the proposed method, respectively, $M \cap S$ the intersection between M and S, and $N(\cdot)$ the number of pixels in a region. The masseter is located in the central portion of the 60 test images used in our study. Hence, the partition in the center of the segmentation map produced by the proposed method can easily be identified as the masseter region S. The smallest value of κ is 0% (no overlap) and the largest value is 100% (exact overlap).

In addition, experiments employing different parameter values are carried out. We vary the gradient threshold from 0.5 to 1.5 times the average edge magnitude. The effectiveness of merging criteria M_{ij} and C_{ij} are compared based on the number of final partitions formed. Instead of using $K = 4$ for clustering, we use $K = 6$ and $K = 8$ and compare the final segmentation results. It should be stressed that in our proposed method, we assume that small partitions are not representative of an individual object and should be considered for merging.

4.2.4 Results

Examples of segmentation maps obtained using the conventional and our improved watershed algorithms are shown in Figure 4.4. The mean number of partitions in the final segmentation maps and the extent of post-segmentation merging are listed in Table 4.1. On average, our improved watershed algorithm is able to produce

segmentation maps that have 95% fewer partitions than maps formed by the conventional algorithm.
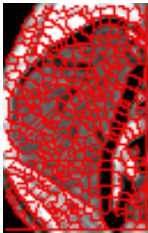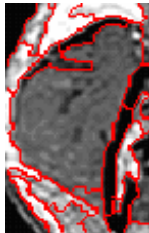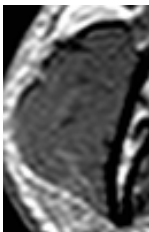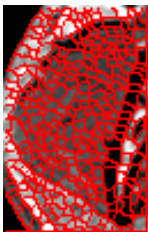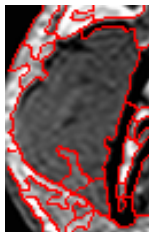
Original MR image	Segmentation map using conventional algorithm	Segmentation map using improved algorithm
(a)	342 partitions	5 partitions
(b)	342 partitions	8 partitions
(c)	328 partitions	7 partitions
(d)	343 partitions	14 partitions

Figure 4.4: Segmentation results using improved watershed algorithm.

Table 4.1: Summarized results obtained using improved watershed algorithm.

Number of MR images used = 60	Number of partitions in segmentation map using conventional algorithm	Number of partitions in segmentation map using improved algorithm	Percentage of partitions merged (%)
Mean	325	14.5	95.5
Standard Deviation	24.7	3.51	1.10

Table 4.2: Comparison of summarized results obtained using K-means clustering with improved watershed algorithm and GVF snake.

Number of MR images used = 60	Number of partitions in segmentation map using conventional algorithm	Number of partitions in segmentation map using improved algorithm with K-means clustering	Percentage of partitions merged (%)	κ index using proposed method (%)	κ index using GVF snake (%)
Mean	325	6.0	98.2	90.6	91.2
Standard Deviation	24.7	1.35	1.41	1.74	1.58

The summarized results obtained using K-means clustering with improved watershed segmentation algorithm are listed in Table 4.2 and examples of the segmentation maps are in Figure 4.5. The mean κ index obtained is 90.6%. On average, K-means clustering combined with the improved watershed is also able to produce segmentation maps that have 98% fewer partitions than those maps formed by the conventional algorithm.
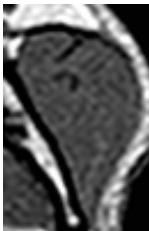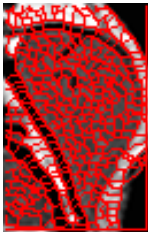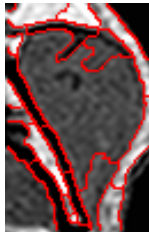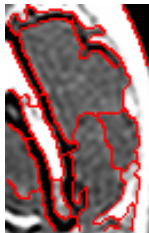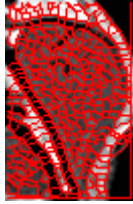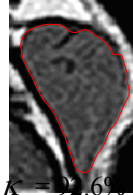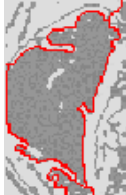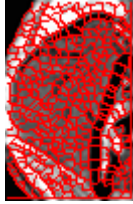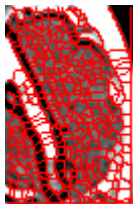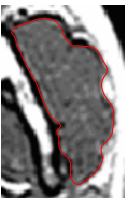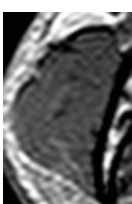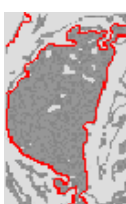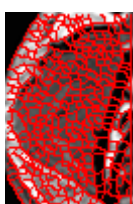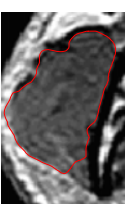
Original MR image	MR image after K-means clustering	Final segmentation map	Segmentation map using conventional algorithm	Final segmentation using GVF snake
(a)		4 partitions κ = 91.8%	342 partitions	κ = 92.6%
(b)		3 partitions κ = 93.0%	342 partitions	κ = 93.2%
(c)		4 partitions κ = 92.1%	328 partitions	κ = 91.8%
(d)		4 partitions κ = 91.2%	343 partitions	κ = 90.7%

Figure 4.5: Results from K-means clustering with improved watershed algorithm.

Using the GVF snake, the mean κ index obtained is 91.2% (Table 4.2). Besides the GVF snake, we made use of K-means clustering alone to delineate the masseter. The mean κ obtained is approximately 83%, which is much lower than the 90.6% obtained using the proposed method. K-means clustering alone is unable to fully delineate the

masseter. It is seen in the top right-hand portion of Figure 4.5(b) that small unwanted regions remain attached to the masseter after K-means clustering.

4.2.5 Discussion

4.2.5.1 Comparisons between conventional and proposed improved watershed algorithms

We apply the improved watershed algorithm to segment the masseter from MR images. The results in Figure 4.4 show that there is a serious problem of over-segmentation with the conventional watershed segmentation algorithm. Referring to Figure 4.4(b), the segmentation map produced by the conventional algorithm has 342 partitions, in contrast to the 8 partitions resulting from the improved algorithm. Thus, 98% of the initial partitions have been merged and the improvement factor is 342/8 = 43. A better representation of the masseter has been obtained.

Visual inspection of the segmentation results reveals that there is no visible under-segmentation. However, the improved algorithm has not completely solved the problem of over-segmentation (Figure 4.4). This may be explained by the fact that regions with relatively similar intensities give rise to many local minima when the improved watershed algorithm is applied. We address this problem by making use of K-means clustering to smooth the inhomogeneous regions before applying the improved watershed segmentation algorithm.

4.2.5.2 Improved watershed algorithm with and without clustering

The segmentation maps obtained using the improved watershed segmentation algorithm with and without K-means clustering are compared. In Figure 4.4(c), there are 7 partitions in the segmentation map produced by the improved watershed segmentation algorithm. When we apply K-means clustering combined with the improved watershed segmentation algorithm to the same image, we obtain a much improved segmentation map with only 4 partitions (Figure 4.5(c)). Compared with the segmentation map obtained using the conventional algorithm, which has 328 partitions, the proposed method produces a segmentation map with 98% fewer partitions and a κ value of 91.8%.

4.2.5.3 Comparison between proposed method and GVF snake

The segmentation results obtained using the proposed method are comparable to those obtained using the GVF snake (Figure 4.6). The mean κ values are 90.6% and 91.2%, for the proposed method and the GVF snake, respectively. It should be noted, however, that the proposed method has the advantage of lower computational complexity. With the GVF snake, correct initialization is critical; improper initialization will lead to longer computational time and inaccurate segmentation (Figure 4.6). Furthermore, good results with the GVF snake are highly dependent on correct tuning of the parameter values.

4.2.5.4 Selection of threshold for magnitude of edge pixels

In our work, thresholding of the gradient magnitude image was performed with the threshold set to the average magnitude of all the edge pixels. When the threshold is set to 1.5 times the average magnitude, there is under-segmentation and missing edges,

resulting in the targeted object not being fully delineated. In contrast, when the threshold is set to be 0.5 times the average magnitude, over-segmentation is present and we do not obtain a good representation of the targeted object. By selecting the average magnitude to be the threshold, we avoid under-segmentation and reduce over-segmentation.
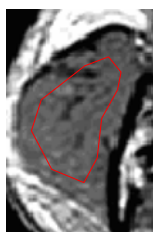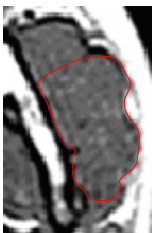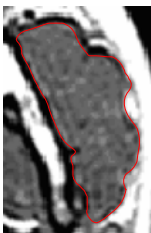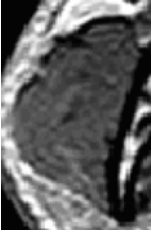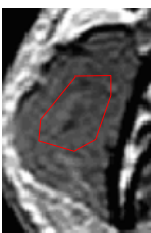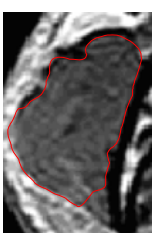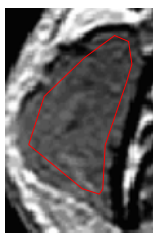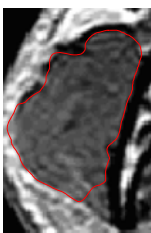
Original MR image	Poor initialization	Final segmentation	Good initialization	Final segmentation
				$\kappa = 92.6\%$
				$\kappa = 93.2\%$
				$\kappa = 91.8\%$
				$\kappa = 90.7\%$

Figure 4.6: Segmentation results obtained using GVF snake.

4.2.5.5 Sensitivity to merging criteria, M_{ij} and C_{ij}

If M_{ij}, instead of C_{ij}, is used as the similarity criterion, the results (Figure 4.7) are not as good. As observed in Figure 4.7(d), using M_{ij} produces a final segmentation map with 20 partitions; with C_{ij}, the final segmentation map has 15 partitions.
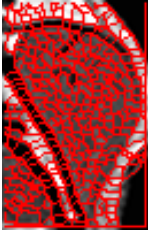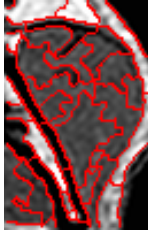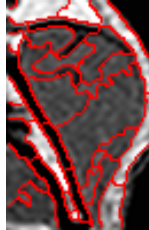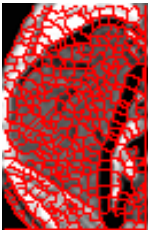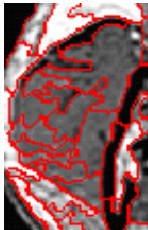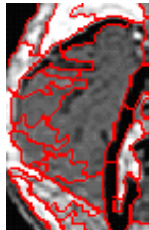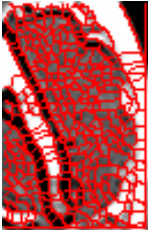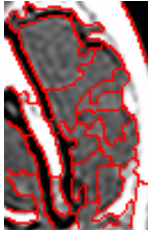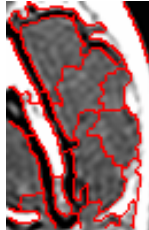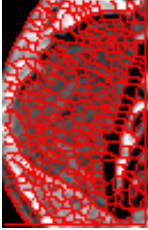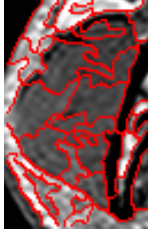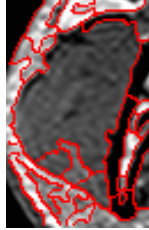
Original MR image	Segmentation map using conventional algorithm	Segmentation map using improved algorithm (M_{ij} as merging criterion)	Segmentation map using improved algorithm (C_{ij} as merging criterion)
(a)	342 partitions	22 partitions	19 partitions
(b)	342 partitions	17 partitions	15 partitions
(c)	328 partitions	13 partitions	10 partitions
(d)	343 partitions	20 partitions	15 partitions

Figure 4.7: Comparison between results obtained using different merging criteria.

4.2.5.6   Sensitivity to number of clusters (K)

We have been using $K = 4$ for K-means clustering since we have prior knowledge that the regions in the MR images represent bone, soft tissue, fat and air. The results obtained with K equal to 4, 6 and 8 are shown in Figure 4.8. It is clear that the segmentation results are very similar. Hence, even though the actual number of regions is not known *a priori*, an estimate of K obtained by visual inspection may be used with satisfactory outcomes.
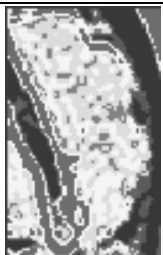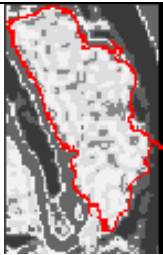
Original MR image	MR image after K-means clustering	Final segmentation map
	$K = 4$	
	$K = 6$	
	$K = 8$	

Figure 4.8: Segmentation results using different values of K during clustering.

4.2.5.7   Limitations of proposed method

It should be stressed that the proposed method has been designed for the segmentation of relatively large objects such as the masseter that we have used for illustration in this paper, and may not be generalized to segmentation of small objects such as blood vessels. This is because during post-segmentation merging, we have assumed that larger regions are representative of individual objects and hence should not be merged. For segmentation of smaller objects, other algorithms [75 - 77] may be more appropriate.

4.3   MR image segmentation using model-based approach

4.3.1 Overview of proposed method

It has been mentioned earlier in Section 4.2.5.3 that in order for the GVF snake to produce a good segmentation in our application here, we will need to have a good initialization. In this section, a model-based method for automatically initializing the GVF snake and obtaining good segmentations is presented.

The proposed method is a two-stage process (Figure 4.9). In the training stage, we use reference MR images in which the targeted muscles have been manually segmented to determine the spatial relationships between the head region of interest (ROI) and targeted muscle ROI. The targeted muscle and head ROIs are the bounding boxes of the muscle and head regions, respectively, in a 2D image (Figure 4.10(a)). The manual segmentations of the muscles are also used to construct muscle templates which are employed in the segmentation stage to discard unwanted background pixels in the study image. An initial segmentation is obtained by using morphological operators and

this serves as the input contour to the GVF snake which iterates to obtain the final segmentation result. The proposed method is used to segment the masseter, lateral pterygoid and medial pterygoid, shown in Figure 4.11, from 2D MR images.

Acquisition of prior knowledge from reference data sets

Segmentation process on test data sets

Input I_i and I_f for muscle in each training data set

↓

Locate reference image

↓

Manual contour tracing of the muscle for each 2D reference image

↓

Automatic detection of head ROI and muscle ROI for each image

↓

Derive a relative relationship between head ROI and muscle ROI for each image

↓

Obtain an average of this relationship for all these reference images

Input I_i and I_f for muscle in each training data set

↓

Locate reference image

↓

Automatic detection of head ROI

↓

Automatic detection of muscle ROI by the system using prior knowledge

↓

Apply anisotropic diffusion to muscle ROI

↓

Thresholding to remove fat and bone after FCM clustering

↓

Check for overlap with template of targeted muscle for initial segmentation

↓

Perform GVF snake to refine initial segmentation

Figure 4.9: Overview of methodology.
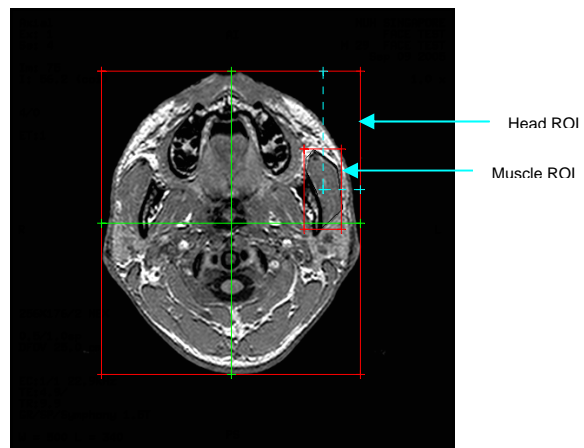
(a)
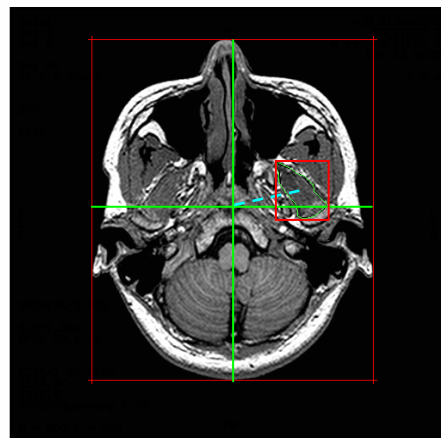
(b)
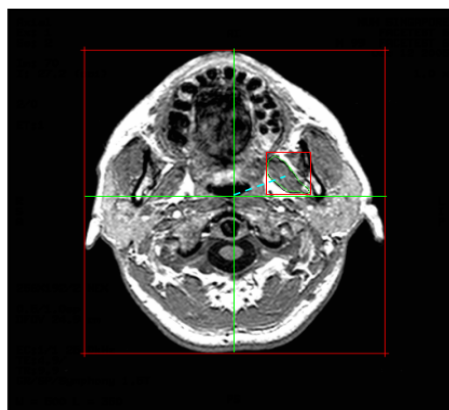
(c)

Figure 4.10: Spatial relationship between

(a) boundary of head ROI and origin of masseter ROI,

(b) origin of head ROI and origin of lateral pterygoid ROI,

(c) origin of head ROI and origin of medial pterygoid ROI.
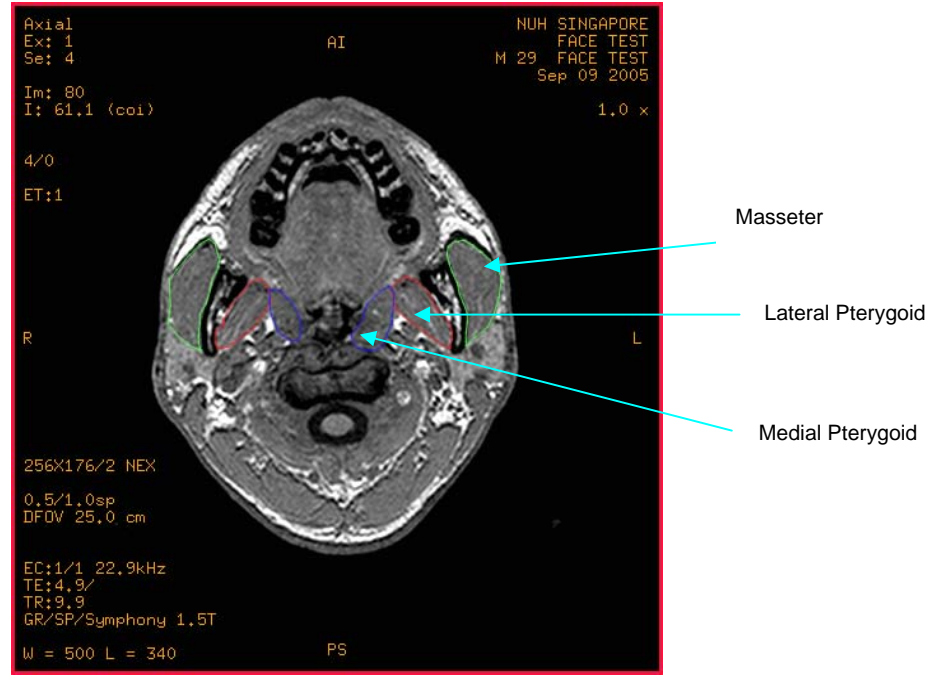
Figure 4.11: Masticatory muscles in MR T1 FLASH image.

4.3.2 The proposed method

4.3.2.1 Acquisition of prior knowledge

The masticatory muscles in the training data sets are first manually segmented by a medical expert. The first 2D axial slice in each data set is in the region of the orbit while the last slice is in the neck region. We assign a start index I_i to the axial slice in which the targeted muscle first appears and an end index I_f to the axial slice in which the targeted muscle last appears in the data set. In addition, we introduce the normalized slice index I_n for a MR slice I_r which lies between I_i and I_f:

$$I_n = \frac{I_r - I_i}{I_f - I_i} \qquad (4.9)$$

For each of the five training data sets, we compute the relative location of the MR slice I_l which has the largest surface area of the targeted muscle. This serves as the reference slice. The average values of I_l for the masseter, lateral pterygoid and medial pterygoid are 0.487, 0.383 and 0.423, respectively. The actual I_l in the training data sets ranges from 0.477 to 0.494, 0.368 to 0.395 and 0.405 to 0.440 for the masseter, lateral pterygoid and medial pterygoid, respectively.

Having selected the reference slice from each data set for each of the muscles, we now automatically detect the head ROI (Figure 4.12(a)) from the projections of the image in the horizontal and vertical directions (Figure 4.12(b)).

(a)

vertical   horizontal
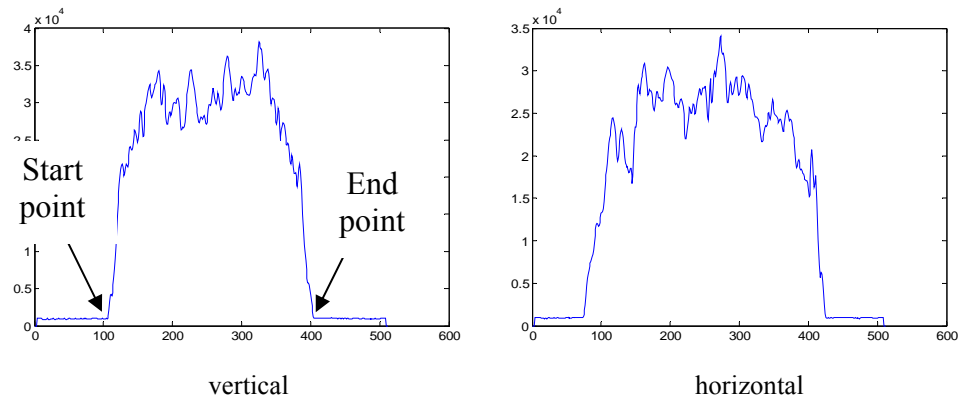
(b)

Figure 4.12: (a) Head ROI, (b) Projections in vertical and horizontal directions.

The masticatory muscles are paired muscles with symmetrical origins and attachments on each side of the midline. The masseter has a lateral origin and attachment, and is centered laterally to the ramus of the mandible. The medial and lateral pterygoid muscles have medial origins on the pterygoid processes and lateral attachments to the ramus and neck of the mandible, respectively. We make use of this anatomical information, together with our observations from the five training data sets to specify a spatial relationship between the ROI of each masticatory muscle and the head ROI in the reference slice.

The spatial relationship between the head and masseter ROIs (Fig. 4.10(a)) is specified in terms of the distance between the boundaries of the head ROI and the origin of the masseter ROI. For a reference slice of the masseter, the distances $l_1, w_1, j_1, k_1, m_1, n_1$ (Fig. 4.13(a)) are measured and the relative distances calculated as follows:

$$m_{1,r} = \frac{m_1}{l_1} \ , \ n_{1,r} = \frac{n_1}{w_1} \ , \ k_{1,r} = \frac{k_1}{l_1} \ , \ j_{1,r} = \frac{j_1}{w_1} \tag{4.10}$$

To obtain a good estimate of the spatial relationship, we use the mean values of $m_{1,r}, n_{1,r}, k_{1,r}, j_{1,r}$ obtained from the five reference slices.

The model of the muscle requires a template of the muscle region in addition to the spatial relationship. This is obtained by first manually tracing the masseter boundary on each of the five reference slices. The boundary (or contour) is represented as a linked list of points whose coordinates are normalized to the length and breadth of the head ROI to allow for different head sizes. The five masseter contours are aligned using their centroids, and the mean contour obtained by averaging the radial distances

for each unit polar angle from 0 to 360 degrees. The mean contour is the template of the masseter.

(a)

$i = 2$ for lateral pterygoid

$i = 3$ for medial pterygoid

(b)
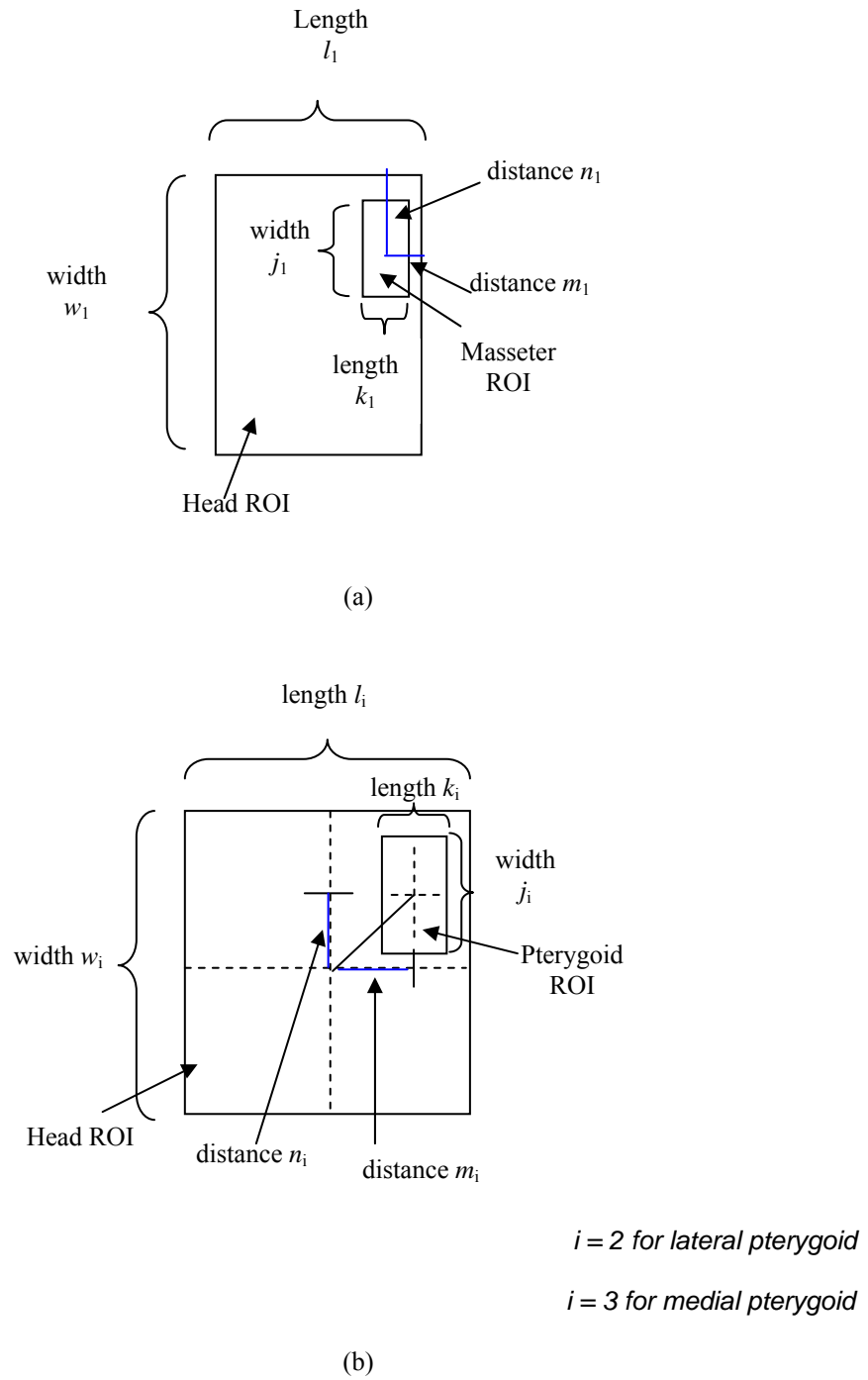
Figure 4.13: (a) Spatial relationship between head and masseter ROIs,

(b) Spatial relationship between head and lateral pterygoid ROIs in reference images.

The spatial relationships between the head and the lateral and medial pterygoid ROIs (Figure 4.10(b) and Figure 4.10(c)) are specified in terms of the distance from the origin of the head ROI to the origin of the muscle ROIs. Following the procedure used for the masseter, we measure the various spatial distances $l_2, w_2, j_2, k_2, m_2, n_2$ for the lateral pterygoid (Figure 4.13(b)) and calculate the relative distances $m_{2,r}, n_{2,r}, k_{2,r}, j_{2,r}$ of each of the five reference slices from the five training data sets. This procedure is also used for the medial pterygoid where we first measure $l_3, w_3, j_3, k_3, m_3, n_3$ followed by calculation of $m_{3,r}, n_{3,r}, k_{3,r}, j_{3,r}$. The process of constructing the templates of the lateral and medial pterygoids follows that for the masseter.

4.3.2.2 Segmentation of muscles from MR slices in study datasets

Given an image from the study data set, the system first automatically determines the head ROI based on the vertical and horizontal projections (as described in the previous section). The system then makes use of the spatial relationship between the targeted muscle ROI and the head ROI to identify the targeted muscle ROI in the study image. A combination of image processing techniques, which includes anisotropic diffusion, template correlation and GVF snake, is used to arrive at the final segmentation.

Given that the width and length of the head ROI in the study image are a_i and b_i, respectively, where $i = 1,2,3$ denotes the masseter, lateral pterygoid and medial pterygoid, respectively, we derive equations for the spatial parameters c_i, d_i, e_i, f_i (Figure 4.14):

$$c_i = a_i j_{i,r} s \quad , \quad d_i = b_i k_{i,r} s \quad , \quad e_i = a_i n_{i,r} s \quad , \quad f_i = b_i m_{i,r} s \qquad (4.11)$$
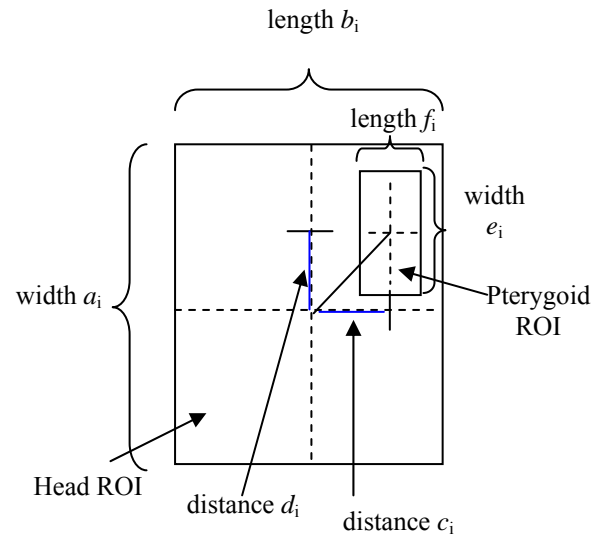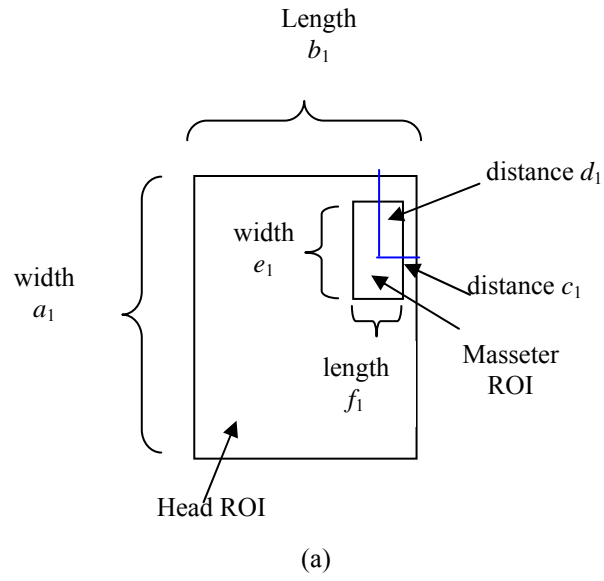
Figure 4.14: (a) Spatial relationship between head and masseter ROIs,

(b) Spatial relationship between head and lateral pterygoid ROIs in study images.

Parameter s is a scaling factor introduced to allow for the slight variations in location, shape and size of the muscles between different subjects. In our work, the minimum

and maximum values of s are found to be 1.3 and 2.5, respectively. The selection of an appropriate value of s is further discussed in Section 4.3.5. When s is 2.5, our method is applicable to images that have been rotated 15° clockwise or anti-clockwise from the upright position. The selection of an appropriate value of s is further discussed in Section 4.3.5.

The muscles consist of bundles of multinucleated cells known as muscle fibers, which give rise to a highly textured appearance in the MR image. An image of the masseter with its muscle fibers is shown in Figure 4.15. Inaccurate results will be produced when we apply active contour and GVF techniques to such textured regions, thus necessitating prior image smoothing with anisotropic diffusion [32] (number of iterations = 20, time-step = 0.2, one smoothing per iteration) which encourages intra-region smoothing while inhibiting inter-region smoothing.
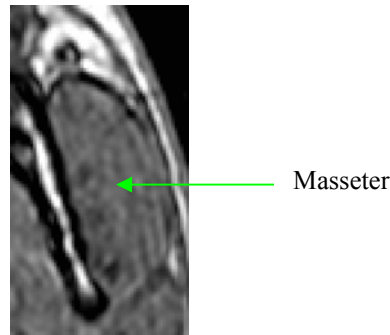
Figure 4.15: Masseter with its muscle fibers.

The muscle ROI comprises soft tissue, fat and bone. Compared to soft tissue, bone has relatively low and fat relatively high intensity values. Using this knowledge, we are able to approximately separate the soft tissue from the bone and the fat. We make use of the fuzzy c-means (FCM) algorithm [78] with three clusters to divide the muscle ROI into three different clusters. As the defined ROI is small, the difference in

computation times taken by FCM and K-means clustering is insignificant. After the ROI has been clustered, thresholding is then carried out, with the lower and upper thresholds being the minimum and maximum intensity values of the second cluster, to form the binary image of the ROI. We discuss the effect of using four clusters in Section 4.3.5.

The templates of the masseter, lateral and medial pterygoids are shown in Figure 4.16. The targeted muscle template ($T_1 \times T_2$ pixels) is moved from left to right, top to bottom across the targeted muscle ROI ($R_1 \times R_2$ pixels). We measure the amount of overlap between the ROI and the template at each position and this is done $(T_1 - R_1)(T_2 - R_2)$ times. If the regions in the targeted muscle ROI and the template overlap by 75% or more, we note the positions of the overlapping pixels. We discuss the effect of changing the threshold value to 65% and 85% in Section 4.3.5.

(a) (b) (c)
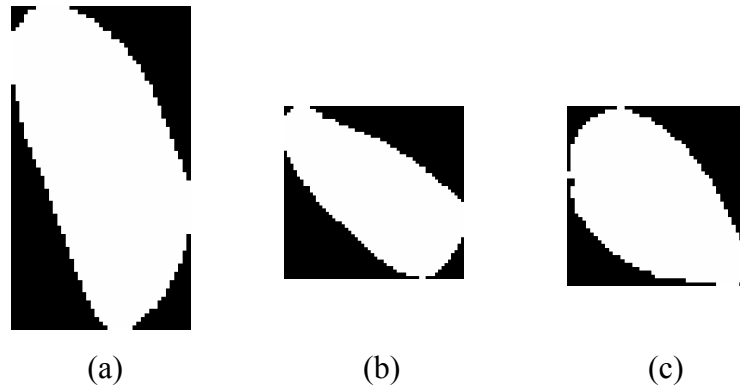
Figure 4.16: Templates of (a) masseter, (b) lateral pterygoid, (c) medial pterygoid.

After all the checking has been done, a binary image is formed with the pixels noted earlier taking a value of '1'. Morphological opening is then applied to the binary image to open the connections between the muscle region and its surrounding soft tissue.

Connected component labelling [79] is employed to find the largest connected component. Morphological closing is used to fill up the holes in the resulting image. The initial segmentation of the muscle is thus obtained. The edge map of the initial segmentation is derived using Canny filter [80] and used to initialize the GVF [26] snake for refining the initial segmentation of the muscle.

The use of GVF snake is preferred over the conventional active contours or snakes which are curves that move within images to find object boundaries. The curve is represented by:

$$\mathrm{X}(s) = [x(s), y(s)], \ s \in [0,1] \tag{4.12}$$

and it deforms through the image to minimize the energy function:

$$E = \int_0^1 \left[\frac{1}{2} \left(\alpha |\mathrm{X}'(s)|^2 + \beta |\mathrm{X}''(s)|^2 \right) + E_{ext}(\mathrm{X}(s)) \right] ds \tag{4.13}$$

where α and β are parameters representing the degree of the smoothness and tautness of the contour respectively. $\mathrm{X}'(s)$ and $\mathrm{X}''(s)$ are the first and second derivatives of $\mathrm{X}(s)$ with respect to s. The external energy E_{ext} is derived from the image and set to small values at features of interest. As object boundaries are usually of high gradient in the image $I(x, y)$, a typical example of external energy for seeking the edges is given as:

$$E_{ext}(x, y) = -|\nabla[G_\sigma(x, y) * I(x, y)]|^2 \tag{4.14}$$

where $G_\sigma(x, y)$ is a 2D Gaussian function with standard deviation σ. $*$ denotes linear convolution and ∇ denotes the gradient operator. The external force F_{ext} is derived from external energy and defined so as to attract the snake to strong edges:

$$F_{ext}(\mathrm{X}) = -\nabla E_{ext}(\mathrm{X}) \qquad (4.15)$$

GVF was proposed as a new external force for snakes to solve the drawbacks of traditional snakes. The GVF field is the vector field:

$$\mathbf{v}(x, y) = [u(x, y), v(x, y)] \qquad (4.16)$$

that minimizes the energy function:

$$\varepsilon = \iint \mu\left(u_x^2 + u_y^2 + v_x^2 + v_y^2\right) + \left|\nabla f\right|^2 \left|\mathbf{v} - \nabla f\right|^2 \partial x \partial y \qquad (4.17)$$

where $f = -E_{ext}$ is an edge map derived from the image, and μ is a parameter controlling the degree of smoothness of the vector field. By replacing the external force F_{ext} by the GVF field $\mathbf{v}$, a solution for GVF snake can be obtained.

4.3.3 Experiments

Our proposed method was applied to five MR study data sets. The user is required to input I_i and I_f for each of the targeted muscles in each data set. The reference slice will then be automatically derived. For each muscle, we performed 2D segmentation on the reference slice of the muscle, as well as on the two slices superior and two slices inferior to the reference slice. Hence, a total of 75 segmentation results (25 for each muscle) were obtained. The values of the parameters used in our GVF snake are: elasticity parameter = 0.5, rigidity parameter = 0.5, viscosity parameter = 0.1, external force weight = 1. The consistency between our computerized segmentations and the manual segmentations was evaluated using the κ index which was introduced earlier in equation 4.8.

In addition, we make use of false positive rate (FPR) to measure the probability of the method incorrectly giving a positive result:

$$FPR = \left(\frac{N(F_p)}{N(M)} \right) \times 100\% \qquad (4.18)$$

where $N(F_p)$ denotes the number of pixels which the method incorrectly determines as positive. The false negative rate (FNR) gives the probability of a negative result:

$$FNR = \left(\frac{N(F_n)}{N(M)} \right) \times 100\% \qquad (4.19)$$

where $N(F_n)$ denotes the number of pixels which the method incorrectly determines as negative.

In addition to experiments carried out to check for the accuracies of the segmentations obtained using our proposed method, other experiments were carried out to analyze the sensitivity to scaling factor s and image rotation of our proposed method. Parameters such as the number of clusters used in FCM clustering and overlap threshold were also justified empirically.

4.3.4 Results

We perform 2D segmentation of the masseter on a total of 25 MR images from the five study data sets. In Figure 4.17, we show a set of masseter results obtained after each stage. In Figure 4.18, we display another 10 segmentation results of the masseter from different MR images. The above results are obtained using s = 1.3. Numerical validations are performed on the 25 segmentation results by comparison with the ground truths, with the results tabulated in Table 4.3. The mean κ, FPR and FNR are 91.4%, 7.8% and 9.4%, respectively.
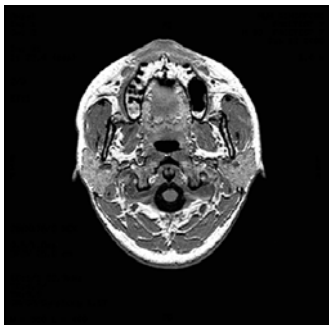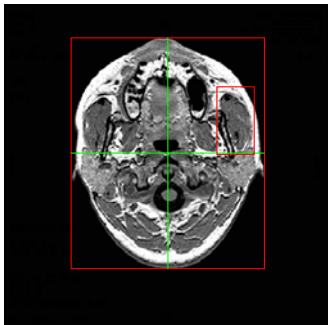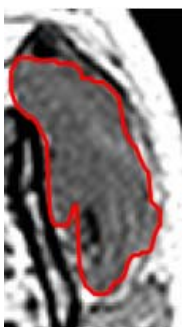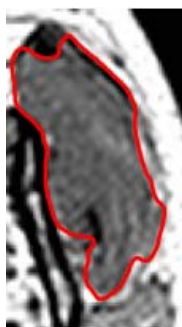
Figure 4.17: Results at each stage for segmentation of masseter.
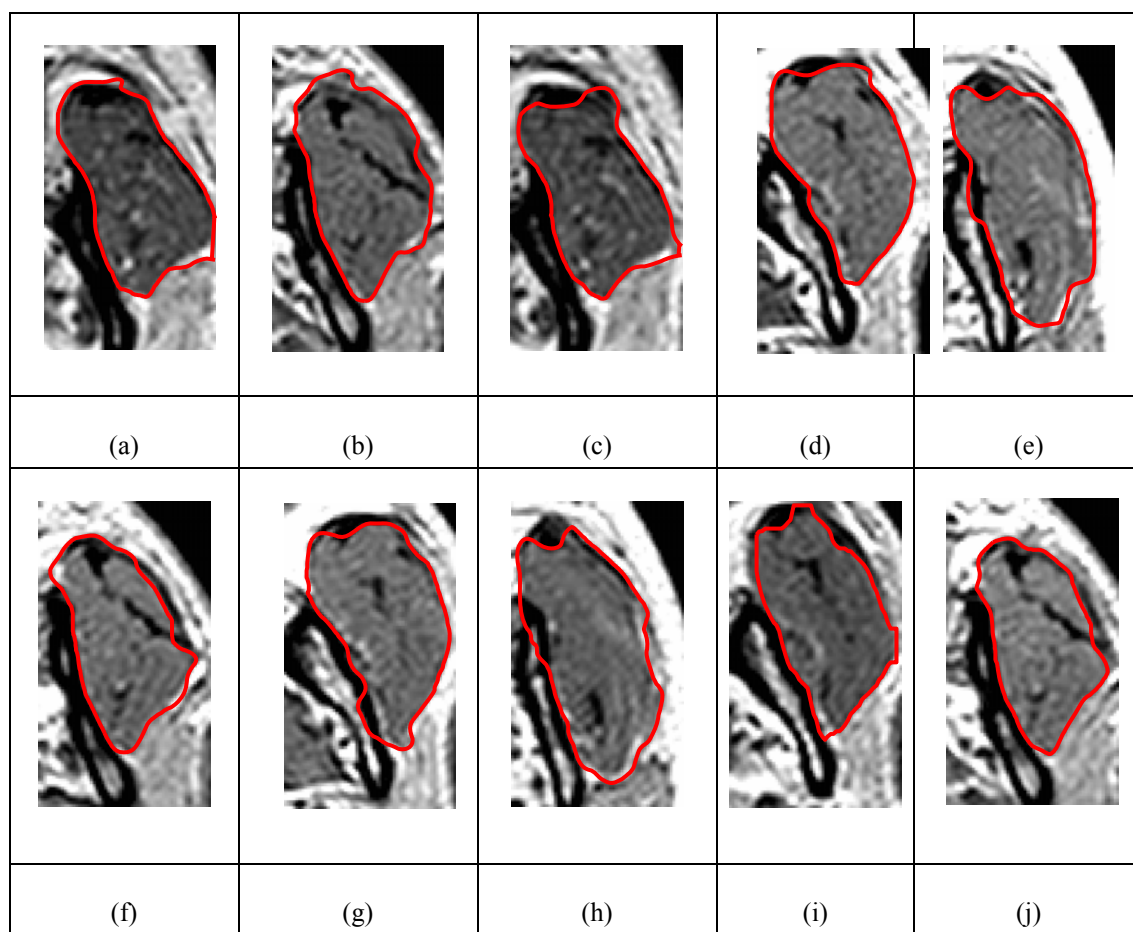
Figure 4.18: Segmentations of masseter from 10 different MR images.

Table 4.3: Validation results on segmentation of masseter.

Image Index	κ (%)	FPR (%)	FNR (%)	Image Index	κ (%)	FPR (%)	FNR (%)
1	93.0	2.6	11.4	14	91.8	10.3	6.1
2	93.5	3.8	9.2	15	90.2	9.5	10.1
3	92.8	4.5	9.9	16	87.8	9.7	14.7
4	91.3	6.3	11.1	17	90.8	7.3	11.1
5	92.8	7.7	6.7	18	92.0	9.2	6.8
6	90.6	11.6	7.2	19	91.5	7.4	9.6
7	89.5	10.4	10.6	20	90.3	8.2	11.2
8	91.5	5.8	11.2	21	91.4	6.3	10.9
9	90.2	9.8	9.8	22	91.8	7.1	9.3
10	88.6	9.2	13.6	23	93.3	5.2	8.2
11	91.2	10.6	7	24	92.1	5.8	10
12	92.4	10.9	4.3	25	91.6	7.9	8.9
13	93.0	7.5	6.5	**Mean**	**91.4**	**7.8**	**9.4**

The ROIs of the lateral pterygoid and medial pterygoid identified by our proposed method are shown in Figures 4.19(a) and 4.19(b), respectively. They are obtained using $s = 1.3$. Five sets of segmentation results for the lateral pterygoid are displayed in Figure 4.20 and five sets of segmentation results for the medial pterygoid in Figure 4.21. The average κ, FPR and FNR are 92.1%, 5.9%, 9.9%, respectively, for the lateral pterygoid (Table 4.4), and 91.2%, 8.6%, 9.1%, respectively, for the medial pterygoid (Table 4.5).

(a)   (b)
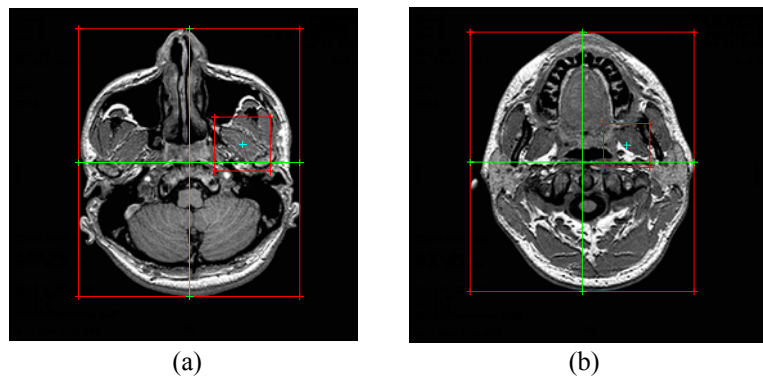
Figure 4.19: Identified ROI of (a) lateral pterygoid, (b) medial pterygoid.
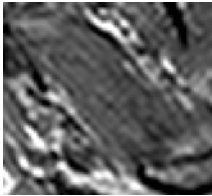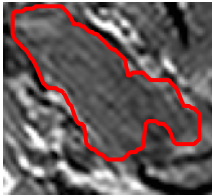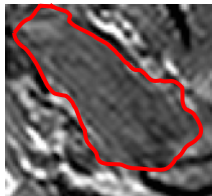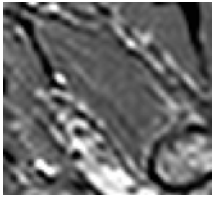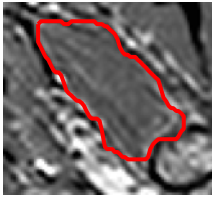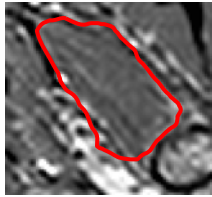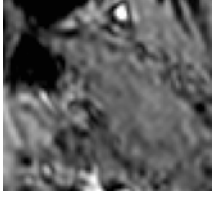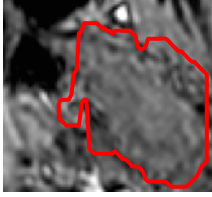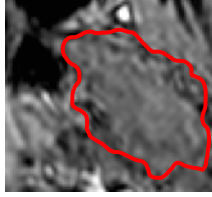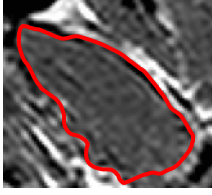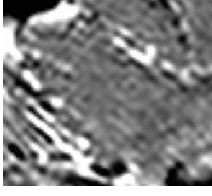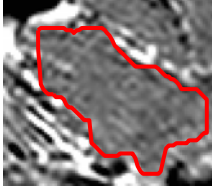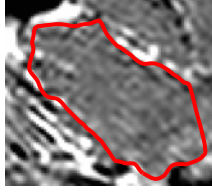
Result	Original ROI of lateral pterygoid	Initialization of GVF snake	Final segmentation of lateral pterygoid
1			
2			
3			
4			
5			

Figure 4.20: Segmentation results of lateral pterygoid.
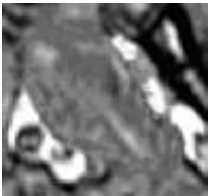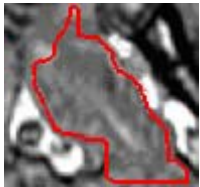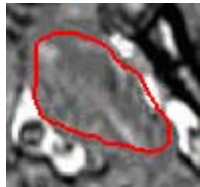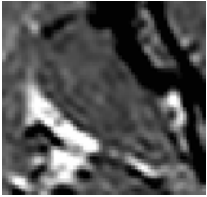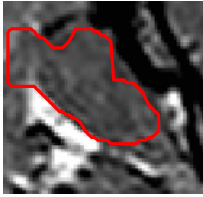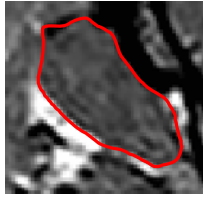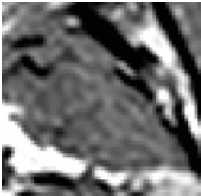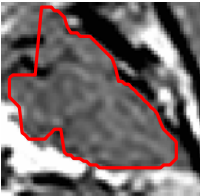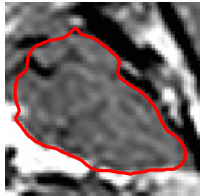
Result	Original ROI of medial pterygoid	Initialization of GVF snake	Final segmentation of medial pterygoid
1			
2			
3			
4			
5			

Figure 4.21: Segmentation results of medial pterygoid.

Table 4.4: Validation results on segmentation of lateral pterygoid.

Image Index	κ (%)	FPR (%)	FNR (%)	Image Index	κ (%)	FPR (%)	FNR (%)
1	93.6	5.7	7.1	14	91.3	6.1	11.3
2	93.8	4.3	8.1	15	91.0	5.5	12.5
3	95.2	3.2	6.4	16	88.9	7.7	14.5
4	92.4	5.8	9.4	17	91.7	7.2	9.4
5	91.8	6.0	10.4	18	93.0	4.5	9.5
6	90.8	5.5	12.9	19	92.4	7.5	7.7
7	91.2	7.8	9.8	20	90.5	9	10
8	92.0	5.7	10.3	21	91.9	6.3	9.9
9	92.2	6.2	9.4	22	92.8	5.9	8.5
10	91.5	9.4	7.6	23	95.3	3.2	6.2
11	89.8	5.6	14.8	24	93.1	5.1	8.7
12	91.0	4.3	13.7	25	92.6	6.5	8.3
13	92.8	3.8	10.6	**Mean**	**92.1**	**5.9**	**9.9**

Table 4.5: Validation results on segmentation of medial pterygoid.

Image Index	κ (%)	FPR (%)	FNR (%)	Image Index	κ (%)	FPR (%)	FNR (%)
1	91.2	8.7	8.9	14	90.5	9.7	9.3
2	92.5	7.1	7.9	15	88.5	8.5	14.5
3	92.8	5.5	8.9	16	90.8	7.2	11.2
4	92.1	7.3	8.5	17	91.5	8.1	8.9
5	91.8	9.2	7.2	18	92.1	9.2	6.6
6	89.6	10.6	10.2	19	90.9	10.1	8.1
7	92.0	9.2	6.8	20	89.5	9.3	11.7
8	93.3	8.5	4.9	21	90.4	7.3	11.9
9	91.1	9.2	8.6	22	90.8	8.1	10.3
10	89.6	9.6	11.2	23	92.3	9.2	6.2
11	91.9	8.8	7.4	24	91.8	9.7	6.7
12	91.5	7.5	9.5	25	87.1	8.8	17
13	93.7	7.8	4.8	**Mean**	**91.2**	**8.6**	**9.1**

4.3.5 Discussion

4.3.5.1   Accuracy of segmentation results

Segmenting the masticatory muscles from MR images is difficult because a muscle and its surrounding tissue have similar gray levels, often with no distinct boundaries between them. Despite this, our proposed method, which involves prior knowledge of the location and a template of the muscle, is able to segment with average κ greater than 90%. In the process, the problem of providing good initializations to the GVF snake was solved. The proposed method was also applied to the segmentation of the masseter, lateral and medial pterygoids.

By training the system using the spatial relationship between the head ROI and muscle ROI, the system is able to automatically determine the muscle ROI in a study image. In Figure 4.17, the output at each stage of the method for segmenting the masseter is displayed. The soft tissue is approximately separated from the fat and bone through FCM with three clusters. In the ROI after thresholding, soft tissue is present together with muscles. By checking for the overlap between the template and the regions in the ROI, we are able to remove the majority of the unwanted soft tissue. After checking for overlap with the template, small unwanted regions remaining in the muscle ROI are then removed through the use of connected components labelling. This gives us an initial segmentation of the muscle.

The initialization process for the GVF snake is automatic. The initial segmentations serve as good initializations for the GVF snake; since they are close to the actual boundaries of the muscles, relatively little iterations are required before the GVF snake converges. Furthermore, accurate segmentations are, to a certain extent, dependent on

the initial state. Our method to initialize the GVF snake proves to be good as we are able to obtain κ better than 90%.

The presence of clear, distinct boundaries and the proximity of the initialization to the GVF snake affect the accuracy of our segmentation results. A better accuracy will be achieved when there are clear boundaries between the masseter and its surrounding soft tissue ($\kappa = 93.5\%$, Figure 4.18(d)). On the contrary, the lack of a distinctive boundary may result in a less accurate segmentation ($\kappa = 89.5\%$, Figure 4.18(a)). Referring to Figures 4.18(g) and (h), leakages can be observed in the segmentation results as some parts of the initializations were near to surrounding soft tissue.

4.3.5.2 Sensitivity to scaling factor *s* and rotation of MR image

In Section 4.3.2.2 we introduce a scaling factor *s* to enlarge the muscle ROI in the study image. A larger ROI may be needed to ensure that the muscle is fully enclosed in it. The ROIs with *s* = 1, 1.1, 1.2, are shown in Figure 4.22. The ROI will fail to fully enclose the muscle for *s* below 1.2.

(a)   (b)   (c)
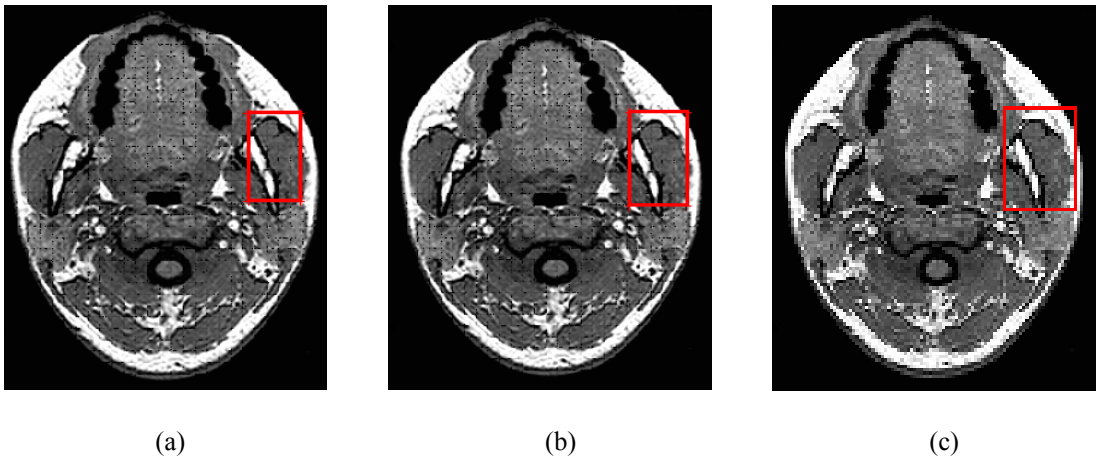
Figure 4.22: Masseter ROI when (a) *s* = 1, (b) *s* = 1.1, (c) *s* = 1.2.

We have also tested our method for its robustness to situations where the image is rotated by 15° to the left and right, or 15° up and down from the upright position. To handle such cases, s needs to be as large as 2.5. The segmentation results are shown in Figure 4.23. It can be observed that for $s = 2.5$, the ROI will contain more spurious components compared to $s = 1.3$. However, by checking for the overlap between the ROI and the template, together with morphological operators, the method is able to provide good initializations to the GVF snake; the average κ of the segmentation results shown in Figure 4.23 is greater than 90%. For values of s greater than 2.5, it can be observed that the ROI contains more soft tissue that has relatively similar intensity values to the muscle, and hence the results may not be as good. The validation shows that our proposed method is tolerant to a 15° rotation of the head. Even though the model is 2D in nature, it is tolerant to a rotation of 15° and can be applied to two neighbouring slices. This is an encouraging sign of a good model. When dealing with data sets where the head has been rotated by more than 15°, a solution will be to locate the midsagittal plane (MSP) in the image [81] and rotate the image till the MSP is in an upright position.
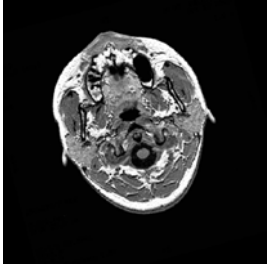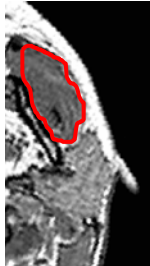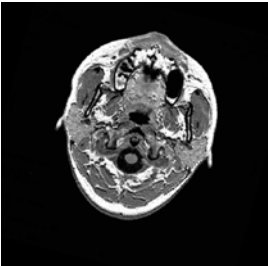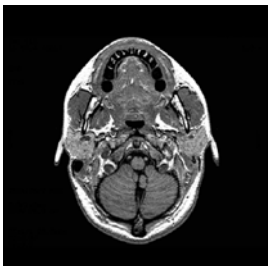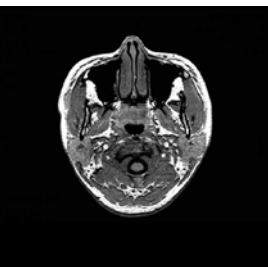
Rotated MR image $(15°anti - clockwise\_rotation)$	Muscle ROI $(s = 2.5)$	Initialization to GVF snake	Final Segmentation

Rotated MR image $(15°clockwise\_rotation)$	Muscle ROI $(s = 2.5)$	Initialization to GVF snake	Final Segmentation

Rotated MR image $(15°upwards)$	Muscle ROI $(s = 2.5)$	Initialization to GVF snake	Final Segmentation

Rotated MR image $(15°downwards)$	Muscle ROI $(s = 2.5)$	Initialization to GVF snake	Final Segmentation

Figure 4.23: Segmentation results of the masseter when image is rotated.

4.3.5.3   Justification of parameters

Throughout our work presented in Section 4.3, we have made use of FCM with three clusters. Figure 4.24 displays the segmentation results through FCM with four clusters. When we change the number of clusters from three to four, the average interval between the lower and upper thresholds is reduced from 100 to 70. The size of the remaining region after thresholding is smaller, and the probability of forming an overlap with the template at 75% or more decreases. Hence, the initialization of the GVF snake falls within the boundaries, and the GVF snake may be trapped in local minima as it propagates outwards. Compared to using FCM with three clusters, κ decreases and FNR increases. It is also possible that no region in the ROI overlaps with the template at 75%, as shown in the second result of Figure 4.24.

The objective of checking for the overlap between template and ROI is to reduce the amount of unwanted soft tissue in the ROI. It is mentioned in Section 4.3.2.2 that we set the threshold for the overlap between template and muscle ROI to be 75%. Instead of 75%, we have also experimented with 65% and 85%, with the segmentation results shown in Figure 4.25 and Figure 4.26, respectively. From Figure 4.25, it can be observed in the first and third result that, when the overlap is 65%, we are still able to obtain good segmentations of the masseter. However, it is also possible that there is minimal removal of unwanted soft tissue, as observed in the second result. The initialization of the GVF snake falls in the unwanted soft tissue and the snake does not converge to the muscle boundary. Compared to setting the overlap to 75%, κ decreases and FPR increases. In contrast, when we set the amount of overlap to be 85%, there may be excessive removal of soft tissue. Hence the initializations of the GVF snake tend to lie within the actual boundaries of the muscle as observed in Figure

4.26. In such situations, as the snake grows outward, it may be trapped in local minima and not converge to the actual boundaries. When the overlap threshold is set within (65%, 85%), the segmentation results are reasonable ($\kappa > 90\%$), so for all the experiments we set the parameter as 75%.

ROI after roughly removing fat and bone clusters	ROI after template correlation	Initialization to GVF snake	Final Segmentation
	No region in the ROI overlap with the template by 75% or more		

Figure 4.24: Segmentation results of the masseter when FCM clusters = 4.
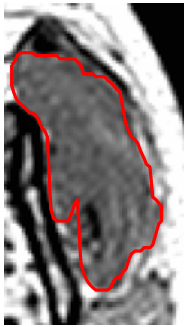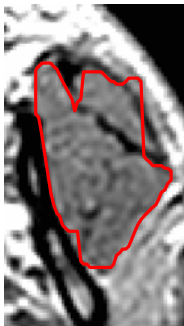
ROI after roughly removing fat and bone clusters	ROI after checking for overlap with template (65%)	Initialization to GVF snake	Final Segmentation

Figure 4.25: Segmentation results of the masseter when overlap = 65%.
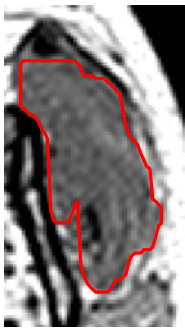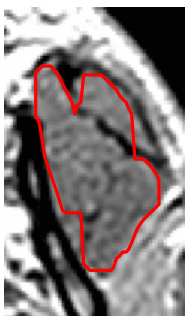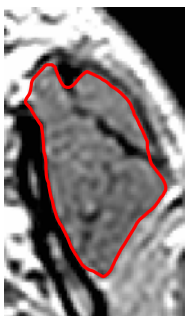
ROI after roughly removing fat and bone clusters	ROI after checking for overlap with template (85%)	Initialization to GVF snake	Final Segmentation

Figure 4.26: Segmentation results of the masseter when overlap = 85%

4.4 Segmentation of temporalis from MR image

4.4.1 Overview of proposed method

In Section 4.3, a method was presented for segmentation of the masseter, lateral and medial pterygoids. The focus of this section is on the segmentation of the temporalis. The method proposed in Section 4.3 which relies on the GVF snake does not give good segmentations of the temporalis and this will be discussed in Section 4.4.5.

The flowchart of the proposed method is in Figure 4.27. Similar to the earlier method, a spatial relationship relating the temporalis ROI to the head ROI is first obtained from reference images in the training data sets where the temporalis has been manually segmented. The temporalis ROI is automatically detected in a study image. Range-constrained thresholding [57] is used to roughly remove the fat, white matter, cerebrospinal fluid (CSF) and muscle tendon in the ROI. This is followed by the use of adaptive morphological operations to first remove the brain tissue, followed by removing other soft tissues surrounding the temporalis, before finally deriving the final segmentation.

Stage 1: Knowledge acquisition on spatial relationship between head ROI and temporalis ROI
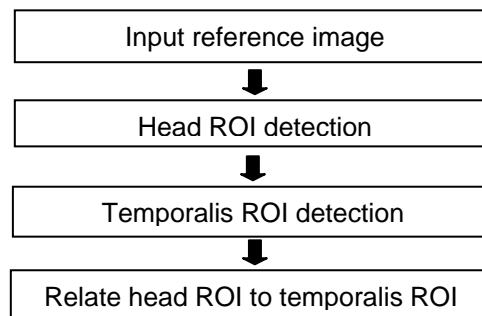
Stage 2: Segmentation of temporalis in study image

```
┌─────────────────────────────────────┐
│          Input study image          │
└─────────────────────────────────────┘
                  ⬇
┌─────────────────────────────────────┐
│          Head ROI detection         │
└─────────────────────────────────────┘
                  ⬇
┌─────────────────────────────────────┐
│   Automatic temporalis ROI detection │
└─────────────────────────────────────┘
                  ⬇
┌─────────────────────────────────────┐
│      Apply range-constrained        │
│   thresholding to temporalis ROI    │
└─────────────────────────────────────┘
                  ⬇
┌─────────────────────────────────────┐
│         Remove brain tissue         │
└─────────────────────────────────────┘
                  ⬇
┌─────────────────────────────────────┐
│   Remove soft tissue connected to   │
│              temporalis             │
└─────────────────────────────────────┘
```
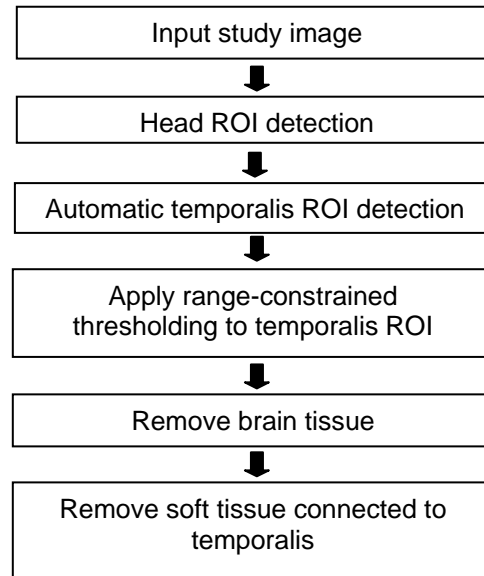
Figure 4.27: Flow-chart of proposed method.

4.4.2 The proposed method

4.4.2.1 Selection of reference slice from each MR dataset

We made use of the same MR datasets used in Section 4.3 for this section. They were acquired using a imaging protocol which scans the entire masseter and pterygoids. However, a small segment of the temporalis that is cephalad to the pinna is not imaged, but this does not have any significant effect on the development of the proposed method. We selected the reference slice for the temporalis at the level just cephalad of the pinna. Currently this selection is done manually, but it can be automated via tracking the contour of the head boundary.

4.4.2.2 Spatial relationship between temporalis and head ROIs

From the reference MR images (one from each of the five training data sets), we determine the spatial relationship between the head and temporalis ROIs. The temporalis and head ROIs are the bounding boxes of the temporalis and head regions, respectively, in a 2D MR image. This spatial relationship serves as the prior knowledge for training the system to identify the temporalis ROI in the study image.

In each reference image, the head ROI is determined through the projections of the image in the x (horizontal) and y (vertical) directions. The temporalis ROI is defined to be the bounding box of the manually segmented temporalis in the reference image.

The spatial relationship between the head and temporalis ROIs (Figure 4.28) is specified in terms of the distance between the boundaries of the head ROI and the origin of the muscle ROI.
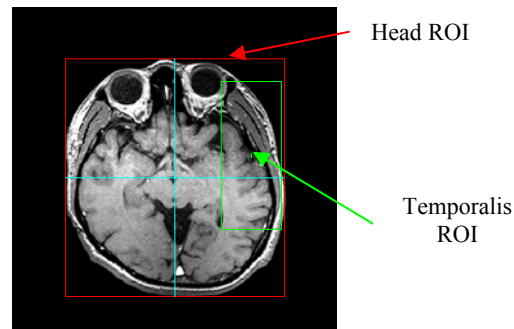
Figure 4.28: Spatial relationship between head and temporalis ROI in reference image.

For a reference image of the temporalis, the distances $b_1, w_1, j_1, k_1, v_1, h_1$ (Figure 4.29) are measured and the relative distances calculated as follows:

$$h_{1,r} = \frac{h_1}{b_1} \ , \ v_{1,r} = \frac{v_1}{w_1} \ , \ k_{1,r} = \frac{k_1}{b_1} \ , \ j_{1,r} = \frac{j_1}{w_1} \qquad (4.20)$$

To obtain a good estimate of the spatial relationship, we use the mean values of $h_{1,r}, v_{1,r}, k_{1,r}, j_{1,r}$ obtained from the five reference images.

4.4.2.3　Detection of temporalis ROI in study images

Given an image from the test data set, the system first automatically determines the head ROI based on the vertical and horizontal projections. Given that the width and length of the head ROI in the study image are w_2 and b_2, respectively, we derive equations for the spatial parameters j_2, k_2, v_2, h_2 :

$$j_2 = w_2 j_{ir} s, \ k_2 = b_2 k_{ir} s, \ v_2 = w_2 v_{ir} s, h_2 = b_2 h_{ir} s \qquad (4.21)$$

The graphical representation can be found in Figure 4.14(a) in the earlier section, where the parameters here, j_2, k_2, v_2, h_2 are represented by e_1, f_1, d_1, c_1 respectively. Parameter s is a scaling factor introduced to allow for the slight variations in location, shape and size of the muscles between different subjects. In our work, the value of s is set to 1.3. We discuss the effects of varying s in Section 4.4.5.

4.4.2.4　Range-constrained thresholding on temporalis ROI

Having determined the temporalis ROI (Figure 4.29(a)), we apply the default fuzzy C-means (FCM) clustering [78] in Matlab 7.0 for an initial segmentation of the temporalis ROI. While we use FCM with four clusters in our work, experiments show that FCM with three clusters yields similar final results. We denote the fraction of the pixels belonging to the clusters with the lowest and highest mean intensities as $x1$ and $x2$, respectively (indicated in the cumulative histogram of Figure 4.30). In the temporalis ROI, fat and white matter have relatively high intensity values compared to

the temporalis and other soft tissue. Therefore, they belong to the cluster with the highest mean intensity value. On the other hand, CSF and muscle tendon have relatively low intensity values, and hence it is reasonable to assume that they belong to the cluster with the lowest intensity. We make use of range-constrained thresholding to remove fat, white matter, CSF and the tendon from the temporalis ROI, since it has been demonstrated in [57] that it is able to provide a threshold with more consistent and robust binarization than conventional thresholding methods.

(a)	(b)	(c)	(d)	(e)
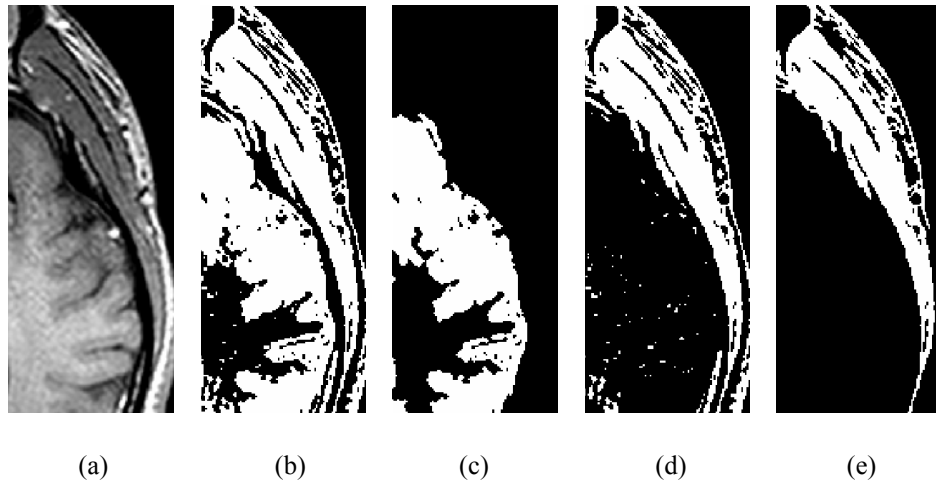
Figure 4.29: Temporalis ROI (a) before, (b) after range-constrained thresholding, (c) segmented brain tissue, (d) temporalis ROI after subtraction of brain tissue, (e) ROI with small connected components removed.
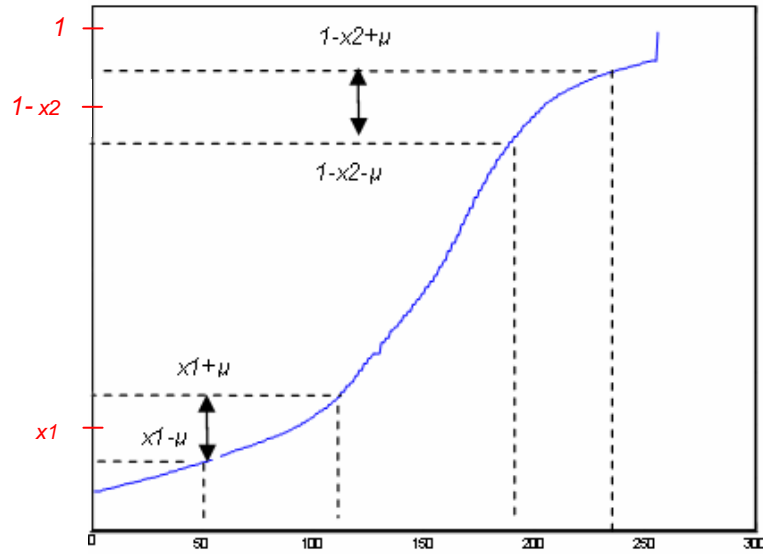
Figure 4.30: Cumulative histogram of temporalis ROI.

Two parameters associated with range-constrained thresholding, H_l^b and H_h^b, constrain the fraction range within the ROI. When determining the upper threshold for the removal of fat and white matter, we set H_l^b and H_h^b, to be $1 - x2 - \mu$ and $1 - x2 + \mu$, respectively, where μ is the tolerance to FCM's clustering error. When determining the lower threshold for the removal of CSF and tendon, we set H_l^b and H_h^b, to be $x1 - \mu$ and $x1 + \mu$, respectively. Having determined the frequency ranges, we then made use of Otsu's method [50] to determine the respective thresholds within the specified fractions. In our study, similar results are obtained for μ varying between 0.05 and 0.10. Examples of these results, as well as a discussion on FCM susceptibility to local minima, are described in Section 4.4.5.

4.4.2.5   Adaptive morphology to remove brain tissue

A substantial amount of brain tissue remains in the temporalis ROI after thresholding (Figure 4.29(b)). Although this tissue constitutes the largest proportion of the ROI, it is not feasible to use connected component labeling [79] to locate the largest connected component and remove it because there is a possibility that small parts of the temporalis may be connected to it. The use of a fixed structuring element to morphologically separate the brain and muscle tissue is also not advisable as this may cause excessive erosion to the muscle structure. Hence, we propose the use of adaptive morphology operations to separate the brain tissue from the other soft tissues.

In the temporalis ROI, we first check if the tissue on the left side of the ROI (which lies in the right hemisphere of the brain) is connected to the soft tissue on the right side of the ROI using connected components labelling. If they are, we apply morphological opening to the ROI with a circular structuring element of radius 1. If the brain tissue is still connected to the soft tissue on the right side, we apply morphological opening with the radius of the structuring element increased, by 1. As the use of morphological opening is destructive as the structuring element increases in size, the radius of the structuring element is limited to a maximum of 5. The entire process is iterated until the brain tissue is separated from the remaining soft tissue. This approach fits our work because in the temporalis ROI, the CSF is removed after range-constrained thresholding and there will be a demarcation between brain tissue and the remaining soft tissue. There may be some weak connections between them, and these are removed after applying the above adaptive morphological procedure.

The segmented brain tissue (Figure 4.29(c)) is subtracted from the temporalis ROI, leaving the other soft tissue in the ROI (Figure 4.29(d)). Small connected components are then removed from the ROI and only the largest connected component is left (Figure 4.29(e)).

4.4.2.6   Removal of unwanted soft tissue around temporalis in ROI

After applying range-constrained thresholding and morphological operations to the temporalis ROI, the presence of unwanted soft tissue persists. From empirical studies with the study images, it is observed that the top half of the temporalis ROI usually contains more unwanted components compared to the bottom half of the temporalis ROI. In the upper half, the eye and other soft tissue surrounding the temporalis are not removed during thresholding. In the lower half, there is only a slight presence of unwanted soft tissue (if any) surrounding the temporalis after range-constrained thresholding and adaptive morphological removal of the brain tissue. We provide an illustration in Figure 4.31(a) and (b), which display the top half and bottom halves, respectively, of the temporalis ROI. Comparing the two, it is clear that the former requires more processing to remove the unwanted soft tissue compared to the latter.

(a)   (b)
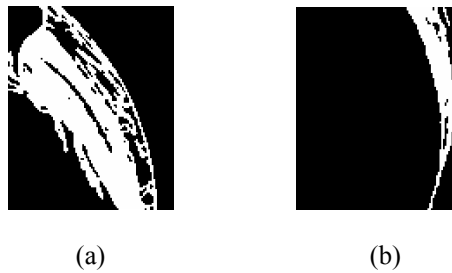
Figure 4.31: (a) Top partition, (b) bottom partition of temporalis ROI in Figure 4.29(e).

Hence, we first divide the temporalis ROI ($j_2 \times k_2$) into two equal partitions (top and bottom), with the top partition comprising the first ($j_2 / 2$) rows of the temporalis ROI

and the bottom partition comprising the next (j_2 / 2) rows. We then make use of a similar adaptive morphology technique, described in Section 4.4.2.5, to process the two partitions. For the top partition, it is assumed that no pixel belonging to the temporalis lies on the boundaries of the temporalis ROI. Hence, in our method, a check is first carried out to see if any pixel belonging to the largest connected component lies on the boundaries of the temporalis ROI. If so, morphological opening is applied to the top partition to remove small unwanted components. The structuring element used in the first iteration is a disk with radius 1. If any boundary pixel is still part of the largest connected component, we increase the disk radius by 1 and re-apply morphological opening to the original top partition. The iterations stop when the largest connected component does not have any pixels lying on the boundary of the temporalis ROI. The same process is employed on the bottom partition.

4.4.3 Experiments

The proposed method was applied to five MR study data sets. In each data set, the user is required to select the reference slice for the temporalis. We then performed 2D segmentation of the temporalis on the reference slice, as well as on the two slices superior and two slices inferior to the reference slice. Hence, a total of 25 segmentation results (five from each of the five study data sets) were obtained. The κ index, FPR and FNR which were introduced earlier in equations 4.8, 4.18 and 4.19 were used as evaluation criteria.

To further validate the proposed method, we also made use of the leave-one-out evaluation strategy [82] to evaluate the performance. With this method, all the data

sets were involved in training as well as testing, giving a total of 50 segmentation results.

4.4.4 Results

A set of results obtained after each stage of operation in our method is shown in Figure 4.32. The results have been obtained using $s = 1.3$. Numerical validations are performed on the 25 segmentation results, using five training sets and five test sets by checking for their consistencies with the ground truths (Table 4.6). The mean κ, FPR and FNR are 90.2%, 8.7% and 10.9%, respectively.

Using the leave-one-out evaluation strategy, the mean κ, FPR and FNR obtained from 50 results are 90.5%, 9.1% and 9.8%, respectively. The results (Table 4.7) are similar to those obtained earlier.
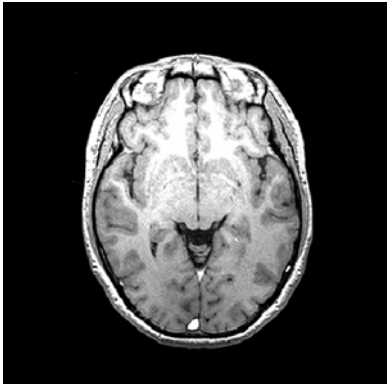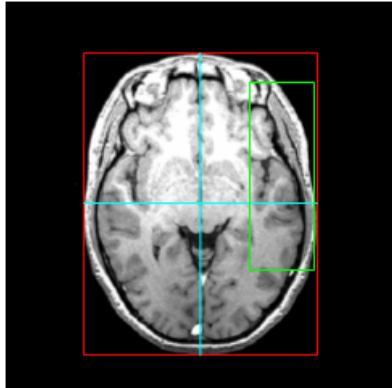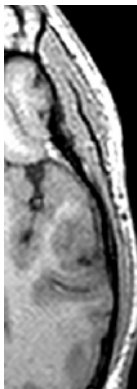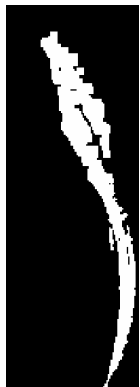
Original MR image	MR image with identified temporalis ROI	Original temporalis ROI

Binary ROI after range-constrained thresholding	Extracted brain tissue via adaptive morphology operators	Temporalis ROI after subtraction of brain tissue	ROI after removing small connected components

Upper portion of ROI after adaptive morphology operators	Lower portion of ROI after adaptive morphology operators	Final segmentation of the temporalis

Figure 4.32: Results after each stage of segmentation.

Table 4.6: Numerical validation results for segmentation of temporalis.

Image Index	κ (%)	FPR (%)	FNR (%)	Image Index	κ (%)	FPR (%)	FNR (%)
1	91.7	8.1	8.5	14	91.1	6.8	11.0
2	88.5	9.8	13.2	15	88.9	10.1	12.1
3	85.2	11.6	18.0	16	87.8	11.8	12.6
4	92.0	6.3	9.7	17	92.1	7.5	8.3
5	89.7	8.5	12.1	18	92.8	5.5	8.9
6	90.6	7.7	11.1	19	90.2	8.8	10.8
7	88.6	10.4	12.4	20	91.5	6.8	10.2
8	92.2	5.8	9.8	21	89.5	9.1	11.9
9	89.8	9.8	10.6	22	91.0	10.8	7.2
10	91.6	8.8	8.0	23	88.1	9.8	14.0
11	92.5	7.1	7.9	24	87.8	12.1	12.3
12	89.5	11.8	9.2	25	90.8	7.5	10.9
13	92.0	4.5	11.5	**Mean**	**90.2**	**8.7**	**10.9**

Table 4.7: Validation results using leave-one-out evaluation strategy.

Test Set	Image	κ (%)	FPR (%)	FNR (%)	Test Set	Image	κ (%)	FPR (%)	FNR (%)
1	1	85.2	11.6	18.0	6	26	87.8	11.8	12.6
	2	88.5	9.8	13.2		27	92.1	7.5	8.3
	3	91.7	8.1	8.5		28	92.8	5.5	8.9
	4	92.0	6.3	9.7		29	91.5	6.8	10.2
	5	89.7	8.5	12.1		30	90.2	8.8	10.8
2	6	88.6	10.4	12.4	7	31	87.8	12.1	12.3
	7	90.6	7.7	11.1		32	89.5	9.1	11.9
	8	92.2	5.8	9.8		33	91.0	10.8	7.2
	9	91.6	8.8	8.0		34	90.8	7.5	10.9
	10	89.8	9.8	10.6		35	88.1	9.8	14.0
3	11	89.5	11.8	9.2	8	36	89.8	9.7	10.7
	12	92.0	4.5	11.5		37	91.5	10.1	6.9
	13	92.5	7.1	7.9		38	93.1	6.8	7.1
	14	91.1	6.8	11.0		39	91.8	8.1	8.3
	15	88.9	10.1	12.1		40	90.5	8.8	10.2
4	16	88.7	10.5	12.1	9	41	89.8	11.5	8.9
	17	90.4	9.2	10.1		42	91.6	10.8	6.1
	18	92.3	7.1	8.3		43	93.4	8.1	5.1
	19	91.2	8.8	9.0		44	92.5	6.5	8.5
	20	86.9	13.5	12.7		45	89.3	12.3	9.1
5	21	90.7	9.4	9.2	10	46	90.9	9.5	8.7
	22	91.3	7.2	10.2		47	91.7	8.3	8.3
	23	93.0	8.7	5.4		48	92.6	7.7	7.1
	24	90.5	11.8	7.2		49	90.8	12.1	6.3
	25	87.9	12.3	11.9		50	89.1	11.8	10.1
	Mean κ = 90.5%				***Mean FPR = 9.1%***			***Mean FNR = 9.8%***		

4.4.5 Discussion

4.4.5.1 Accuracy of segmentation results

The temporalis has a complex structure as observed in the MR images. This, together with the fact that it is surrounded by soft tissue with similar intensity values, has made its segmentation from MR images challenging. The proposed method, which involves thresholding and morphological operations, is able to produce segmentations with average κ of 90%.

4.4.5.2 On dividing the ROI before further processing

Based on empirical studies, we divided the temporalis ROI into two equal partitions before further processing, as mentioned in Section 4.4.2.6. The presence of the orbit and unwanted soft tissue surrounding the temporalis, even after range-constrained thresholding and extraction of the brain tissue, means that the top half of the ROI requires more processing than the bottom half. We make use of morphological opening to separate the temporalis from the unwanted components. With reference to Figure 4.31(a) and (b), based on our method, the top partition undergoes morphological processing whereas the bottom partition does not, and hence the original structure of the temporalis in the bottom partition is preserved. If we had processed the temporalis ROI as a whole, we would find that the bottom half of the temporalis ROI undergoes the same morphological opening as the upper half, and the resulting structure will not be a good representation of the temporalis.

<div align="center">(a)   (b)</div>
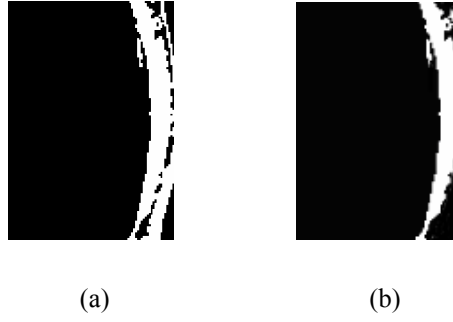
Figure 4.33: Bottom partition of temporalis ROI (a) before, (b) after processing.

To further illustrate our method, Figure 4.33(a) displays the bottom partition from another temporalis ROI. Unlike that in Figure 4.31(b), it requires morphological processing to break the connections between the temporalis and its surrounding soft tissue. Figure 4.33(b) displays the result after our method has successfully removed the unwanted soft tissue.

4.4.5.3 Sensitivity to scaling factor s and rotation of MR image

We introduce a scaling factor s in Section 4.4.2.3 to enlarge the temporalis ROI in the study image. A larger ROI may be needed to ensure that the muscle is fully enclosed. As illustrated in Figure 4.34, when $s = 1$, the ROI fails to enclose the entire temporalis. From experiments, we obtain a minimum value of $s = 1.3$ to ensure the ROI encompasses the temporalis. In addition, we have also experimented with $s = 1.5, 1.75,$ 2.0 and 2.5, with the results in Figure 4.34. The segmentation results, with mean κ around 90%, are comparable to the result obtained using $s = 1.3$. The advantage of using a larger value of s is that it allows the ROI to fully enclose the temporalis even when the images have been rotated. This is analogous to a situation where the subject's head is rotated for the scan. However, when s is increased to a large value, the proposed method may fail to produce the expected segmentation results. Figure 4.35

displays the corresponding images when $s = 3.5$ and the temporalis is not segmented correctly.
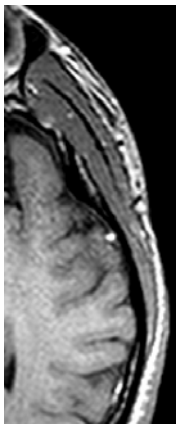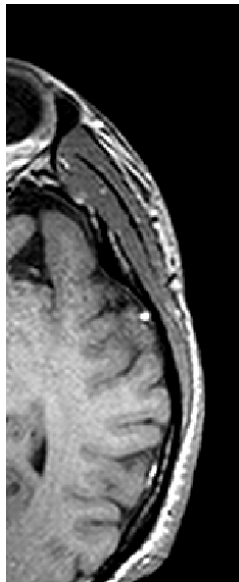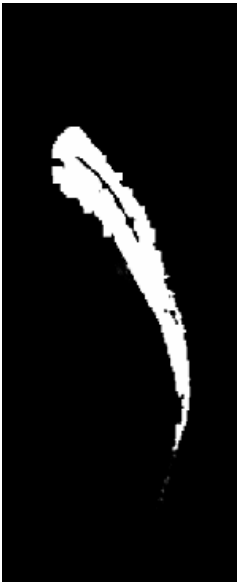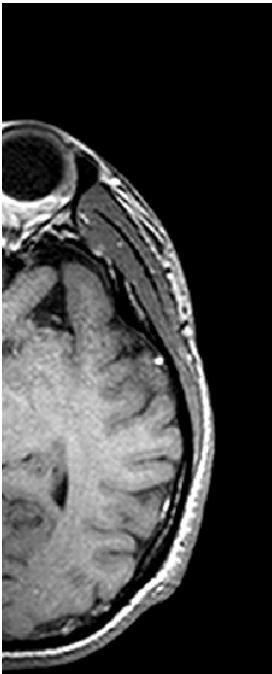
	s = 1.0		s = 1.5		s = 1.75	
Original temporalis ROI	Final temporalis segmentation	Original temporalis ROI	Final temporalis segmentation	Original temporalis ROI	Final temporalis segmentation	

s = 2.0		s = 2.5	
Original temporalis ROI	Final temporalis segmentation	Original temporalis ROI	Final temporalis segmentation

Figure 4.34: Segmentation results when parameter s is varied.
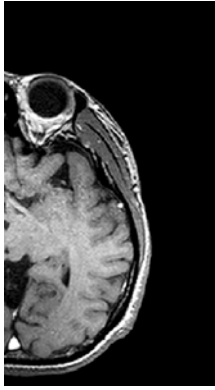
Original ROI of temporalis	Binary ROI after range-constrained thresholding	Extracted brain tissue

Temporalis ROI after subtraction of brain tissue	Final Segmentation after adaptive morphology operators

Figure 4.35: Segmentation results obtained when $s = 3.5$.

Besides testing for its sensitivity to scaling factor s, we also tested the proposed method for its robustness in scenarios where the image has been rotated by 15° clockwise and anti-clockwise, or 15° up and down from the upright position. The value of s used is 2.5. The segmentation results are comparable to those obtained when the images are not rotated and the average κ is around 90%. We note that for $s = 2.5$, the ROI will contain more spurious components compared to $s = 1.3$. However, our method is sufficiently robust to overcome this problem and produce good

segmentations of the temporalis. Where there is a wide rotation of the head (>15°), a possible solution will be to locate the midsagittal plane (MSP) in the image [81] and rotate the image till the MSP is in an upright position before applying the proposed method. Besides the MSP, locating other anatomical features, such as the eyes or medulla could also help in the localisation and make our proposed method more rotationally invariant.

The segmentation results indicate that the proposed method is capable of segmenting the temporalis from 2D MR images. The advantages with the proposed method are that it is effective when the ROI is enlarged to encompass more unwanted components and when the images are rotated. These signs are encouraging.

4.4.5.4   Sensitivity to choice of reference slice

As mentioned in Section 4.4.2.1, we selected the reference slice for the temporalis at the level just cephalad of the pinna. Using this reference slice, we obtain a segmentation accuracy of around 90%. In addition, we tested the robustness of the proposed method to different selected reference slices. We selected as reference slice the image slices that are 5 slices superior and 5 slices inferior to the proposed reference. The values of κ, FPR and FNR are 87.0%, 17.2%, 7.6%, respectively, when the reference slice is 5 slices superior to the proposed reference, and 87.6%, 20.0%, 2.7%, respectively, when the reference slice is 5 slices inferior to the proposed reference. The results are similar to those obtained when the proposed reference is used. Selecting the reference slice to be at the level just cephalad of the pinna offers the possibility of automating the process via tracking the contour of the head boundary.

4.4.5.5 Sensitivity of range-constrained thresholding to fraction range and comparison with FCM and Otsu methods

As mentioned in Section 4.4.2.4, there are two parameters associated with range-constrained thresholding, namely H_l^b and H_h^b, that constrain the fraction range within the ROI. H_l^b and H_h^b can be varied by adjusting μ, which we define as the tolerance to FCM's clustering error. We experimented with values of μ ranging from 0.05 to 0.10 and obtained similar results. An illustration of the results produced by range-constrained thresholding using $\mu = 0.05$ and $\mu = 0.10$ is shown in Figure 4.36.

Original temporalis ROI	Result using range-constrained thresholding (μ=0.05)	Result using range-constrained thresholding (μ=0.10)	Result using FCM clustering	Result using Otsu method
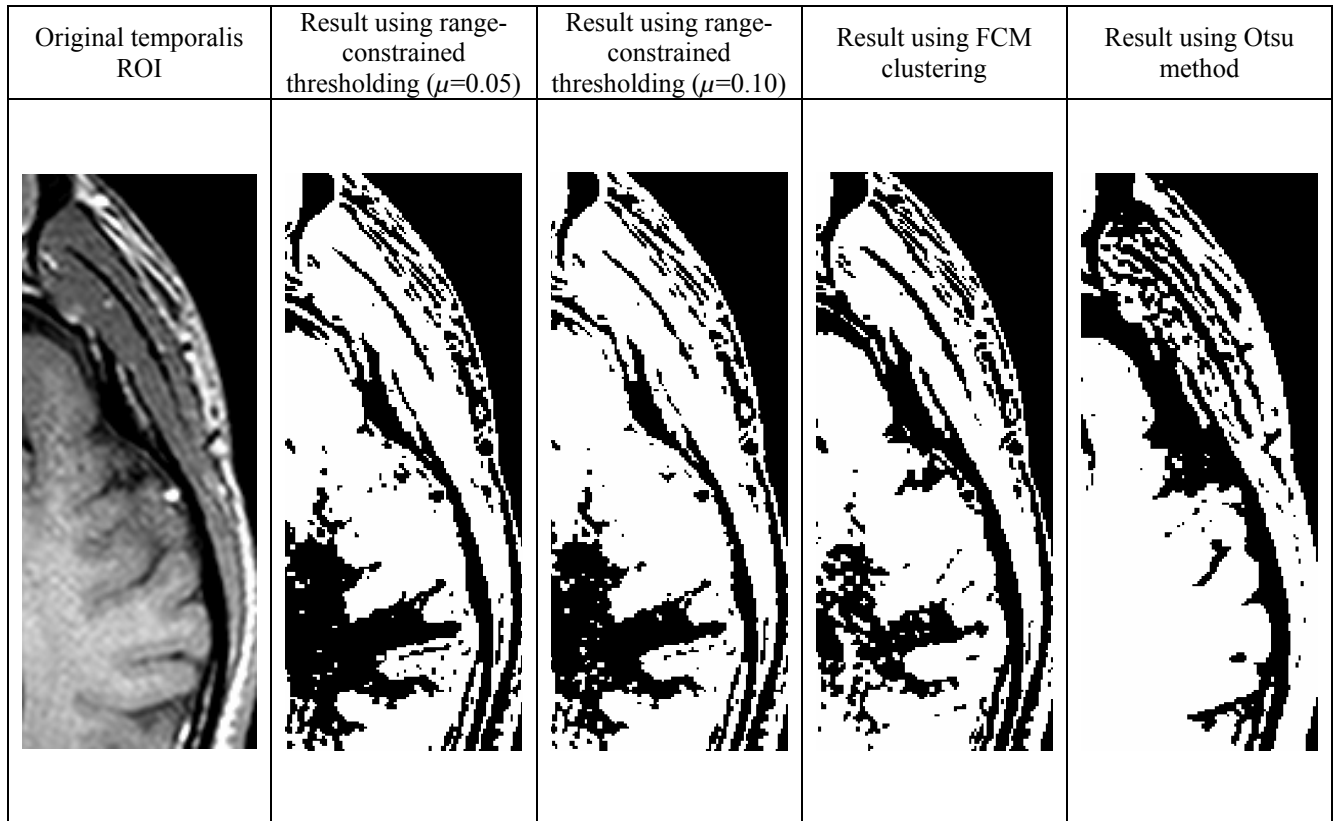
Figure 4.36: Resulting temporalis ROI using different thresholding techniques.

We have also compared our method against FCM clustering and Otsu's method, with the results in Figure 4.36. It is seen that Otsu's method misclassified some brain tissue

and parts of the temporalis as background. FCM clustering produces satisfactory results but it also has the problem of misclassifying some boundary brain tissue. The susceptiability of FCM to local minima depends on the complexity of the feature space as well as the initial condition. If the system contains local minima and the initial state is located near a local minimum, then FCM will converge to the local minimum. On the other hand, similar to variance-based thresholding methods, FCM tends to result in a type of systematic error which selects the threshold towards the component with the larger probability or larger variance [83]. Nevertheless, FCM could provide a good initial solution, which can be improved by methods incorporating some prior knowledge such as range-constrained thresholding.

4.4.5.6   Comparison with results obtained using GVF snake

We have compared the results obtained using our method against those obtained using the GVF snake, which is one of the popular techniques used in medical image segmentation. We initialize the GVF snake with points close to the boundaries of the temporalis, and the results are shown in Figure 4.37. The value of κ, FPR and FNR are 80.8%, 26.7%, 12.1%, respectively, for the first result in Figure 4.37, and 84.7%, 14.7%, 15.7%, respectively, for the second result in Figure 4.37. Comparing these results against those in Figures 4.32 and 4.34, we note that our method produces superior results. The GVF snake does not segment the temporalis accurately but, instead, converges to the muscle tendon within the temporalis (Figure 4.37). In contrast, the proposed method is able to retain the thin space occupied by the tendon (Figures 4.32 and 4.34). Another indication that our method produces superior results is that it manages to delineate the temporalis from its surrounding tissue in narrow and concave regions, unlike the use of the GVF snake, which propagates inwards and away

from the concave boundaries despite the initializations being made near them. A possible reason for this is the settings of the parameters in the GVF snake.
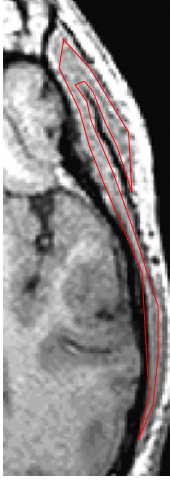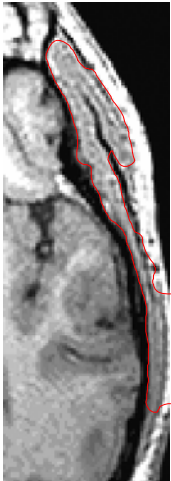
Original temporalis ROI	GVF snake initialization	Final segmentation	Segmented image

Figure 4.37: Segmentation results obtained using GVF snake.

Chapter 5

Determining dominant slices for patient-specific masticatory muscles modeling

5.1 Introduction

Techniques for segmenting the masticatory muscles from MR images were presented in the previous chapters. They were validated and tested for their robustness. The work found in [84, 85] are examples where 2D methods are applied sequentially to the slices of a 3D volumetric data. For the segmentation of masticatory muscles, repeatedly applying our proposed 2D methods to all the 2D slices in the MR dataset may not achieve good segmentation results. This is because in a 3D MR dataset, there are slices where no clear boundary exists between the muscle and the surrounding tissue. As such, we will need to make use of the neighbouring slices which provide additional information.

In this chapter, we describe an approach for obtaining patient-specific models of the masticatory muscles from the MR images of the head. We determine the set of dominant slices that together best represent the salient features of the 3D muscle shape from training datasets. Candidates for the dominant slices are identified by shape- and area-based criteria, and this is followed by fuzzy-c-means clustering [78] to determine the actual slices. Manual segmentation is carried out on these dominant slices on the patient dataset, with shape-based interpolation [28] then applied to construct accurate muscle model. Compared to the common practice of manually segmenting the

masticatory muscles from all MR slices [15, 18], there is significant time-savings as each MR dataset used in our work consists of nearly 170 slices.

In an initial work [86] done, a method was proposed for the extraction of the masseter utilizing knowledge from only three MR slices (starting slice, ending slice, as well as the slice with the largest cross-sectional muscle area) to extract the entire masseter. With only three slices, the shape and size variations of the muscle are not adequately captured, as illustrated in Figure 5.1. A better representation can be obtained with the use of more slices. However, the selection of these slices is not trivial as a random or an equally-spaced selection is not likely to lead to an accurate model. In our approach, we propose a set of shape- and area-based criteria for determining the candidates for these dominant slices, with clustering used to establish the final dominant slices.

(a)   (b)
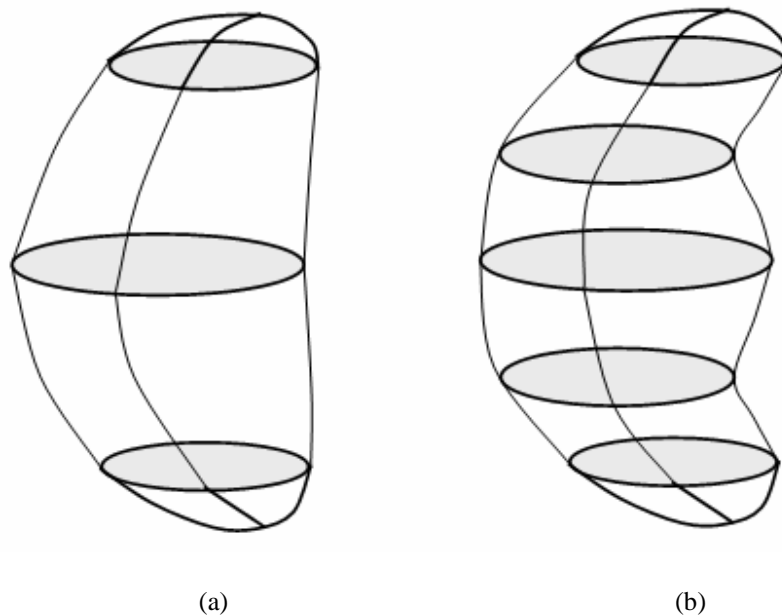
Figure 5.1: (a) Model used in earlier method, (b) Model used in current method.
(Dominant slices are represented by shaded ellipses)

5.2 Overview of proposed work

In the training sets, the left and right masseters and the lateral and medial pterygoids were first manually segmented by an expert radiologist. From these training sets, we determine the locations of the dominant slices for each of the muscles using a set of criteria that capture the main features of the muscle shape. Given a patient dataset, we carry out 2D segmentation of the muscle on the dominant slices, followed by shape-based interpolation to construct the 3D muscle model.

5.3 The proposed method

5.3.1 Normalization of slice location

The masticatory muscles vary in size between humans, and therefore the number of MR slices that they occupy differs. We use the normalized slice index, I_n, so that the locations of the dominant slices are size-invariant. For a slice I_r, its normalized value is:

$$I_n = \frac{I_r - I_i}{I_f - I_i} \tag{5.1}$$

where I_i and I_f refer, respectively, to the locations of the slices where the targeted muscle first and last appears. They are identified through human intervention.

5.3.2 Determination of dominant slices

Dominant slices are obtained from training sets. In order for an accurate patient-specific muscle model to be built, the MR slices that capture the main features of the muscle shape have to be determined. We define the following set of criteria for locating the candidates for the dominant slices:

- Slices where the muscle first and last appears (Figure 5.2).

- Slices where the muscle area pattern undergoes a change, i.e., the turning points in the plot of cross-sectional muscle area *vs* I_n (Figure 5.3).

- Slices in which the structure of the masticatory muscle undergoes a significant change in orientation, i.e., the turning points in the plot of the muscle centroid on each slice *vs* I_n (Figure 5.4).
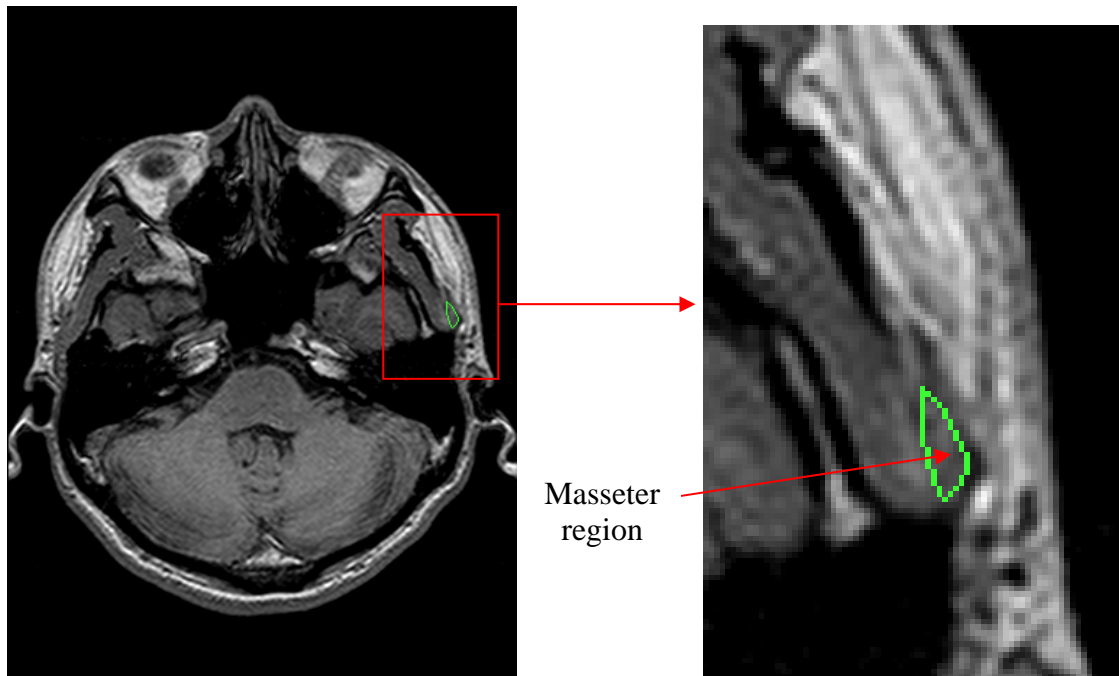
Masseter region

Figure 5.2: Sample MR slice where masseter first starts to appear.
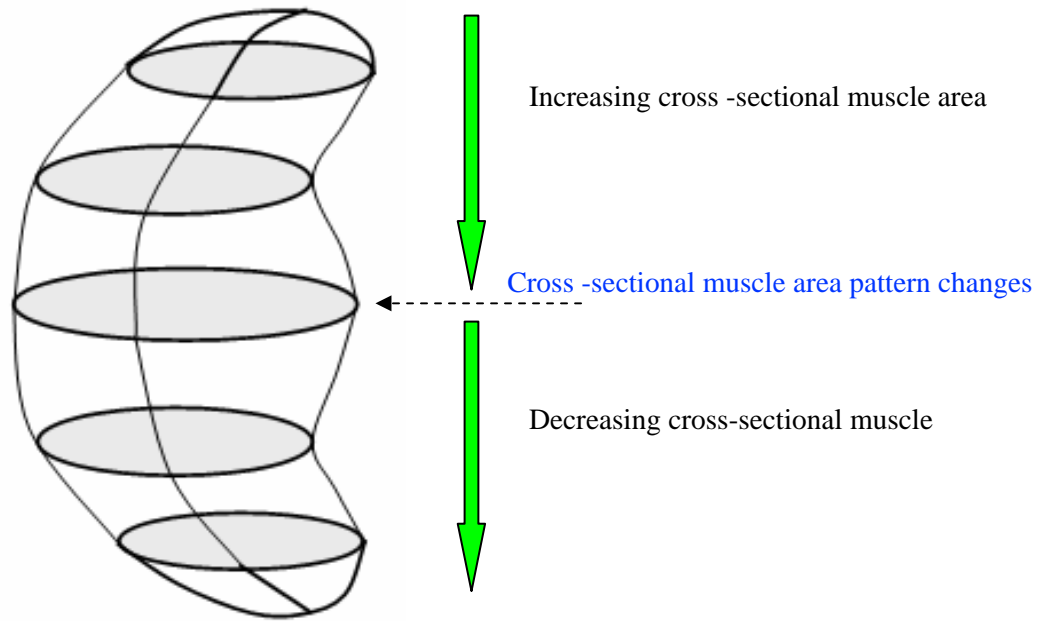
(a)
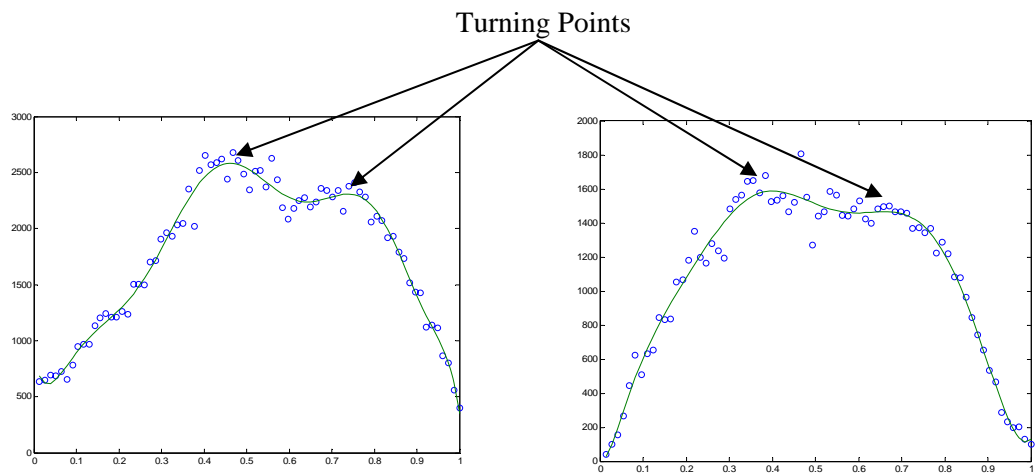
(b)

Figure 5.3: (a) Change in cross-sectional muscle area pattern,

(b) Turning points in the plot of cross-sectional muscle area $vs\ I_n$.
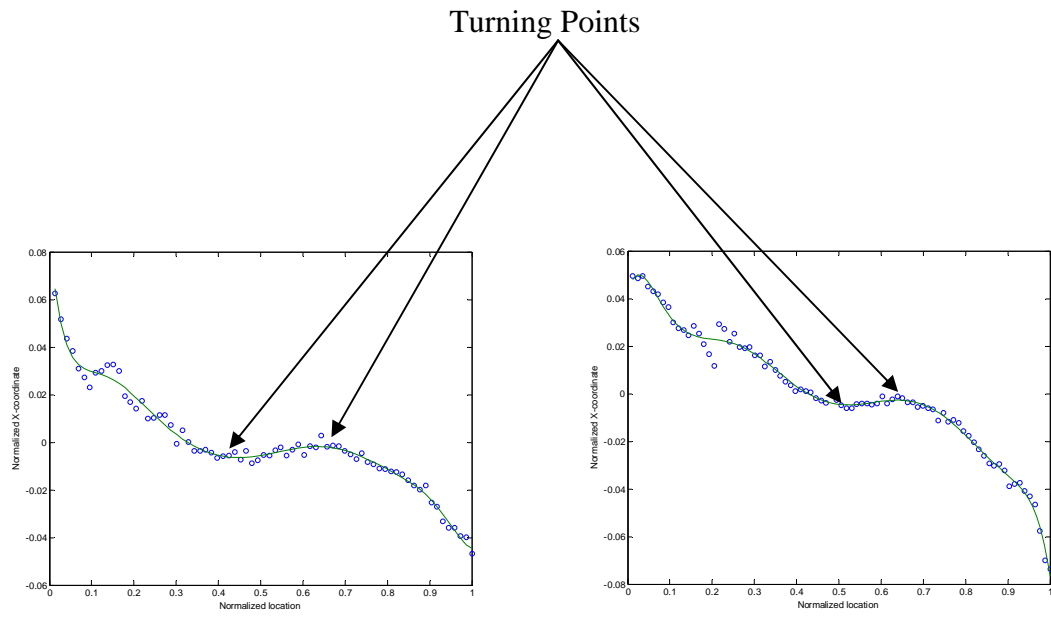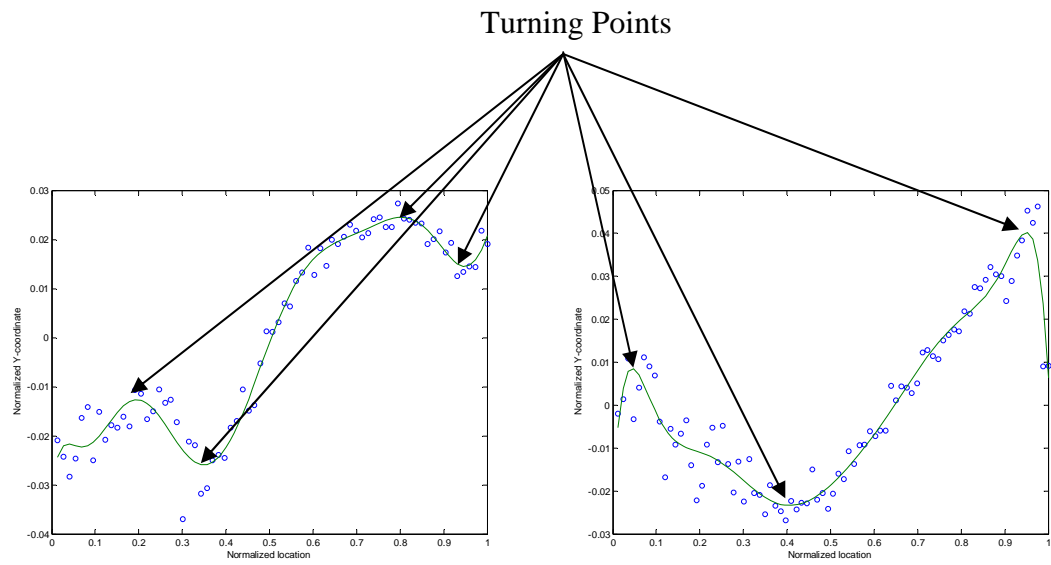
Figure 5.4: (a) x-coordinate of muscle region centroid $vs\,I_n$,

(b) y-coordinate of muscle region centroid $vs\,I_n$.

Slices I_i and I_f are considered dominant slices because they have to be identified correctly in order for an accurate model to be built. Furthermore, the muscle regions in I_i and I_f are often indistinct due to their smaller areas, and a high degree of clinical expertise is required for their recognition.

To build an accurate muscle model, it is important to locate the slices where the cross-sectional muscle area pattern changes. These slices can be found at the turning points in the plot of cross-sectional muscle area vs I_n . The masticatory muscles were manually segmented by an expert radiologist in each of the training sets, and the cross-sectional muscle areas were measured and their values plotted against the normalized slice location. A spline with 10 polynomial coefficients was then fitted onto the points using the spline-fitting function in MATLAB 7.0. Section 5.6.3 presents a discussion on number of coefficients used. On each of the spline-fitted curves, the normalized slice locations at the turning points of the spline are selected as the candidate slices.

Dominant slices also exist where the muscle undergoes a significant change in orientation. From each of the training datasets, the centroid of the manually segmented muscle region on each slice is measured in terms of their x and y coordinates. The centroid of a muscle region R is defined in terms of the moments m_{ij}:

$$(\bar{x}, \bar{y}) = \left(\frac{m_{10}}{m_{00}}, \frac{m_{01}}{m_{00}} \right) \tag{5.2}$$

where

$$m_{ij} = \sum_{x \in R} \sum_{y \in R} x^i y^j R(x, y) \tag{5.3}$$

The x coordinate $(\bar{x})$ of the muscle centroid on each of the slices is plotted against the normalized slice locations, and a spline was fitted onto the plotted points as described earlier. The same process is applied to the y coordinate $(\bar{y})$. The turning points on each of the spline-fitted graphs are selected as the candidate slices.

5.3.3 Clustering of candidate slice locations

Clustering refers to the partitioning of a collection of data points into clusters such that objects inside the same cluster show similarity in the defined features. Our objective here is to cluster the N identified candidates, denoted by their slice indices d_i, to determine the dominant slices. The set of candidates is denoted by D, i.e.,

$$D = \{d_i, i = 1,2,...,N \, / \, d_i \in R\} \tag{5.4}$$

FCM clustering, which is useful in dealing with nontrivial data and uncertainties [78], is applied to set D to obtain c classes. The locations of the dominant slices are given by the cluster centers.

The class prototypes are represented by a $c \times 1$ matrix V, with the kth ($k = 1,2,...,c$) row representing the prototype of the kth class. The cluster is represented by a $c \times N$ matrix U. The element u_{ki} of matrix U represents the membership of the ith data point to the kth class. With FCM clustering, u_{ki} ranges from 0 to 1 and characterizes the degree of similarity between the ith data point and the kth class prototype:

$$\sum_{k=1}^{c} u_{ki} = 1, \forall i \, ; \quad 0 \le u_{ki} \le 1, \forall k,i \tag{5.5}$$

The matrix U is found by minimizing the generalized least squares within-group square error function J :

$$J = \sum_{k=1}^{c} \sum_{i=1}^{N} u_{ki}^{b} \left\| d_i - v_k \right\|^2 \qquad (5.6)$$

where $b \in [1, \infty)$ is a weighting exponent on each fuzzy membership and $\| \ \|$ denotes the Euclidean distance. u_{ki} and v_k are updated as follows:

$$u_{ki} = \frac{1}{\sum_{l=1}^{c} \left(\frac{\left\| d_i - v_k \right\|}{\left\| d_i - v_l \right\|} \right)^{2/(b-1)}}, \quad k = 1, 2, ..., c \; ; \; i = 1, 2, ..., N \qquad (5.7)$$

$$v_k = \frac{\sum_{i=1}^{N} u_{ki}^{b} d_i}{\sum_{i=1}^{N} u_{ki}^{b}}, \quad k = 1, 2, ..., c \qquad (5.8)$$

The default FCM function available in MATLAB 7.0 is used in the implementation of our work. The parameters and their values are: weighting component $b = 2.0$, maximum number of iterations = 100, minimum amount of improvement = 1×10^{-5}. By varying the number of classes, c, we are able to investigate the effects that the number of dominant slices has on the accuracy of the muscle models.

5.3.4 Shape-based interpolation

Having determined the locations of the dominant slices, segmentation of the masticatory muscles from the corresponding 2D slices in the test dataset is then carried out. We apply the shape-based interpolation algorithm proposed in [28] to create the models for each of the masticatory muscles. In this approach, each object is grouped into two types of components, namely simple and complex. A non-uniform rational B-spline (NURBS)-based method and a distance map-based method are designed for

interpolation of the simple components and the complex components, respectively. For each masticatory muscle, once all the object points have been interpolated, the results are combined hierarchically in a bottom-up manner to produce the interpolation of the entire muscle. In the process, knowledge-based and heuristic strategies are used to preserve various topological relationships. A comprehensive description of this hybrid approach can be found in [28]. This approach has also been validated quantitatively and effectively used for interpolation of the Schaltenbrand-Wahren atlas [87]. The work presented here differs from earlier work as the determination of dominant slices is carried out for accurate patient-specific masticatory muscles modeling. Instead of making use of all available slices, which was the case in earlier work, only the dominant slices were used to build the models in the work presented here.

5.4   Experiments

The leave-one-out method [82] is used to evaluate the proposed method and fifteen datasets from adult volunteers were used. With this evaluation method, all the datasets were involved in training as well as testing. A total of 90 masticatory muscles models (left and right masseters, lateral and medial pterygoids) belonging to fifteen subjects were built. To evaluate the consistency between the patient-specific models and the manual segmentations, we again make use of the κ index [74] which was introduced in the previous chapter.

For each of the 90 muscle models, the number of dominant slices c was varied from 5 to 10 and their influence on the accuracy was investigated. In our MR datasets, which consist of 1mm slices, the masseter, lateral pterygoid and medial pterygoid muscles occupy approximately 80, 35 and 50 slices respectively. It is pertinent to study how

model accuracy varies with the fraction of slices used, and to this end we introduce the compression ratio, η,

$$\eta = \frac{c}{T_{slice}} \tag{5.9}$$

where c is the number of dominant slices used for the targeted muscle and T_{slice} is the number of slices occupied by the targeted muscle.

Other experiments include testing our proposed approach for its robustness against the selection of I_i and I_f which was performed manually and studying the effects of varying the number of polynomial coefficients used in the spline-fitting process.

5.5   Results

We provide sample plots of cross-sectional muscle area vs I_n which were obtained in our experiments. The plots for the masseters, lateral pterygoids and medial pterygoids are in Figures 5.5–5.7 respectively. Sample plots of x- and y-coordinate of centroids belonging to muscle region on each slice vs I_n for the masseters. lateral pterygoids and medial pterygoids are in Figures 5.8–5.10 respectively. The mean graphs obtained from the datasets belonging to the fifteen subjects are shown in the bottom row of Figures 5.5–5.10. It should be noted that determination of the candidates for dominant slices is not performed on the mean graphs in order to avoid missing out on potential candidates.

Left Masseter	Right Masseter
Plot of cross-sectional muscle area on each slice (in terms of pixels) against normalized slice location	Plot of cross-sectional muscle area on each slice (in terms of pixels) against normalized slice location

Figure 5.5: Samples of cross-sectional muscle area *vs* I_n for masseters.

Left Lateral Pterygoid	Right Lateral Pterygoid
Plot of cross-sectional muscle area on each slice (in terms of pixels) against normalized slice location	Plot of cross-sectional muscle area on each slice (in terms of pixels) against normalized slice location
Mean	Mean
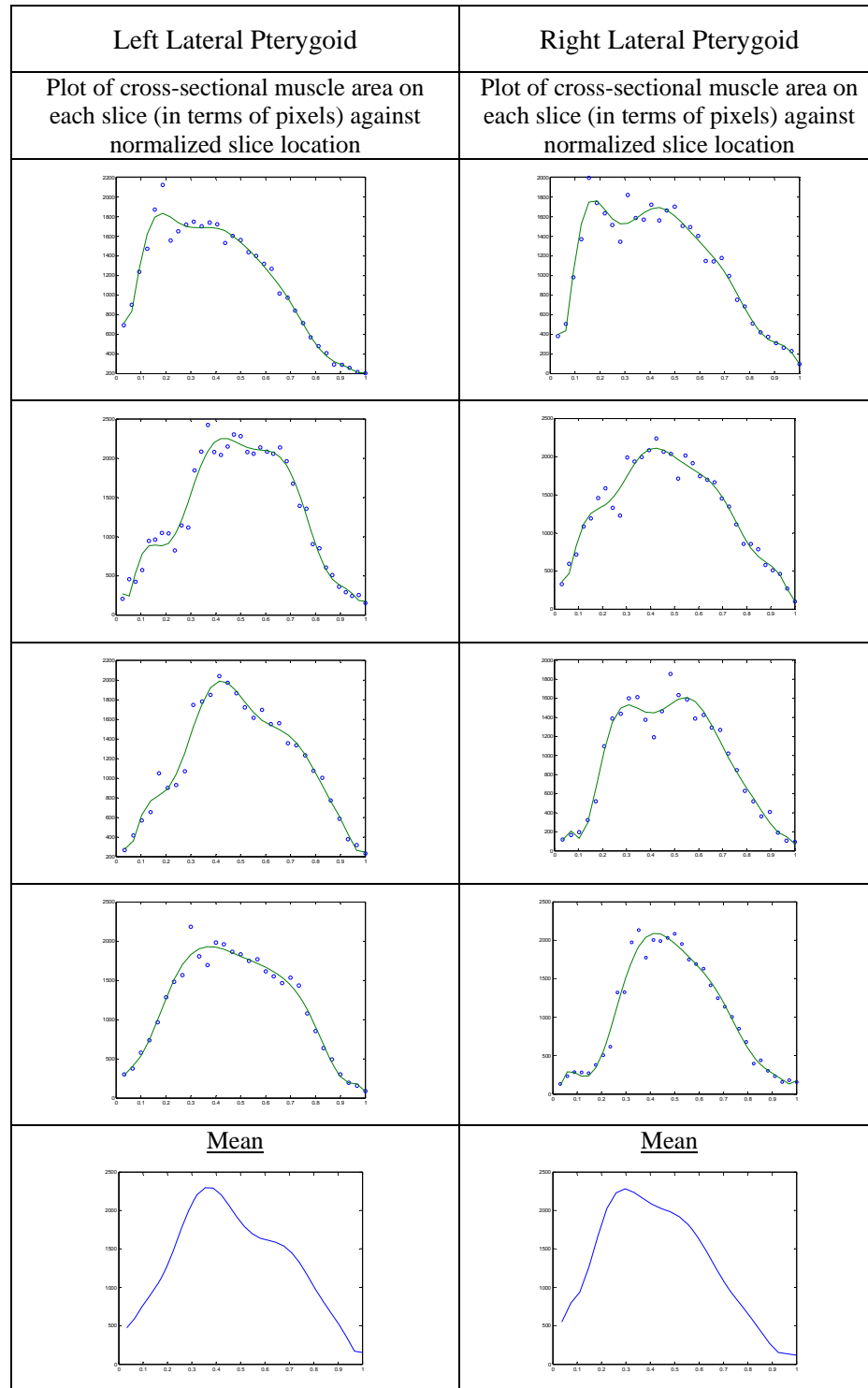
Figure 5.6: Samples of cross-sectional muscle area *vs* I_n for lateral pterygoids.

Left Medial Pterygoid	Right Medial Pterygoid
Plot of cross-sectional muscle area on each slice (in terms of pixels) against normalized slice location	Plot of cross-sectional muscle area on each slice (in terms of pixels) against normalized slice location
<u>Mean</u>	<u>Mean</u>
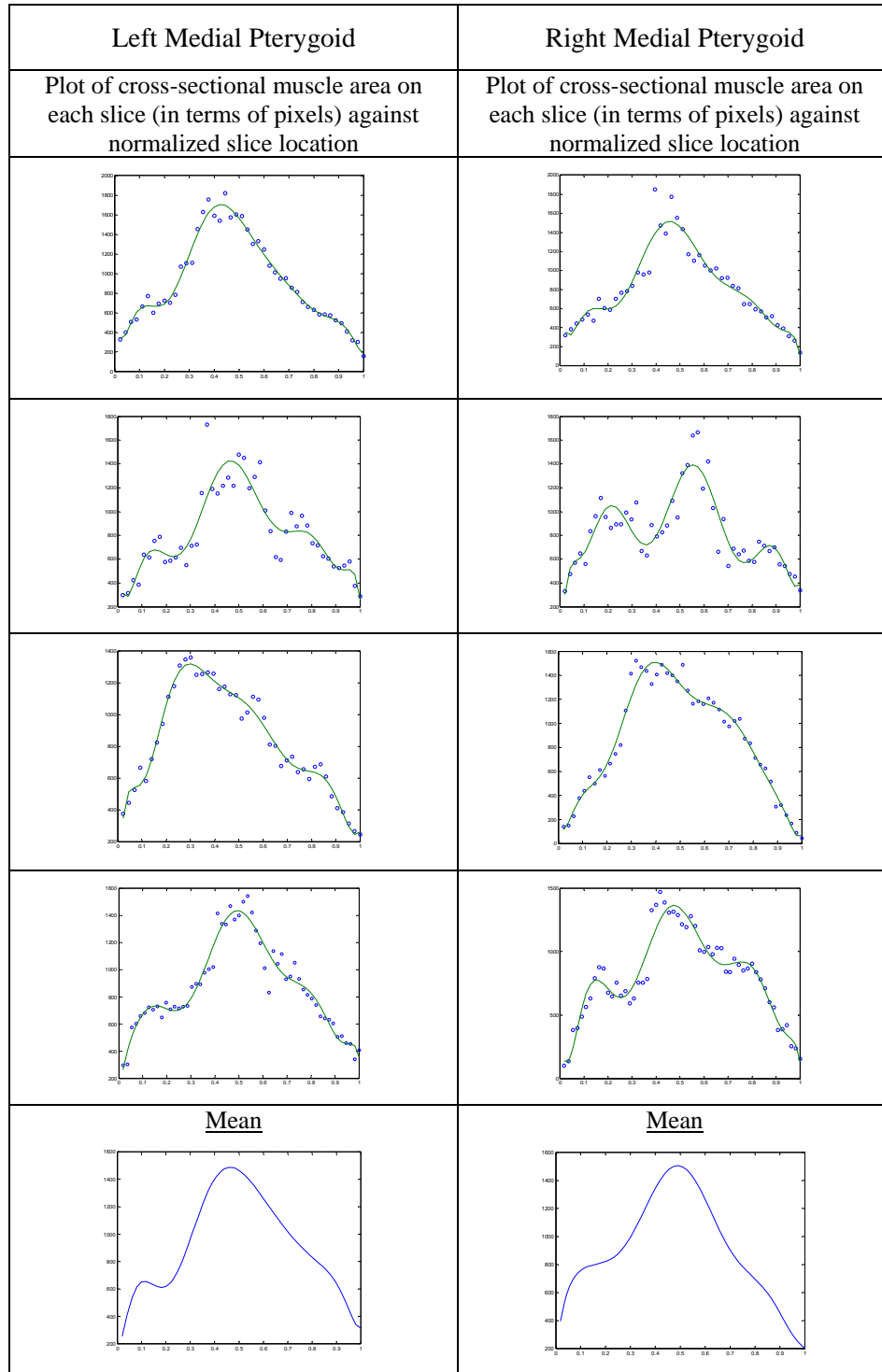
Figure 5.7: Samples of cross-sectional muscle area *vs* I_n for medial pterygoids.

Left Masseter	Right Masseter
Plot of x-coordinate of muscle region centroid against normalized slice location	Plot of x-coordinate of muscle region centroid against normalized slice location

(a)

Left Masseter	Right Masseter
Plot of y-coordinate of muscle region centroid against normalized slice location	Plot of y-coordinate of muscle region centroid against normalized slice location
Mean	Mean

(b)

Figure 5.8: Samples of (a) x-coordinate, (b) y-coordinate of centroid of muscle region

vs I_n for masseters.

Left Lateral Pterygoid	Right Lateral Pterygoid
Plot of x-coordinate of muscle region centroid against normalized slice location	Plot of x-coordinate of muscle region centroid against normalized slice location
<u>Mean</u>	<u>Mean</u>

(a)

Left Lateral Pterygoid	Right Lateral Pterygoid
Plot of y-coordinate of muscle region centroid against normalized slice location	Plot of y-coordinate of muscle region centroid against normalized slice location
Mean	Mean

(b)

Figure 5.9: Samples of (a) x-coordinate, (b) y-coordinate of centroid of muscle region

vs I_n for lateral pterygoids.

Left Medial Pterygoid	Right Medial Pterygoid
Plot of x-coordinate of muscle region centroid against normalized slice location	Plot of x-coordinate of muscle region centroid against normalized slice location
<u>Mean</u>	<u>Mean</u>

(a)

Left Medial Pterygoid	Right Medial Pterygoid
Plot of y-coordinate of muscle region centroid against normalized slice location	Plot of y-coordinate of muscle region centroid against normalized slice location

(b)

Figure 5.10: Samples of (a) x-coordinate, (b) y-coordinate of centroid of muscle

region *vs* I_n for medial pterygoids.

The accuracies of the results for the left, right masseters, lateral pterygoids and medial pterygoids models when c is varied are summarized in Tables 5.1–5.3, respectively, and plotted in Figure 5.11.

The number of dominant slices c was varied from 5 to 10 for each of the 90 muscle models. In Figures 5.12, 5.14 and 5.16, examples on the orientations of the masseters, lateral pteygoids and medial pterygoids models are provided respectively, while in Figures 5.13, 5.15 and 5.17, sample models obtained for the masseters, lateral pteygoids and medial pterygoids respectively when c was varied, are displayed.

The average overlap indices (κ) achieved for the left, right masseters, lateral pterygoids and medial pterygoids, when 10 dominant slices are selected, are 91.5%, 91.4%, 90.7, 91.2%, 92.3% and 91.1%, respectively.

Table 5.1: Validation results for left and right masseters.

	Left Masseter						Right Masseter				
c	*Test Set*	*κ* (%)	*c*	*Test Set*	*κ* (%)	*c*	*Test Set*	*κ* (%)	*c*	*Test Set*	*κ* (%)
5	1	80.7	6	1	83.5	5	1	81.8	6	1	85.2
	2	81.2		2	84.0		2	80.9		2	84.3
	3	78.3		3	82.1		3	79.3		3	82.2
	4	81.7		4	83.9		4	82.1		4	85.5
	5	78.6		5	81.1		5	77.5		5	81.0
	6	81.7		6	84.8		6	82.3		6	85.4
	7	78.0		7	81.2		7	77.9		7	82.8
	8	80.8		8	82.5		8	80.5		8	83.8
	9	79.3		9	83.0		9	78.1		9	81.8
	10	79.8		10	82.3		10	80.4		10	84.9
	11	78.9		11	82.6		11	78.5		11	82.5
	12	80.3		12	83.3		12	79.7		12	83.1
	13	79.7		13	83.9		13	80.8		13	82.9
	14	78.5		14	83.5		14	79.2		14	83.8
	15	80.5		15	81.8		15	81.5		15	84.5
	Mean	**79.9**		*Mean*	**82.9**		*Mean*	**80.0**		*Mean*	**83.6**
7	1	86.8	8	1	89.8	7	1	87.8	8	1	91.2
	2	87.5		2	90.4		2	87.5		2	90.2
	3	86.3		3	89.2		3	85.8		3	88.9
	4	85.8		4	89.6		4	87.2		4	90.3
	5	85.3		5	90.3		5	87.9		5	90.3
	6	86.7		6	89.1		6	88.1		6	90.5
	7	85.2		7	88.9		7	86.1		7	89.6
	8	86.1		8	90.4		8	87.0		8	91.0
	9	85.9		9	87.6		9	85.8		9	88.9
	10	86.7		10	89.4		10	88.5		10	91.0
	11	87.1		11	89.2		11	87.1		11	89.3
	12	86.5		12	87.9		12	86.8		12	89.6
	13	85.9		13	88.9		13	87.8		13	89.1
	14	86.1		14	88.1		14	87.6		14	89.5
	15	85.5		15	88.5		15	88.1		15	89.7
	Mean	**86.2**		*Mean*	**89.2**		*Mean*	**87.3**		*Mean*	**89.9**
9	1	90.9	10	1	92.2	9	1	91.9	10	1	92.6
	2	91.2		2	92.0		2	91.6		2	91.8
	3	90.5		3	91.5		3	89.8		3	90.7
	4	90.8		4	91.8		4	91.3		4	92.0
	5	91.2		5	92.1		5	91.0		5	91.8
	6	89.9		6	91.7		6	91.0		6	91.9
	7	90.3		7	91.4		7	90.3		7	90.7
	8	91.4		8	92.9		8	91.5		8	92.0
	9	88.3		9	90.4		9	89.8		9	90.6
	10	90.2		10	91.2		10	91.7		10	92.2
	11	89.5		11	90.9		11	90.5		11	91.4
	12	89.3		12	91.3		12	90.3		12	90.6
	13	90.5		13	91.1		13	91.1		13	91.6
	14	91.1		14	91.6		14	90.1		14	90.4
	15	89.7		15	90.7		15	90.5		15	91.2
	Mean	**90.3**		*Mean*	**91.5**		*Mean*	**90.8**		*Mean*	**91.4**

Table 5.2: Validation results for left and right lateral pterygoids.

	Left Lateral Pterygoid						Right Lateral Pterygoid				
c	*Test Set*	κ (%)	c	*Test Set*	κ (%)	c	*Test Set*	κ (%)	c	*Test Set*	κ (%)
5	1	80.7	6	1	84.9	5	1	78.9	6	1	83.2
	2	80.0		2	83.6		2	79.2		2	83.8
	3	77.7		3	81.0		3	77.8		3	81.0
	4	78.6		4	83.5		4	79.4		4	82.4
	5	80.8		5	84.9		5	78.1		5	83.2
	6	80.7		6	84.2		6	77.5		6	81.3
	7	78.6		7	83.2		7	79.2		7	83.6
	8	80.6		8	84.8		8	80.2		8	84.0
	9	77.2		9	83.0		9	78.9		9	83.2
	10	78.4		10	82.3		10	79.1		10	84.4
	11	80.5		11	83.5		11	80.2		11	84.2
	12	78.2		12	82.4		12	79.4		12	81.2
	13	79.1		13	83.1		13	77.7		13	83.4
	14	80.3		14	83.5		14	78.6		14	82.2
	15	77.2		15	82.7		15	79.5		15	81.9
	Mean	**79.2**		*Mean*	**83.4**		*Mean*	**78.9**		*Mean*	**82.9**
7	1	89.4	8	1	90.4	7	1	89.7	8	1	90.9
	2	86.2		2	87.0		2	87.8		2	88.9
	3	86.6		3	87.7		3	86.8		3	87.4
	4	87.2		4	88.5		4	86.9		4	87.5
	5	86.7		5	89.8		5	87.2		5	90.4
	6	87.5		6	89.7		6	88.2		6	89.6
	7	87.8		7	89.0		7	86.6		7	87.4
	8	86.2		8	87.8		8	88.8		8	90.3
	9	88.8		9	90.0		9	88.4		9	89.5
	10	85.5		10	87.8		10	87.1		10	87.8
	11	86.1		11	88.5		11	87.3		11	87.8
	12	86.4		12	87.7		12	86.5		12	87.4
	13	85.9		13	87.9		13	86.4		13	88.4
	14	86.5		14	88.4		14	87.4		14	89.2
	15	87.4		15	88.9		15	87.7		15	88.1
	Mean	**87.0**		*Mean*	**88.6**		*Mean*	**87.5**		*Mean*	**88.7**
9	1	91.7	10	1	91.9	9	1	91.8	10	1	92.7
	2	88.1		2	89.7		2	90.7		2	92.0
	3	88.6		3	90.8		3	88.1		3	89.7
	4	89.1		4	91.4		4	89.2		4	90.6
	5	90.4		5	91.7		5	91.3		5	92.7
	6	91.0		6	91.3		6	90.9		6	92.7
	7	89.8		7	90.4		7	89.1		7	90.6
	8	88.1		8	89.1		8	91.3		8	92.6
	9	90.4		9	91.5		9	90.9		9	92.2
	10	88.8		10	90.3		10	88.9		10	90.4
	11	89.1		11	90.3		11	88.4		11	89.8
	12	88.6		12	89.8		12	88.3		12	90.5
	13	90.2		13	90.8		13	89.2		13	91.3
	14	89.9		14	90.5		14	89.4		14	90.7
	15	89.7		15	91.4		15	88.6		15	89.1
	Mean	**89.6**		*Mean*	**90.7**		*Mean*	**89.7**		*Mean*	**91.2**

Table 5.3: Validation results for left and right medial pterygoids.

	Left Medial Pterygoid						Right Medial Pterygoid				
c	Test Set	κ (%)	c	Test Set	κ (%)	c	Test Set	κ (%)	c	Test Set	κ (%)
5	1	81.4	6	1	84.5	5	1	81.4	6	1	84.1
	2	78.2		2	84.9		2	80.3		2	85.0
	3	78.6		3	82.4		3	79.5		3	84.2
	4	78.5		4	82.0		4	80.8		4	83.5
	5	81.0		5	84.1		5	80.2		5	83.8
	6	80.4		6	82.1		6	79.8		6	84.9
	7	78.0		7	83.5		7	80.8		7	85.1
	8	77.5		8	83.7		8	80.5		8	84.7
	9	81.1		9	85.0		9	81.2		9	84.5
	10	78.3		10	82.8		10	81.8		10	85.3
	11	78.6		11	82.1		11	79.8		11	83.8
	12	79.2		12	83.4		12	81.2		12	84.5
	13	80.1		13	84.2		13	79.4		13	83.5
	14	78.4		14	83.8		14	79.6		14	84.1
	15	79.6		15	84.1		15	80.5		15	84.6
	Mean	**79.3**		*Mean*	**83.5**		*Mean*	**80.5**		*Mean*	**84.4**
7	1	85.4	8	1	88.8	7	1	86.5	8	1	88.2
	2	87.5		2	89.7		2	87.1		2	89.7
	3	86.3		3	90.4		3	87.0		3	87.9
	4	87.1		4	89.1		4	85.7		4	88.5
	5	86.7		5	90.5		5	86.7		5	88.2
	6	85.4		6	88.6		6	87.6		6	88.4
	7	86.1		7	89.3		7	88.1		7	90.5
	8	87.7		8	91.2		8	87.7		8	89.7
	9	86.8		9	90.2		9	86.2		9	88.3
	10	85.8		10	90.9		10	88.9		10	89.3
	11	86.4		11	88.1		11	85.6		11	88.4
	12	87.1		12	89.7		12	86.4		12	89.1
	13	86.8		13	89.8		13	87.2		13	89.5
	14	87.2		14	90.5		14	86.8		14	89.2
	15	85.8		15	89.5		15	87.3		15	90.2
	Mean	**86.5**		*Mean*	**89.8**		*Mean*	**87.0**		*Mean*	**89.0**
9	1	90.8	10	1	91.8	9	1	91.0	10	1	92.4
	2	91.4		2	92.2		2	89.8		2	91.1
	3	90.7		3	91.0		3	88.5		3	89.8
	4	91.5		4	92.3		4	90.8		4	91.7
	5	90.8		5	92.7		5	91.5		5	92.4
	6	89.8		6	91.9		6	88.6		6	89.1
	7	91.5		7	93.5		7	91.2		7	91.7
	8	91.9		8	93.4		8	89.9		8	90.5
	9	91.4		9	93.0		9	90.5		9	90.9
	10	91.3		10	92.1		10	89.5		10	91.0
	11	90.5		11	91.2		11	89.2		11	90.9
	12	91.2		12	92.4		12	90.4		12	91.3
	13	91.5		13	93.1		13	91.0		13	92.1
	14	90.9		14	92.2		14	89.4		14	90.5
	15	89.7		15	91.8		15	90.8		15	91.6
	Mean	**91.0**		*Mean*	**92.3**		*Mean*	**90.1**		*Mean*	**91.1**
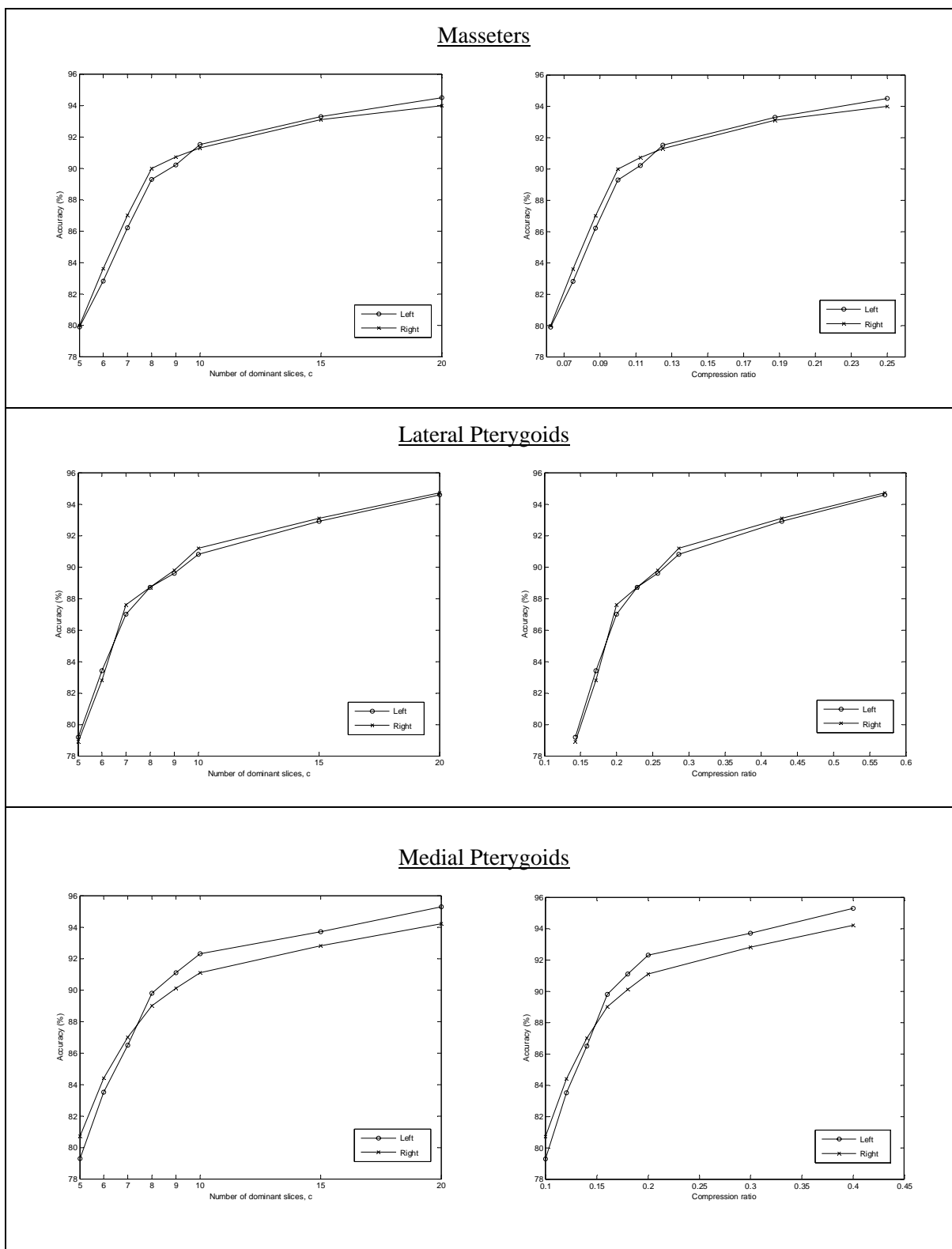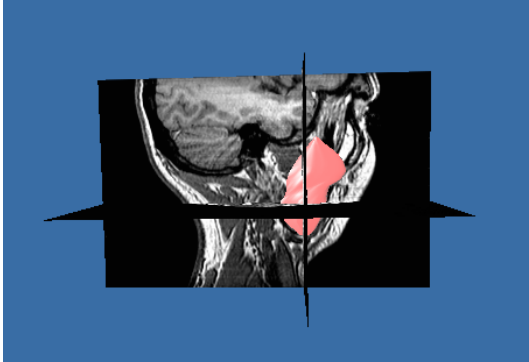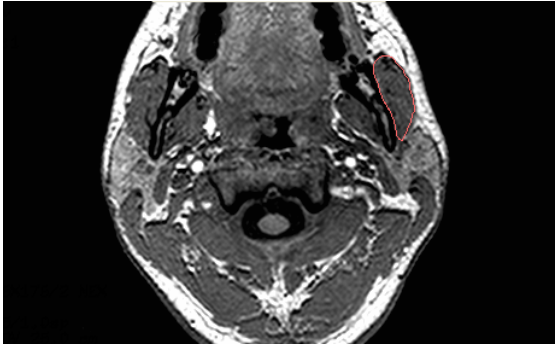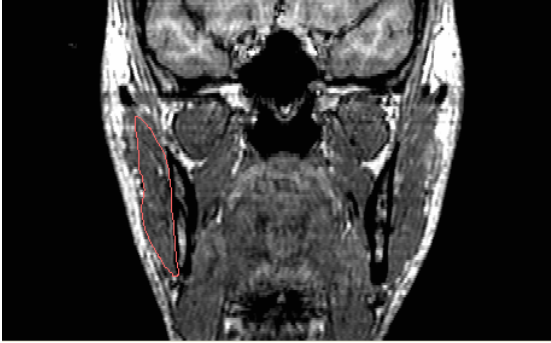
Figure 5.11: Plot of models' accuracies against number of dominant slices and compression ratio.

Right Masseter	
3D View	Axial View
Coronal View	Sagittal View

(a)

Left Masseter	
3D View	Axial View
Coronal View	Sagittal View

(b)

Figure 5.12: Orientations of the (a) right and (b) left masseters models.
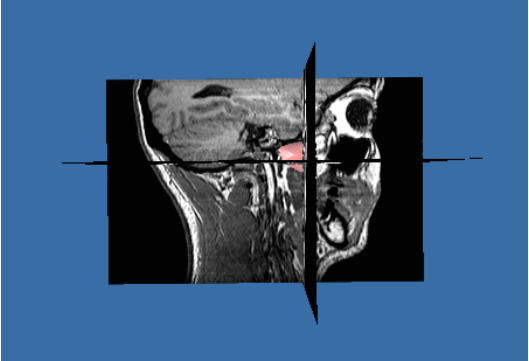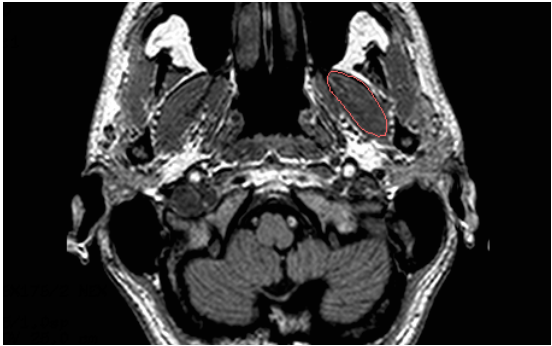
Left Masseter		Right Masseter	
$c = 5$	$c = 6$	$c = 5$	$c = 6$
$c = 7$	$c = 8$	$c = 7$	$c = 8$
$c = 9$	$c = 10$	$c = 9$	$c = 10$

Figure 5.13: Left and right masseters models. c is the number of dominant slices used.

Right Lateral Pterygoid	
3D View	Axial View
Coronal View	Sagittal View

(a)

Left Lateral Pterygoid	
3D View	Axial View
Coronal View	Sagittal View

(b)

Figure 5.14: Orientations of the (a) right and (b) left lateral pterygoids models.
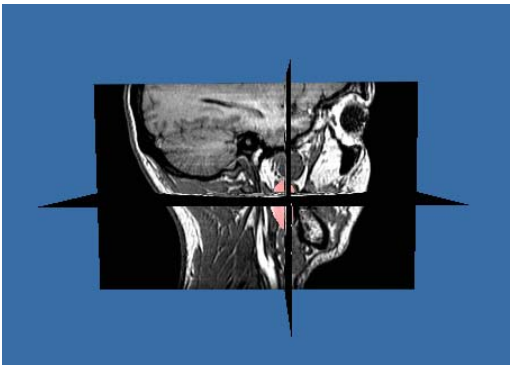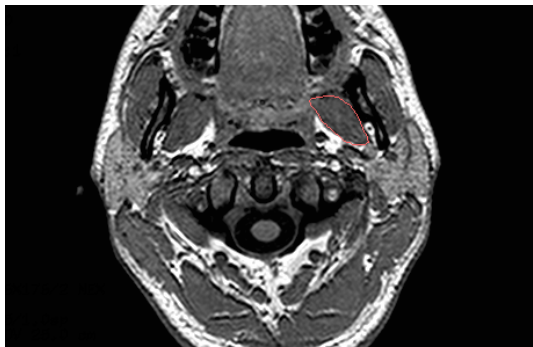
Left Lateral Pterygoid		Right Lateral Pterygoid	
$c = 5$	$c = 6$	$c = 5$	$c = 6$
$c = 7$	$c = 8$	$c = 7$	$c = 8$
$c = 9$	$c = 10$	$c = 9$	$c = 10$

Figure 5.15: Left and right lateral pterygoids models.

Right Medial Pterygoid	
3D View	Axial View
Coronal View	Sagittal View

(a)

Left Medial Pterygoid	
3D View	Axial View
Coronal View	Sagittal View

(b)

Figure 5.16: Orientations of the (a) right and (b) left medial pterygoids models.

Left Medial Pterygoid		Right Medial Pterygoid	
$c = 5$	$c = 6$	$c = 5$	$c = 6$
$c = 7$	$c = 8$	$c = 7$	$c = 8$
$c = 9$	$c = 10$	$c = 9$	$c = 10$
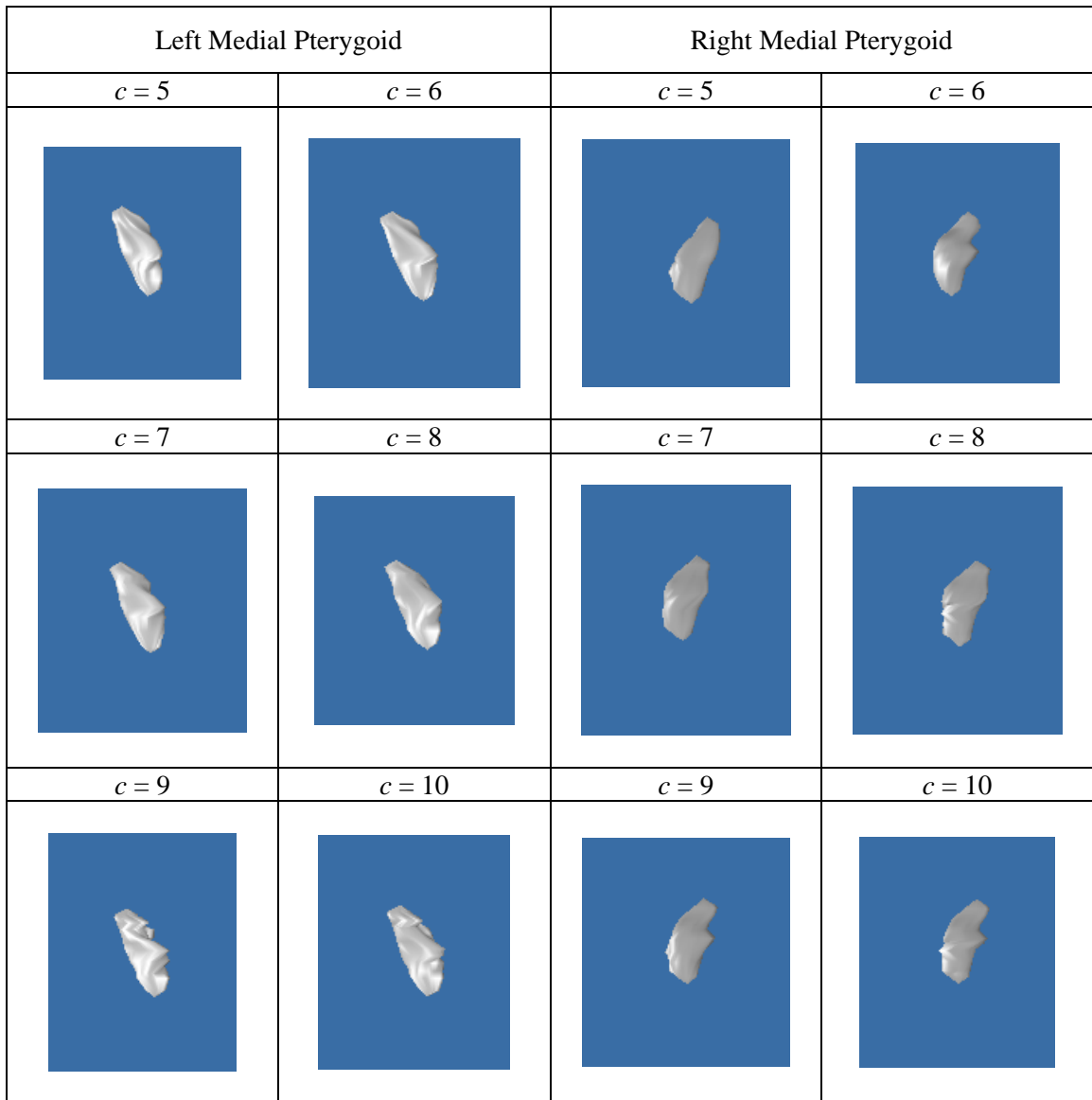
Figure 5.17: Left and right medial pterygoids models.

5.6 Discussion

5.6.1 Sensitivity of model accuracy to number of dominant slices, *c*

It can be observed in Figure 5.11 that the accuracy of the constructed models improves as the number of dominant slices is increased. When only five dominant slices are used, accuracy is about 80% or less; with 10 dominant slices, it is above 90%. It can

also be observed in Figure 5.11 that the rate of increase in accuracy levels off as the number of dominant slices increases. For example, referring to the accuracy for the right masseter in Table 5.1, the increase was 3.6% when the number of dominant slices was raised from 5 to 6, but only 1.5% when the number of dominant slices was increased from 8 to 10. The use of 8 dominant slices will produce muscle models with nearly 90% accuracy, and compared to the use of 10 dominant slices, the difference in accuracy is approximately 2%. This trend is continued when more than 10 dominant slices are utilized.

Besides displaying the variation of accuracy against number of dominant slices used (c), Figure 5.11 also shows the variation of accuracy against compression ratio (η). To obtain accuracy above 90%, a higher η ($\frac{10}{35} = 0.286$) is required for the lateral pterygoid compared to the masseter ($\frac{10}{80} = 0.125$). This is accounted for by the greater complexity of the structure of the former (Figure 5.15) compared to that of the latter (Figure 5.13).

5.6.2 Selection of I_i and I_f

Currently the selection of slices I_i and I_f, where the muscle first and last appears, respectively, is done manually by the radiologist. The accurate selection of these two slices is hindered by the presence of fuzzy boundaries between the muscles and surrounding soft tissue. Manual selection might also introduce intra- and inter-observer variations. Fortunately, these factors do not have a significant impact in the case of our MR datasets, which have 1mm slices. The masseter muscle occupies about 80 slices,

and hence a variation of two slices will only cause a deviation of 2.5%. For the lateral and medial pterygoid muscles, which occupy about 35 and 50 slices, respectively, a variation of two slices will result in a deviation of 5.7% and 4.0%, respectively.

Using eight dominant slices, we carried out a sensitivity test to investigate the effect that selection of I_i and I_f has on model accuracy. We denote the original I_i and I_f that we have selected for our models by I_i^o and I_f^o, respectively. We considered four scenarios: (i) $I_i^o +2$ slices and $I_f^o +2$ slices; (ii) $I_i^o +2$ slices and $I_f^o -2$ slices ; (iii) $I_i^o -2$ slices and $I_f^o +2$ slices; (iv) $I_i^o -2$ slices and $I_f^o -2$ slices. Through this test, we conclude that slight variations of ± 2 slices in the selection of I_i and I_f have little impact on the accuracies of the built models with the difference being less than 2% when compared to the models built using I_i^o and I_f^o.

5.6.3 Number of polynomial coefficients used in spline fitting

It is mentioned in Section 5.3.2 that 10 polynomial coefficients are used in the spline-fitting function. This is because it has been observed, in this particular application here, that a smaller number of polynomial coefficients, such as 5, may result in over-smoothing of the spline, higher approximation error and overlooking of the dominant slices. On the other hand, a large number of polynomial coefficients, such as 15, will result in over-fitting and the inclusion of less salient dominant slices. This is illustrated in Figure 5.18.

10 coefficients

(a)

5 coefficients => over-smoothing

(b)

15 coefficients => over-fitting
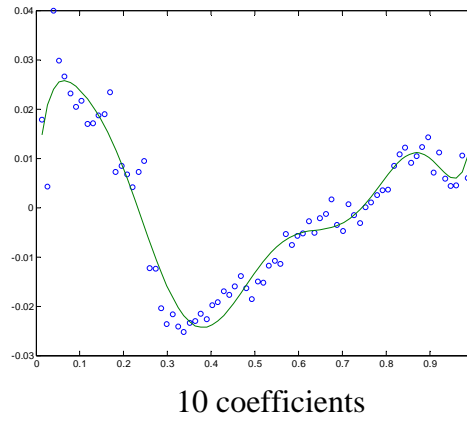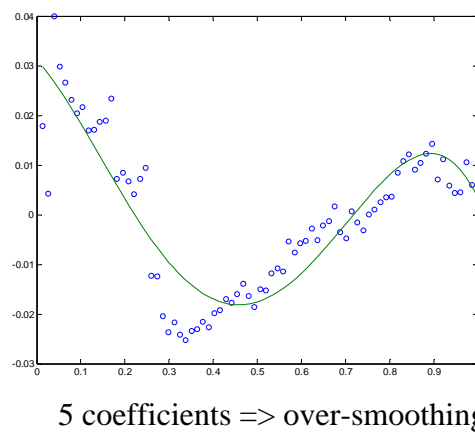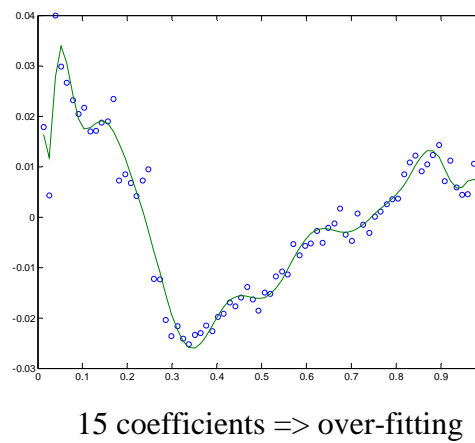
(c)

Figure 5.18: Spline-fitting when (a) 10 polynomial coefficients are used,

(b) 5 polynomial coefficients are used,

(c) 15 polynomial coefficients are used.

5.6.4 Segmentation of muscles from dominant slices in study datasets

Segmentation of the muscles has to be carried out on the dominant slices. Other than MR slices I_i and I_f, where an experienced clinician will be better able to differentiate between muscle and surrounding tissue, the techniques proposed in the previous chapter can be applied to segment the muscles from the dominant slices. Other alternatives for 2D segmentation on the dominant slices will include manual contour tracing or the live-wire method [88].

5.6.5 Comparison with models from slices selected at equal intervals

We selected eight dominant slices at regular intervals for each of the masticatory muscles. For example, if the masseter occupies 78 slices, the dominant slices, where 2D segmentation is carried out, would be slices 1, 12, 23, 34, 45, 56, 67 and 78. The mean κ values obtained using this method were 84.2%, 77.6% and 81.2% for the masseter, lateral and medial pterygoids, respectively. Using eight dominant slices, κ values obtained were 89.6%, 88.7% and 89.4%, respectively. The difference in accuracy is the largest for the lateral pterygoid (difference of 11.1%) and the smallest for the masseter (difference of 5.4%). This is because the structure of the lateral pterygoid (Figure 5.15) is more complex compared to the masseter (Figure 5.13). By selecting dominant slices at equal intervals, and not using our proposed method, one will fail to capture the slices which best represent the features (shape and size) of the lateral pterygoid and hence a model with lower accuracy would be constructed.

5.6.6 Clustering of candidates for dominant slices

As mentioned in Section 5.3.3, FCM clustering is performed on the candidates for dominant slices to obtain c classes, with the cluster centers taken to be the locations of the dominant slices. Although the slices at the turning points in the plots of cross-sectional muscle area vs I_n were selected as candidates for dominant slices, the dominant slices that are finally determined in the test set may not contain them, due to the clustering process. Comparing the left masseter models when $c = 8$, 9 and 10 in Figure 5.13, it can be observed that when $c = 9$, the dominant slices do not consist of one of the slices at the turning points. A slice near it is determined instead. Even then, the overall accuracy of the built model is not greatly affected and this is an encouraging sign.

5.6.7 Potential application to other structures

Using the proposed method, the dominant slices were determined for the masseter, lateral and medial pterygoids, and accurate muscle models were built. The masseter, lateral and medial pterygoids are anatomies of different shapes and sizes, and the fact that accurate models of them can be built using the proposed method is an indication that it is applicable to other anatomies with different shapes and sizes.

Chapter 6

Segmentation of the masticatory muscles from volumetric data

6.1   Introduction

The lack of a computerized method for the segmentation of human masticatory muscles is most probably due to the fact that they lacks strong edges in MR images and they have fairly similar intensity values with their surrounding soft tissue. This situation is more severe in some MR slices than others. We propose a model-based solution to segment the masticatory muscles from MR datasets.

There is an increasing use of model-based techniques for segmentation in MR images, such as the work described in [89], which incorporates prior knowledge for segmenting the corpus callosum from MR images with little human intervention. Another example is found in [30], where segmentation is carried out via matching of distributions belonging to photometric variables that incorporate learned shape and appearance models for the objects of interest. Other examples of model-based methods used in medical image segmentation can be found in [90, 91].

In the previous chapter, an approach was presented to determine the dominant slices for the masticatory muscles and accurate patient-specific masticatory muscles models were built. These models provide useful information especially in the regions where there are fuzzy boundaries between the muscles and surrounding soft tissue.

In the proposed method presented in this chapter, the patient-specific models serves as initial coarse segmentations which are further refined by first matching the distributions of the intensity values belonging to the pixels within the patient-specific models to their expected distributions which were estimated from the distributions of the pixels within the segmented muscle regions in the dominant slices. The boundaries of the output results are then expanded and boundary analysis performed on it. In this process, boundary pixels whose intensity values fall outside the standard deviation range, which was obtained from the boundaries of the segmented muscle regions in the dominant slices, are removed, thus providing the final segmentations.

6.2   Overview of proposed work

The overview of the proposed method is in Figure 6.1. Given a test MR dataset, patient-specific muscles models are first built using the process described in Chapter 5. These models serve as the coarse segmentations. Two refinements are then carried out on the coarse segmentations to arrive at the final segmentations. In the first refinement, the distributions of the pixels' intensity values in the muscles' regions belonging to the muscles models are matched to their expected distributions, which are obtained from the muscles regions in the dominant slices. The boundaries of the output results are then expanded and boundary analyses are performed on them. In this iterative process, boundary pixels whose intensity values fall outside the threshold are removed. The threshold is set to be the intensity standard deviation of the pixels belonging to the boundaries of the segmented muscles regions in the dominant slices.

```
┌─────────────────────────────────────┐
│     Patient-specific muscles models  │
└─────────────────────────────────────┘
                  ⬇
┌─────────────────────────────────────┐
│   Matching distributions of pixels in│
│       MR slices of muscles models    │
└─────────────────────────────────────┘
                  ⬇
┌─────────────────────────────────────┐
│    Analysis on boundary pixels and   │
│        removal of outliers           │
└─────────────────────────────────────┘
```
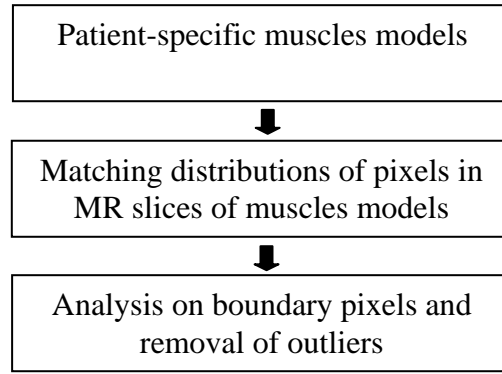
Figure 6.1: Overview of proposed method.

6.3 The proposed method

6.3.1 Matching distributions in MR slices

The patient-specific muscles models obtained using the approach proposed in the previous chapter serve as coarse segmentation of the masticatory muscles. An initial refinement is performed by matching the distributions of the intensity values belonging to the pixels in the muscles regions belonging to the slices within the muscles models to their expected distributions which we estimated from the distributions of the pixels within the segmented muscles regions in the dominant slices. The rationale behind this is that there is relatively uniform distribution of the intensity values within the muscle structure.

Let the slices which the muscle occupy in the MR test dataset be $S = \{S_1, S_2, S_3, ..., S_N\}$, where S_i denotes the ith slice and N the total number of slices that the muscle occupies in the MR test dataset. The intensity value at point (x, y) is defined as $I(x, y)$ and R_i as the muscle region bounded by the patient-specific muscle model in slice S_i. By

letting N_i be the number of pixels in R_i, the mean and standard deviation intensity of each region R_i are denoted by:

$$M_{R_i} = \frac{1}{N_i} \sum_{(x,y) \in R_i} I(x, y) \qquad (6.1)$$

and

$$SD_{R_i} = \sqrt{\frac{1}{N_i} \sum_{(x,y) \in R_i} \left(I(x, y) - M_{R_i} \right)^2} \qquad (6.2)$$

respectively.

Through the distributions of the pixels' intensity values lying within the segmented muscle regions in the dominant slices, the distributions $\left(M_{R_i}^{est}, SD_{R_i}^{est} \right)$ of the regions in the slices lying between the dominant slices are estimated. For a slice S_i which lies between dominant slices S_j and S_k where $j < k$,

$$M_{R_i}^{est} = M_{R_j} + (i - j) \left(\frac{M_{R_k} - M_{R_j}}{k - j} \right) \qquad (6.3)$$

$$SD_{R_i}^{est} = SD_{R_j} + (i - j) \left(\frac{SD_{R_k} - SD_{R_j}}{k - j} \right) \qquad (6.4)$$

The muscle regions in the dominant slices of the coarse segmentation built from a test dataset are assumed to be reasonably accurate, as they can be either manually segmented or segmented accurately using our proposed 2D techniques which have been validated, and hence no refinement is performed on them. As for the slices lying in between the dominant slices, there might be some inaccuracies with the muscle regions delineated by the coarse segmentation and this can be improved. An initial refinement process is carried out for the muscle region in each slice:

- Shift the centroid to one of its 8-connected neighbours (Figure 6.2).
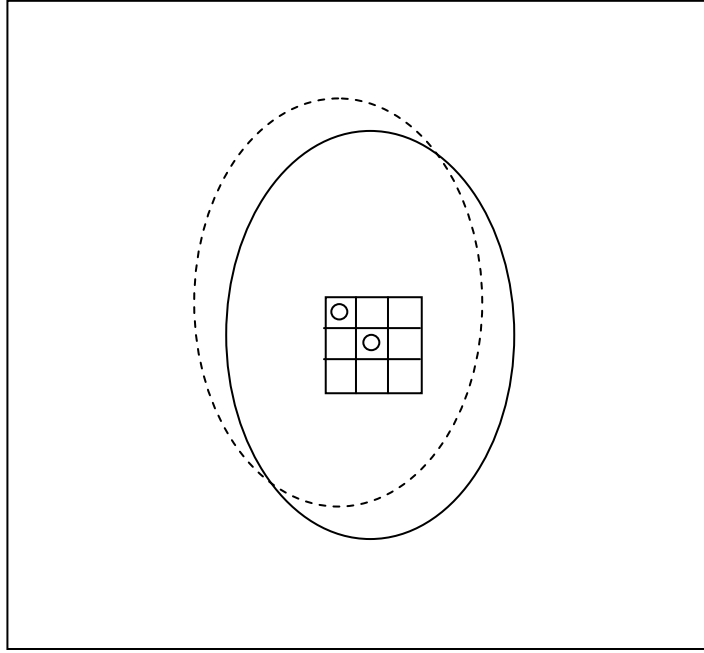
Figure 6.2: Shifting of the centroid and its corresponding muscle region.

- Calculate the intensity mean $\left(M'_{R_i}\right)$ and standard deviation $\left(SD'_{R_i}\right)$ of the corresponding muscle region.

- Repeat the above two steps for the other 8-connected neighbours.

- Out of the 9 possible regions (inclusive of the original region), select the muscle region which has the minimum combined difference between its distribution and the estimated distribution i.e. minimize the following criterion:

$$T_R = \left(\left|\left(M'_{R_i} - M^{est}_{R_i}\right)\right| + \left|\left(SD'_{R_i} - SD^{est}_{R_i}\right)\right|\right) \qquad (6.5)$$

6.3.2 Boundary analysis

Having selected the muscle regions whose distributions best matches the estimated distributions, 3D boundary analysis is carried out on the resulting muscle structure after the first refinement. Before this analysis is carried out, the boundary of the resulting muscle structure is first expanded by 2 pixels (Figure 6.3).
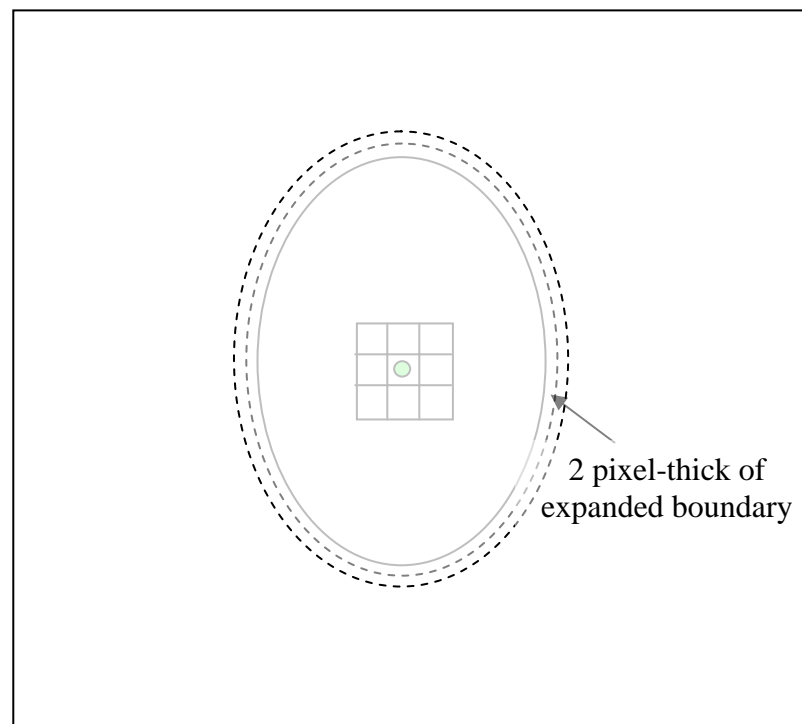
Figure 6.3: 2D view of a muscle region in a MR slice after expanding the boundary.

The rationale behind expanding the boundary is that the initial boundary might have omitted some of the pixels which should be included. Expanding the boundary will include some of the pixels which were previously left out. However, expanding the boundary also meant the inclusion of some pixels which should not be included. This problem is minimized by removing boundary pixels whose intensity values fall outside the standard deviation range derived from the pixels on the muscles' boundaries in the

dominant slices. Pixels whose intensity values fall outside the standard deviation range are classified as outliers. The rationale behind this is that in our application here, the boundary pixels belonging to a single anatomy have intensity values that do not have a wide standard deviation. The pixels with relatively higher intensity values and relatively lower intensity values probably belong to surrounding bright tissue and bone tissue respectively.

We calculate the intensity standard deviation $\left(SD_B^{ref}\right)$ of the boundaries belonging to the segmented muscle regions in the dominant slices of the test dataset. This is set as a threshold and the refinement process is carried out as follows:

- Obtain the boundary of the 3D muscle.

- Calculate the mean $\left(M_B\right)$ and standard deviation $\left(SD_B\right)$ of the boundary pixels.

- If $SD_B > SD_B^{ref}$, remove those boundary pixels with intensity values smaller than $M_B - SD_B^{ref}$ or greater than $M_B + SD_B^{ref}$.

- Repeat the above 3 steps on the resulting 3D muscle.

- Stop iterations when $SD_B < SD_B^{ref}$.

6.4   Experiments

Using the locations of the dominant slices which were determined in the previous chapters, patient-specific muscles models were built using test datasets from fifteen

adult volunteers. Six dominant slices are used here. These models serve as coarse segmentations and the proposed approach presented here is applied to refine them.

A total of 90 human masticatory muscles (left and right masseters, lateral and medial pterygoids) belonging to fifteen subjects were segmented. The κ index [74] introduced earlier was used to evaluate the consistency between the computerized segmentations and manual segmentations. In addition, quantification was carried out by measuring the volumes of the muscles segmentations.

Other experiments include varying the number of available options for the selection of centroid candidates and varying the boundary thickness after the initial refinement.

6.5   Results

The accuracies for the segmentations of the masseters, lateral pterygoids and medial pterygoids are tabulated in Tables 6.1 – 6.3 respectively. The average κ indices achieved for the left and right masseters, lateral pterygoids and medial pterygoids are 86.6%, 87.5%, 86.5%, 86.3%, 86.9% and 87.1% respectively. Examples of the segmentations for the left and right masseters, lateral pterygoids and medial pterygoids can be found in Figures 6.4 – 6.6 respectively while examples of the volume rendered human head together with the human masticatory muscles is in Figure 6.7. The muscles segmentations displayed in Figures 6.4 – 6.6 follow the positional array shown in Figures 5.12, 5.14 and 5.16 respectively.

Table 6.1: Validation results for left and right masseters segmentations.

Left Masseter		Right Masseter	
Test Set	*Overlap index κ (%)*	*Test Set*	*Overlap index κ (%)*
1	86.2	1	88.5
2	87.9	2	87.1
3	85.3	3	86.5
4	86.6	4	89.1
5	87.0	5	86.3
6	88.5	6	88.1
7	85.0	7	87.5
8	85.9	8	87.8
9	85.5	9	84.2
10	85.4	10	87
11	87.8	11	88.1
12	85.5	12	87.3
13	86.5	13	86.0
14	88.1	14	89.5
15	87.8	15	89.5
Mean	**86.6**	*Mean*	**87.5**
Standard deviation	**1.18**	*Standard deviation*	**1.42**

Table 6.2: Validation results for left and right lateral pterygoids segmentations.

Left Lateral Pterygoid		Right Lateral Pterygoid	
Test Set	*Overlap index κ (%)*	*Test Set*	*Overlap index κ (%)*
1	86.0	1	87.9
2	88.4	2	86.8
3	84.7	3	84.7
4	86.9	4	84.6
5	87.9	5	87.1
6	87.0	6	86.5
7	85.1	7	87.4
8	87.9	8	88.0
9	88.0	9	85.6
10	86.2	10	88.1
11	87.4	11	86.7
12	84.6	12	86.1
13	85.0	13	83.7
14	86.4	14	86.9
15	85.2	15	83.6
Mean	**86.5**	*Mean*	**86.3**
Standard deviation	**1.31**	*Standard deviation*	**1.50**

Table 6.3: Validation results for left and right medial pterygoids segmentations.

Left Medial Pterygoid		Right Medial Pterygoid	
Test Set	*Overlap index* κ *(%)*	*Test Set*	*Overlap index* κ *(%)*
1	85.6	1	85.3
2	85.2	2	87.1
3	88.4	3	86.0
4	84.0	4	88.1
5	88.4	5	86.0
6	88.5	6	86.7
7	89.1	7	89.9
8	88.5	8	85.8
9	86.0	9	85.2
10	85.9	10	88.5
11	84.1	11	89.8
12	87.3	12	86.1
13	85.2	13	86.2
14	89.1	14	86.6
15	87.8	15	89.5
Mean	**86.9**	*Mean*	**87.1**
Standard deviation	**2.01**	*Standard deviation*	**1.63**

Left Masseter	Right Masseter
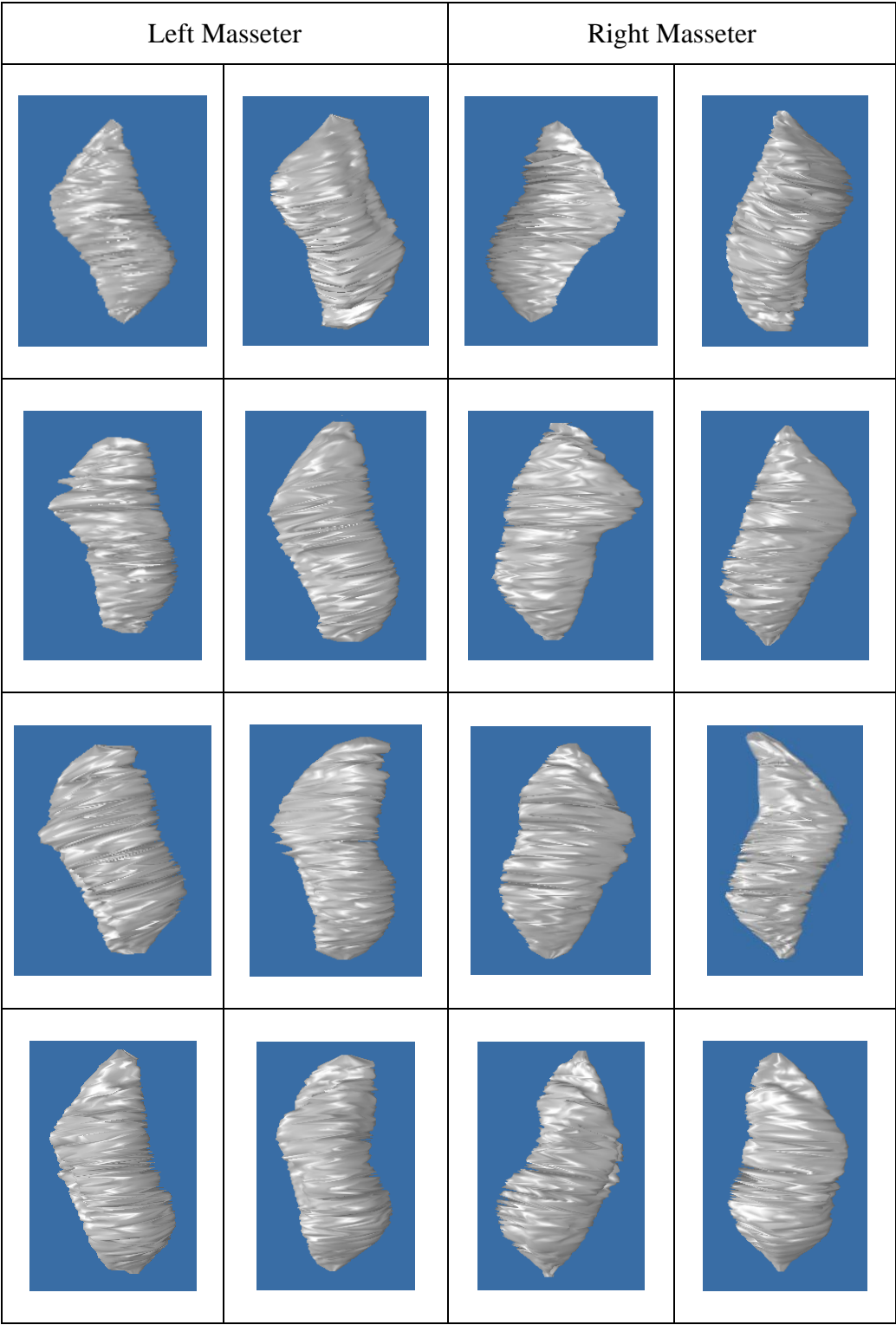
Figure 6.4: 3D segmentations of left and right masseters.

Left Lateral Pterygoid		Right Lateral Pterygoid	
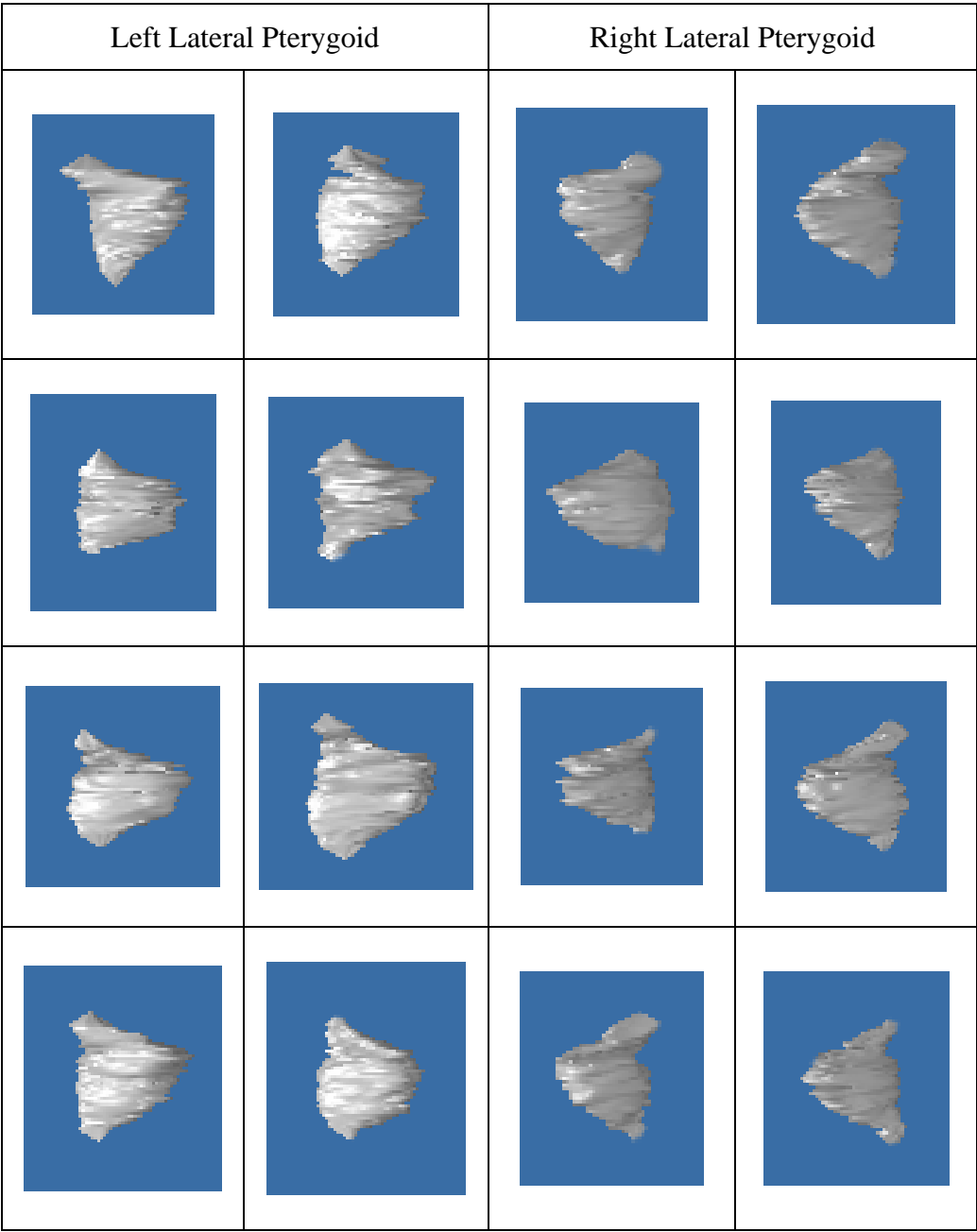
Figure 6.5: 3D segmentations of left and right lateral pterygoids.

Left Medial Pterygoid		Right Medial Pterygoid	
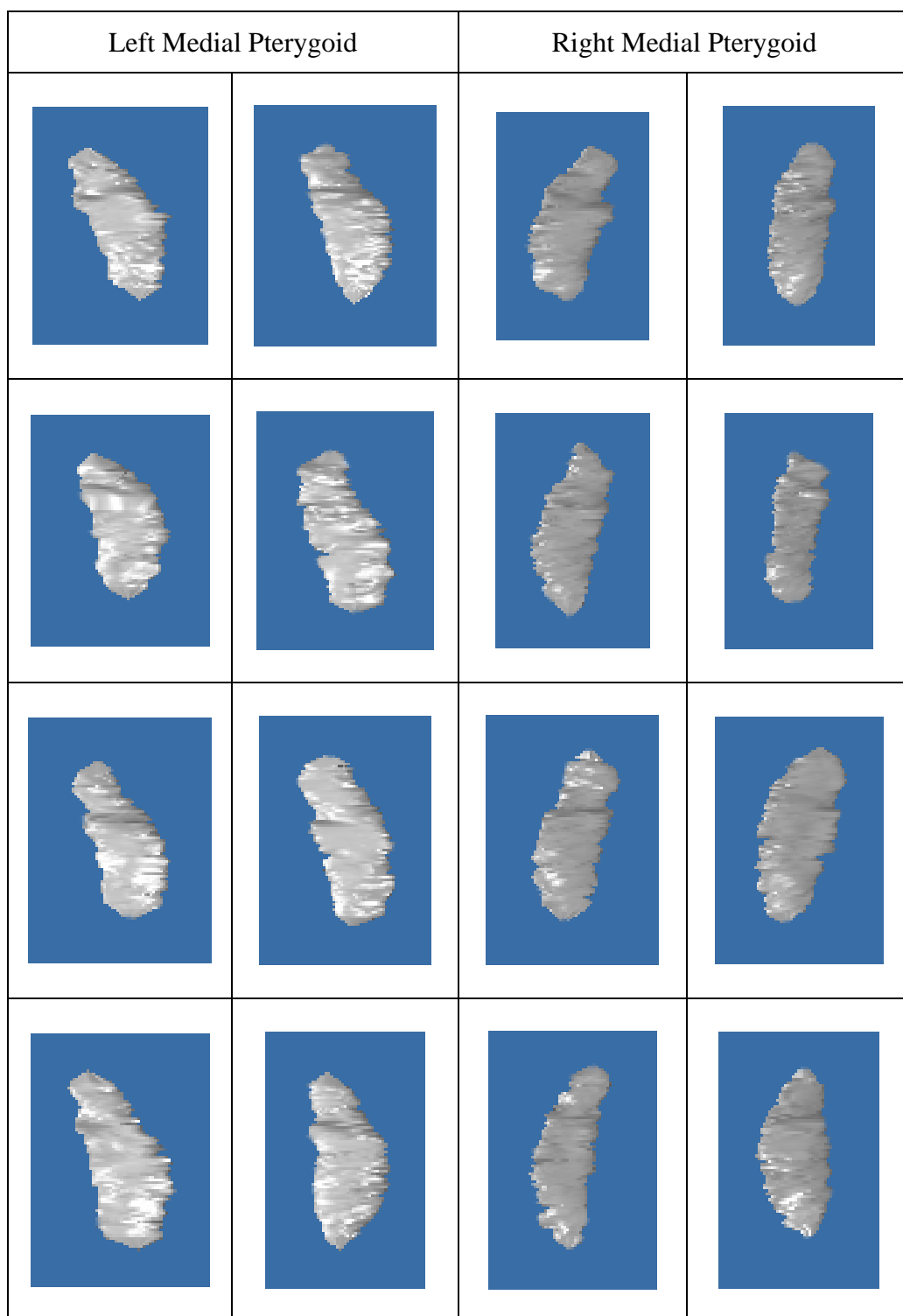
Figure 6.6: 3D segmentations of left and right medial pterygoids.
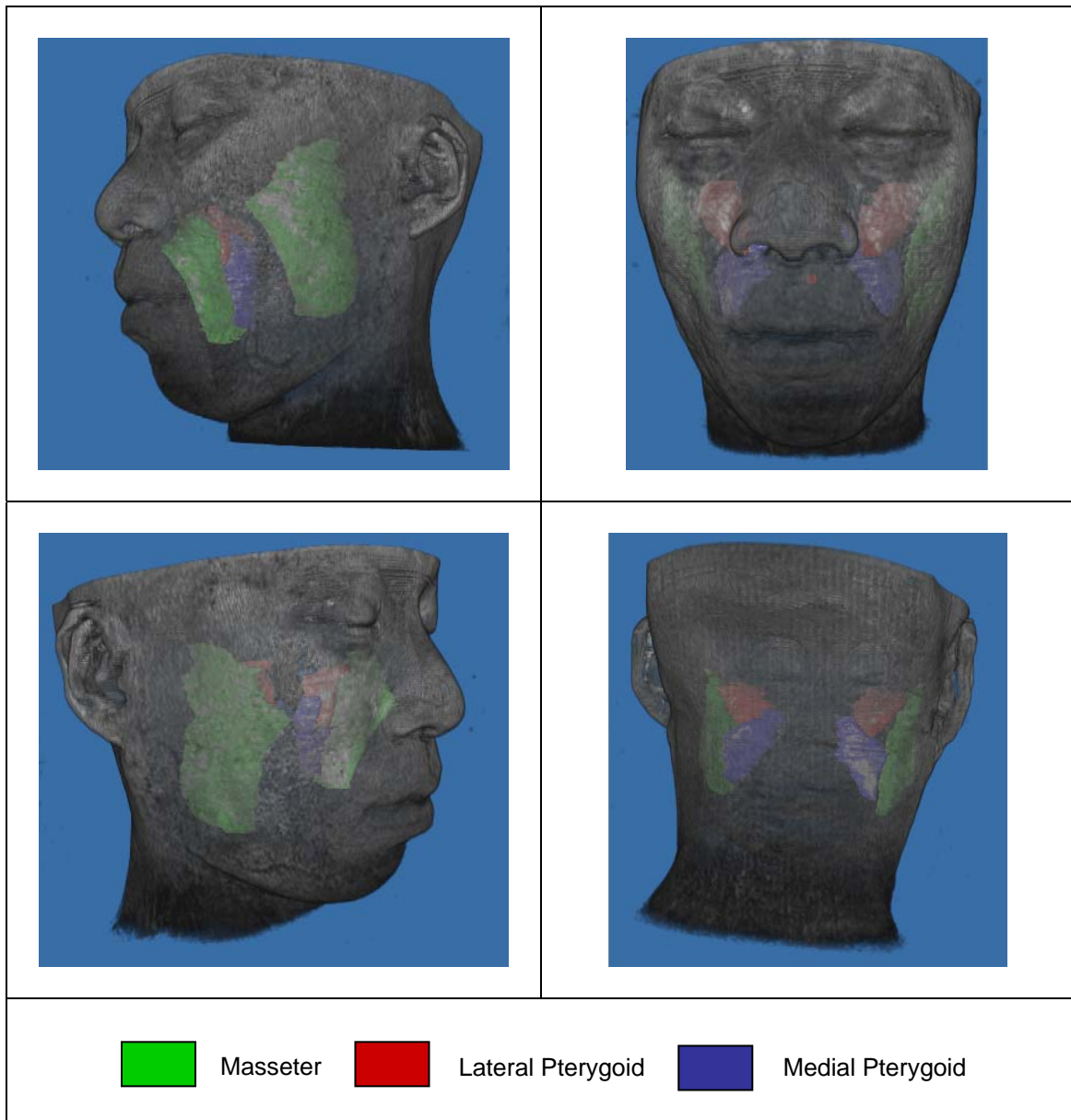
Figure 6.7: Volume rendered images of the human head with masticatory muscles.

6.6   Discussion

6.6.1 Accuracy of the muscles segmentations

The patient-specific model plays an important role in our proposed method as it serves

as an initial coarse segmentation. Comparisons are made between the accuracies of the

patient-specific models and the segmentations obtained in this chapter. In the previous chapter, it was reported that the average κ indices achieved for the left and right patient-specific masseters, lateral and medial pterygoids models are 82.9%, 83.6%, 83.4%, 82.9%, 83.5% and 84.4% respectively when six dominant slices were being used.

Empirical results indicate that on average, the left and right masseters, lateral and medial pterygoids segmentations obtained here have improvements in accuracies of 3.7%, 3.9%, 3.1%, 3.4%, 3.4% and 2.7% respectively over the models which were used as coarse segmentations. It should be stressed here even that though a significant improvement cannot always be guaranteed, there is always a positive improvement in the accuracy over that of the patient-specific models. Comparing the results in Figures 6.4 – 6.6 against those in Figures 5.13, 5.15 and 5.17, it can however be observed that the segmentation results have coarser surfaces as compared to the patient-specific models. This is due to the removal of outlier pixels on the boundary, which resulted in uneven boundaries.

The number of dominant slices used in our work here is six and 2D segmentations are carried out on only these six slices, which is only a small fraction of the MR slices which the muscles typically occupy and hence the amount of work clinicians need to do is minimized, which is the motivation for proposing this approach. It should be noted that increasing the number of dominant slices may help to improve on the accuracy of the model but this will result in a greater amount of human interaction and time consumption which makes it unfavourable.

6.6.2 On selection of centroid candidates

It was mentioned in Section 6.3.1 that the centroid of the muscle region in each MR slice was shifted from its original position to its 8-connected neighbours and checked for the agreement between the distributions of the corresponding regions and the estimated distribution which was derived from the masseter regions in the dominant slices. The region which has the best matched distribution is selected.

The candidates for the centroid were restricted to the 8-connected neighbours to preserve the shape of the patient-specific models. Further experiments were conducted to expand the list of candidates for centroid such that it includes the 16 pixels surrounding the 8-connected neighbours. It was observed that the final selected position of the centroid is usually among the original centroid and its 8-connected neighbours. Hence it is recommended that the candidates for the centroid be restricted to the 8-connected neighbours to reduce the amount of time consumed in the shifting and checking process.

6.6.3 On expansion of the boundaries after initial refinement

It was mentioned in Section 6.3.2 that the boundary of the coarse segmentation was expanded by 2 pixels before boundary analysis was carried out on it. By doing so, it is hoped that those pixels in the muscles regions which have been omitted by the coarse segmentations are included. The main reason for restricting the expansion to 2 pixels is that in a number of the MR slices, especially those in the region where the masseter first and last appears, the muscle and tissue have very similar intensity values and the inclusion of such pixels should be minimized.

It should be also noted here that in the boundary analysis process carried out under the proposed approach, not only the pixels in the expanded boundaries are being considered. At each iteration, the standard deviation of the intensities of the boundary pixels is being calculated and pixels classified as outliers are removed. The iterations stop only when the intensity standard deviation is smaller than the threshold which is set to be the standard deviation of the intensities of the boundary pixels of the segmented muscles regions in the dominant slices.

6.6.4 Quantification of segmentation results and clinical findings

The volumes of the 3D muscles segmentations were measured and tabulated in Tables 6.4 – 6.6. The mean volumes of the left and right masseters are $26.23cm^3$ and $25.53cm^3$ respectively. As the MR datasets used were acquired from healthy male adult subjects who have no facial problems, the left and right masseters' volumes of each subject are relatively similar. However, as the subjects have a wide age range, it can be observed that the standard deviations are relatively large at $3.95cm^3$ and $4.26cm^3$ for the left and right masseters respectively.

The mean volumes of the left and right lateral and medial pterygoids are $8.53\pm0.473cm^3$, $8.85\pm0.582cm^3$, $9.54\pm0.631cm^3$ and $9.76\pm0.859cm^3$ respectively.

The measurements were further classified according to the age and ethnic group of the subjects. For Asians who are left than 30 years old, the mean left and right masseter volumes are $28.54cm^3$ and $27.72cm^3$ respectively while for Asians more than 40 years old, the mean left and right masseter volumes are $23.16cm^3$ and $22.13cm^3$ respectively.

These findings are in line with what was previously reported in a study [15] where the muscles were manually segmented and which mentioned that the masseter muscle volume in young adults ($31.77 \pm 8.99\text{cm}^3$) is higher than that of older adults ($21.22 \pm 6.16\text{cm}^3$). This is an indication that the proposed computerized technique is effective and is an encouraging sign. It should however be emphasized here that the findings from our studies are not conclusive as only fifteen datasets were used.

Table 6.4: Quantification results for left and right masseters.

Left Masseter		Right Masseter		Age Group	Ethnic Group
Test Set	*Volume (cm³)*	*Test Set*	*Volume (cm³)*		
1	23.51	1	24.54	30-40	Asian
2	30.56	2	31.89	20-30	Asian
3	18.92	3	18.53	20-30	European
4	30.49	4	31.05	30-40	Asian
5	19.64	5	17.42	20-30	European
6	23.00	6	21.97	40-50	Asian
7	28.91	7	27.41	20-30	Asian
8	26.97	8	24.16	20-30	Asian
9	25.37	9	25.83	20-30	Asian
10	32.07	10	29.44	20-30	Asian
11	23.31	11	22.30	40-50	Asian
12	26.29	12	25.41	30-40	Asian
13	29.54	13	30.08	20-30	Asian
14	28.53	14	27.22	20-30	Asian
15	26.34	15	25.76	20-30	Asian
Mean	**26.23**	*Mean*	**25.53**		
Standard deviation	**3.95**	*Standard deviation*	**4.26**		

Table 6.5: Quantification results for left and right lateral pterygoids.

Left Lateral Pterygoid		Right Lateral Pterygoid		Age Group	Ethnic Group
Test Set	*Volume (cm³)*	*Test Set*	*Volume (cm³)*		
1	8.56	1	8.95	30-40	Asian
2	9.38	2	9.58	20-30	Asian
3	7.86	3	7.69	20-30	European
4	8.86	4	9.29	30-40	Asian
5	7.93	5	8.24	20-30	European
6	8.23	6	8.11	40-50	Asian
7	8.82	7	9.21	20-30	Asian
8	8.16	8	8.78	20-30	Asian
9	8.81	9	8.46	20-30	Asian
10	8.89	10	9.20	20-30	Asian
11	8.05	11	8.21	40-50	Asian
12	7.93	12	8.79	30-40	Asian
13	9.03	13	9.22	20-30	Asian
14	8.89	14	9.52	20-30	Asian
15	8.59	15	9.43	20-30	Asian
Mean	**8.53**	*Mean*	**8.85**		
Standard deviation	**0.473**	*Standard deviation*	**0.582**		

Table 6.6: Quantification results for left and right medial pterygoids

Left Medial Pterygoid		Right Medial Pteryoid		Age Group	Ethnic Group
Test Set	*Volume (cm³)*	*Test Set*	*Volume (cm³)*		
1	9.45	1	9.54	30-40	Asian
2	10.21	2	10.51	20-30	Asian
3	8.58	3	8.34	20-30	European
4	10.3	4	10.98	30-40	Asian
5	8.77	5	8.76	20-30	European
6	8.85	6	8.92	40-50	Asian
7	9.98	7	10.38	20-30	Asian
8	9.78	8	9.51	20-30	Asian
9	9.14	9	10.12	20-30	Asian
10	10.21	10	10.68	20-30	Asian
11	8.51	11	8.30	40-50	Asian
12	9.60	12	9.78	30-40	Asian
13	10.23	13	10.59	20-30	Asian
14	9.92	14	10.28	20-30	Asian
15	9.62	15	9.78	20-30	Asian
Mean	**9.54**	*Mean*	**9.76**		
Standard deviation	**0.631**	*Standard deviation*	**0.859**		

Chapter 7

Conclusion

7.1   Overview of Achievements

- **Improved watershed algorithm with K-means clustering**

The concept and implementation of the novel technique, improved watershed algorithm with K-means clustering, is described in this thesis. Through comparative studies with other methods such as the conventional watershed algorithm and K-means clustering, it has been shown that the proposed method is capable of producing superior results.

The improved watershed technique [92, 93] was first proposed to address the main drawback of the conventional watershed technique, which is over-segmentation. The proposed algorithm differs from the conventional algorithm in that we perform thresholding on the gradient magnitude image to reduce the number of edge pixels. An important component in the improved watershed algorithm is post-segmentation merging of the partitions in the segmentation map formed by the watershed transform.

The experimental results demonstrate that the improved watershed algorithm can greatly reduce the amount of over-segmentation produced by the conventional watershed segmentation algorithm. To further reduce the problem of over-segmentation, the use of K-means clustering to obtain a coarse segmentation prior to the application of the improved watershed segmentation algorithm was proposed.

Experimental results obtained by applying the proposed improved watershed algorithm with K-means clustering to the segmentation of the masseter from 60 MR images indicate that the mean κ index achieved is greater than 90%, and that the segmentation maps have 98% fewer partitions than those formed by the conventional algorithm [94, 95].

- **Model-based approach for muscles segmentation from MR images**

A method for segmenting the masseters, lateral and medial pterygoids, which belong to the group of human masticatory muscles, from MR images is proposed in this thesis. Such method, to our best knowledge, is currently unavailable. In the process of designing the proposed method, a solution to the problem of providing good initializations to the GVF snake automatically was proposed. Without good initializations, the GVF snake does not provide good segmentations in the applications here.

Under the proposed method [96 – 98], by training the system using the spatial relationship between the head ROI and muscle ROI, the system is able to determine the muscle ROI in a study image automatically, instead of requiring human interaction. The soft tissue is approximately separated from the fat and bone through FCM with three clusters. In the resulting ROI, the muscles are present with the soft tissue. By checking for the overlap between the template and the regions in the ROI, we are able to remove the majority of the unwanted soft tissue. After checking for overlap with the template, small unwanted regions remaining in the muscle ROI are then removed through the use of connected components labelling. This gives us an initial segmentation of the muscle, which serves as initialization to the GVF snake.

The initialization process for the GVF snake is automatic. The initial segmentations serve as good initializations for the GVF snake. Since they are close to the actual boundaries of the muscles, relatively little iterations are required before the GVF snake converges. Our method to initialize the GVF snake proves to be good as we are able to obtain a mean κ better than 90% in 75 segmentation results. This is achieved despite the fact that clear and distinct boundaries might be unavailable between muscles and surrounding soft tissue. Furthermore, even though the model is 2D in nature, it is tolerant to a rotation of 15° and can be applied to two neighbouring slices superior and inferior to the reference slice [98]. This is an encouraging sign.

- **Segmentation using adaptive morphology**

Morphological operations such as opening and closing are commonly used in image processing. However, the appropriate size of the structuring element is often unknown. In our application here, the use of a fixed structuring element to morphologically separate the brain and muscle tissue is not advisable as this may cause excessive erosion to the muscle structure. Hence the use of adaptive morphology is proposed. This is found to be more appropriate.

In the proposed method for segmentation of the temporalis, we first check if the tissue on the left side of the ROI is connected to the soft tissue on the right side of the ROI. If they are, we apply morphological opening to the ROI with a circular structuring element of radius 1. If the brain tissue is still connected to the soft tissue on the right side, we apply morphological opening again but with the radius of the structuring element increased, by 1. The entire process is iterated until the brain tissue is separated

from the remaining soft tissue. This approach fits our work because in the temporalis ROI, the CSF is removed after range-constrained thresholding and there will be a demarcation between brain tissue and the remaining soft tissue. There may be some weak connections between them, and these are removed after applying the above adaptive morphological procedure.

- **Determination of dominant slices for patient-specific models**

A method for determining the dominant slices of the human masticatory muscles (masseter, lateral and medial pterygoids) in MR datasets of the head is proposed and implemented. The dominant slices for each muscle together capture the main features of the muscle. This method facilitates the building of accurate patient-specific human masticatory muscles models.

In our proposed method [99 – 101], the masticatory muscles in the training datasets were manually segmented by an expert radiologist. The locations of the dominant slices for each muscle were then determined from the training datasets using area- and shape-based criteria. Given a test dataset, segmentation of the muscles is carried out only on the dominant slices whose locations had been determined from the training sets. Shape-based interpolation is used to construct the complete muscle models from the 2D segmentations. The mean accuracy of the models built is as high as 92% when 10 dominant slices are being used, and drop to 78% when only 5 dominant slices are used. As the number of dominant slices is increased, the magnitude of the improvement in accuracy decreases.

Using the proposed method, the dominant slices for the masseters, lateral and medial pterygoids were determined and accurate muscles models were built. The muscles are anatomies of different shapes and sizes, and the fact that accurate models of them can be built using the proposed method is an indication that it is possibly applicable to other anatomies with different shapes and sizes. This is an encouraging sign.

- **3D human masticatory muscles segmentation**

A method for 3D segmentation of the human masticatory muscles has been proposed and implemented. The task is a challenging one due to the lack of strong edges between the muscles and surrounding soft tissue in MR images. This situation is more severe in some MR slices than others. Other problems pertaining to 3D human masticatory muscles segmentation include intensity inhomogeneity between slices and the variation in the size of the muscles in different slices which may result in higher error rate. The proposed method, which makes use of patient-specific masseter models and matching of distributions of pixels' intensity values both within the muscle volume and on its boundaries is capable of producing good segmentations [102]. As compared to the common practice where clinicians manually segment the muscles from all slices in the MR dataset which consists of 160 slices in the work here, the proposed method is much more practical and the amount of time clinicians can save is considerable.

7.2 Future Work

- **Platform for dental research**

An interactive environment, where MR scans are presented in tri-planar / 3D views, can be built to permit rapid quantification, visualization and interaction with structures

of human masticatory muscles from a database or input scans. Users can navigate around in the complex anatomical 3D spatial environment of the human head and relate regions in 2D slices to 3D space. An advantage this brings is that users can identify the positions where the muscles first and last appear with greater confidence. Comparisons between normal subjects and patients, using this environment, can possibly help identify facial asymmetry and ascertain extent of deformity.

- **Integration with facial models for pre-surgical simulations**

Using the techniques proposed in this thesis, the human masticatory muscles can be readily segmented when given a MR dataset. Studies can be carried out using the muscles segmentations to create statistical masticatory muscles models when a large number of datasets from a population becomes available.

After statistical masticatory muscles models have been built, efforts can then be made to integrate them with available pre-surgical facial models. It has been observed that the primary inadequacy with exisiting models is that they lack information on the actual location, shape and size of the human masticatory muscles. The integration task is challenging and will involve multi-modality registration techniques to register the human masticatory muscles models with the skull and surface information which can be extracted from CT data using the method presented earlier in this thesis. The different image resolution will hinder the registration task. After the integration is completed, finite element method (FEM) can be used to model dynamic motion, which will allow clinicians to simulate and predict the deformations of human masticatory muscles, as the bones (maxilla and mandible) are being adjusted.

References

[1] R.W. Brand and D.E. Isselhard. *Anatomy of orofacial structures*, St. Louis: Mosby, 1998.

[2] R. Koch, M. Gross, F. Caris, D. Buren, G. Frankhauser and Y. Parish. Simulating facial surgery using finite element models, *Proceedings of the 23rd annual conference on Computer Graphics and Interactive techniques*, pp. 421-428, 1996.

[3] Y. Aoki, S. Hashimoto, M. Terajima and A. Nakasima. Simulation of postoperative 3D facial morphology using a physics-based head model, *Visual Computer*, Vol. 17, No. 2, pp. 121-131, 2001.

[4] Y. Zhang, E.C. Prakash and E. Sung. A new physical model with multilayer architecture for facial expression animation using dynamic adaptive mesh, *IEEE Transactions on Visualization and Computer Graphics*, Vol. 10, No. 3, pp. 339-352, 2004.

[5] R. M. Koch, S.H.M. Roth, M.H. Gross, A.P. Zimmermann and H.F. Sailer. A framework for facial surgery simulation, *Proceedings of the 18th spring conference on Computer Graphics*, pp. 33-42, 2002.

[6] E. Gladilin, S. Zachow, P. Deuflhard and H.C. Hege. Anatomy and physics-based facial animation for craniofacial surgery simulations, *Medical & Biological Engineering & Computing*, Vol.42, No. 2, pp. 167-170, 2004.

[7] K. Maki, N. Inou, A. Takanishi and A.J. Miller. Computer-assisted simulations in orthodontic diagnosis and the application of a new cone beam X-ray computed tomography, *Journal of Orthodontics and Craniofacial Research*, Vol. 6, Suppl. 1, pp. 179-182, 2003.

[8] M. Meehan, M. Teschner and S. Girod. Three-dimensional simulation and prediction of craniofacial surgery, *Journal of Orthodontics and Craniofacial Research*, Vol. 6, No. 1, pp. 103-107, 2003.

[9] W.E. Lorensen and H.E. Cline. Marching cubes: a high resolution 3-D surface construction algorithm, *Proceedings of the 23rd annual conference on Computer Graphics and Interactive techniques*, pp. 163-189, 1987.

[10] J. Xia, N. Samman, R.W. Yeung, S.G. Shen, D. Wang, H.H. Ip and H. Tideman. Computer-assisted three-dimensional surgical planning and simulation. 3D soft tissue planning and prediction, *International Journal of Oral Maxillofacial Surgery*, Vol. 29, No. 4, pp. 250-258, 2000.

[11] T.Y. Wong, J.J. Fang, C.H. Chung, J.S. Huang and J.W. Lee. Comparison of 2 methods of making surgical models for correction of facial asymmetry, *International Journal of Oral Maxillofacial Surgery*, Vol. 63, No. 2, pp. 200-208, 2005.

[12] N. Noguchi and M. Goto. Computer simulation system for orthognathic surgery, *Journal of Orthodontics and Craniofacial Research*, Vol. 6, Suppl. 1, pp. 176-178, 2003.

[13] I.N. Bankman. *Handbook of Medical Imaging: Processing and Analysis*, Academic Press. 2000.

[14] P.C. Benington, J.E. Gardener and N.P. Hunt. Masseter muscle volume measured using ultrasonography and its relationship with facial morphology, *European Journal of Orthodontics*, Vol. 21, No. 6, pp. 659-670, 1999.

[15] T.K. Goto, K. Tokumori, Y. Nakamura, M. Yahagi, K. Yuasa, K. Okamura and S. Kanda. Volume changes in human masticatory muscles between jaw closing and opening, *Journal of Dental Research*, Vol. 81, No. 6, pp. 428-432, 2002.

[16] M. Takashima, N. Kitai, S. Murakami, S. Furukawa, S. Kreiborg and K. Takada. Volume and shape of masticatory muscles in patients with hemifacial microsomia, *The Cleft Palate-Craniofacial Journal*, Vol. 40, No.1, pp. 6-12, 2003.

[17] T.K. Goto, M. Yahagi, Y. Nakamura, K. Tokumori, G.E.J. Langenbach and K. Yoshiura. In vivo cross-sectional area of human jaw muscles varies with section location and jaw position, *Journal of Dental Research*, Vol. 84, No. 6, pp. 570-575, 2005.

[18] T.K. Goto, S. Nishida, M. Yahagi, G.E.J. Langenbach, Y. Nakamura, K. Tokumori, S. Sakai, H. Yabuuchi and K. Yoshiura. Size and orientation of masticatory muscles in patients with mandibular laterognathism, *Journal of Dental Research*, Vol. 85, No. 6, pp. 552-556, 2006.

[19] J. Teran, E. Sifakis, S.S. Blemker, T.H. Ng, C. Lau and R. Fedkiw. Creating and simulating skeletal muscle from the visible human data set, *IEEE Transactions on Visualization and Computer Graphics*, 2005, Vol. 11, No. 3, pp 317-328, 2005.

[20] P.R. Andresen, F.L. Bookstein, K. Conradsen, B.K. Ersboll, J.L. March, and S. Kreiborg. Surface-bounded growth modeling applied to human mandibles, *IEEE Transactions on Medical Imaging*, Vol. 19, No. 11, 2000.

[21] L. Vincent and P. Soille. Watersheds in digital spaces: an efficient algorithm based on immersion simulations, *IEEE Transactions on Pattern Analysis and Machine Intelligence*, Vol. 13, No. 6, pp. 583-598, 1991.

[22] H.T. Nguyen, M. Worring and R.V.D. Boomgaard. Watersnakes: Energy-driven watershed segmentation, *IEEE Transactions on Pattern Analysis and Machine Intelligence*, Vol. 25, No. 3, pp. 330-342, 2003.

[23] V. Grau, A.U.J. Mewes, M. Alcaniz, R. Kikinis and S.K. Warfield. Improved watershed transform for medical image segmentation using prior information, *IEEE Transactions on Medical Imaging*, Vol. 23, No. 4, 2004, pp 447-458, 2004.

[24] N. Ray, S.T. Acton, T. Altes, E.E. De Lange and J.R. Brookeman. Merging parametric active contours within homogeneous image regions for MRI-based lung segmentation, *IEEE Transactions on Medical Imaging*, Vol. 22, No. 2, pp. 189-199, 2003.

[25] C. Pluempitiwiriyawej, J.M. Moura, Y.J. Wu and C. Ho. STACS: New active contour scheme for cardiac MR image segmentation, *IEEE Transactions on Medical Imaging*, Vol. 24, No. 5, pp. 593-603, 2005.

[26] C. Xu and J.L. Prince. Snakes, Shapes, and Gradient Vector Flow, *IEEE Transactions on Image Processing*, Vol. 7, No. 3, pp. 359-369, 1998.

[27] T.Y. Lee and C.H. Lin. Feature guided shape-based image interpolation, *IEEE Transactions on Medical Imaging*, Vol. 21, No. 12, pp. 1479-1489, 2002.

[28] J. Liu and W.L. Nowinski. A hybrid approach to shape-based interpolation of stereotactic atlases of the human brain, *Neuroinformatics*, Vol. 4, No. 2, pp. 177-198, 2006.

[29] J. Yang, L.H. Staib and J.S. Duncan. Neighbor-constrained segmentation with level set based 3-D deformable models, *IEEE Transactions on Medical Imaging*, Vol. 23, No. 8, pp. 940-948, 2004.

[30] D. Freedman, R.J. Radke, T. Zhang, Y. Jeong, D.M. Lovelock and G.T.Y. Chen. Model-based segmentation of medical imagery by matching distributions, *IEEE Transactions on Medical Imaging*, Vol. 24, No. 3, pp. 281-292, 2005.

[31] M. Jiang, Q. Ji and B.F. McEwen. Model-based automated extraction of microtubules from electron tomography volume, *IEEE Transactions on Information Technology in Biomedicine*, Vol. 10, No. 3, pp. 608-617, 2006.

[32] P. Perona and J. Malik. Scale-space and edge detection using anisotropic diffusion, *IEEE Transactions on Pattern Analysis and Machine Intelligence*, Vol. 12, No. 7, pp. 629-639, 1990.

[33] J.J. Abrahams. Dental CT imaging: a look at the jaw, *Radiology*, Vol. 219, No. 2, pp. 334-345, 2001.

[34] K. Yeshwant, E.B. Seldin, J. Gateno, P. Everett, C.L. White, R. Kikinis, L.B. kaban and M.J. Troulis. Analysis of skeletal movements in mandibular distraction osteogenesis, *Journal of Oral and Maxillofacial Surgery*, Vol. 63, No. 3, pp. 335-340, 2005.

[35] A. Schramm, R. Schon, M. Rucker, E.L. Barth, C. Zizelmann and N.C. Gellrich. Computer-assisted oral and maxillofacial reconstruction, *Journal of Computing and Information Technology*, Vol. 14, No. 1, pp. 71-77, 2006.

[36] J. Gateno, J.J. Xia, J.F. Teichgraeber, A.M. Chritensen, J.J. Lemoine, M.A.K. Liebschner, M.J. Gliddon and M.E. Briggs. Clinical feasibility of computer-aided simulation (CASS) in the treatment of complex cranio-maxillofacial deformities, *Journal of Oral and Maxillofacial Surgery*, Vol. 65, No. 4, pp. 728-734, 2007.

[37] A.F. Ayoub, Y. Xiao, B. Khambay, J.P. Siebert and D. Hadley. Towards building a photo-realistic virtual human face for craniomaxillofacial diagnosis and treatment planning, *International Journal of Oral and Maxillofacial Surgery*, Vol. 36, No. 5, pp. 423-428, 2007.

[38] D.P. Kuehn, S.L. Ettema, M.S. Goldwasser, J.C. Barkmeier and J.M. Wachtel. Magnetic resonance imaging in the evaluation of occult submucous cleft palate, *Cleft Palate-Craniofacial Journal*, Vol. 38, No. 5, pp. 421-431, 2001.

[39] T. Taniyama, N. Kitai, Y. Iguchi, S. Murakami, M. Yanagi and K. Takada. Craniofacial morphology in a patient with simpson-golabi-behmel syndrome, *Cleft Palate-Craniofacial Journal*, Vol. 40, No. 5, pp. 550-555, 2003.

[40] S. Gerhard, T. Ennemoser, A. Rudisch and R. Emshoff. Condylar injury: magnetic resonance imaging findings of temporomandibular joint soft-tissue changes, *International Journal of Oral and Maxillofacial Surgery*, Vol. 36, No. 3, pp. 214-218, 2007.

[41] W.P. Smith, S. Prince and S. Phelan. The role of imaging and surgery in the management of vascular tumors of the masseter muscle, *Journal of Oral and Maxillofacial Surgery*, Vol. 63, No. 12, pp. 1746-1752, 2005.

[42] J.F. Schenck. The role of magnetic susceptibility in magnetic resonance imaging: MRI magnetic compatibility of the first and second kinds, *Medical Physics*, Vol. 23, No. 6, pp. 815-850, 1996.

[43] J.M. Links, L.S. Beach, B. Subramaniam, M.A. Rubin, J.G. Hennessey and A.L. Reiss. Edge complexity and partial volume effects, *Journal of Computer Assisted Tomography*, Vol. 22, No. 3, pp. 450-458, 1998.

[44] O. Dietrich, M.F. Reiser and S.O. Schoenberg. Artifacts in 3-T MRI: Physical background and reduction strategies, *European Journal of Radiology*, Vol. 65, No. 1, pp. 29-35, 2008.

[45] G. Eggers, M. Rieker, J. Fiebach, B. Kress, H. Dickhaus and S. Hassfeld. Geometric accuracy of magnetic resonance imaging of the mandibular nerve, *Dentomaxillofacial Radiology*, Vol. 34, No. 5, pp. 285-291, 2005.

[46] H.K. Wong, J.C.H. Goh and P.S. Goh. Paired cylindrical interbody cage fit and facetectomy in posterior lumbar interbody fusion in an asian population, *Spine*, Vol. 26, No. 5, pp. 572-577, 2001.

[47] C.-F. Westin, A. Bhalerao, H. Knutsson, and R. Kikinis. Using local 3D structure for segmentation of bone from computer tomography images, *Proceedings of the IEEE Computer Society Conference on Computer Vision and Pattern Recognition*, pp. 794-800, 1997.

[48] H.P. Ng, K.W.C. Foong, S.H. Ong and W.L. Nowinski. Towards construction of a 3D virtual human head for clinical purposes, *Proceedings of the 1st International Conference on Complex Medical Engineering*, pp. 297-301, 2005.

[49] P.K. Sahoo, S. Soltani, and A.K.C. Wong. A survey of thresholding techniques, *Computer Vision, Graphics, and Image Processing*, Vol. 41, pp. 233-260, 1988.

[50] N. Otsu. A threshold selection method from gray-level histograms, *IEEE Transactions on Systems Man and Cybernetics*, Vol. 9, No. 1, pp. 62-66, 1979.

[51] R. C. Gonzalez and R. E. Woods. Digital Image Processing, Addison-Wesley, pp. 419, 1992.

[52] A.B. Jani, C.A. Pelizzari, G.T.Y. Chen, J. Roeske, R.J. Hamilton, R.L. Macdonald, F. Bova, K.R. Hoffmann and P.A. Sweeney. Volume rendering quantification algorithm for reconstruction of CT volume-rendered structures, *IEEE Transactions on Medical Imaging*, Vol. 19, No. 1, pp. 12-24, 2000.

[53] K. Waters and D. Terzopoulos. A physical model of facial tissue and muscle articulation, *Proceedings of the 1st Conference on Visualization in Biomedical Computing*, pp. 77 – 82, 1990.

[54] M. Chabanas, V. Luboz, Y. Payan. Patient specification finite element model of the face soft tissues for computer-assisted maxillofacial surgery, Medical Image Analysis, Vol. 7, No. 2, pp.131-151, 2003.

[55] C. Lee, S. Huh, T.A. Ketter and M. Unser. Unsupervised connectivity-based thresholding segmentation of midsagittal brain MR images, *Computers in Biology and Medicine*, Vol. 28, No. 3, pp. 309-338, 1998.

[56] D.Y. Kim and J.W. Park. Connectivity-based local adaptive thresholding for carotid artery segmentation using MRA images, *Image and Vision Computing*, Vol. 23, No. 14, pp. 1277-1287, 2005.

[57] Q.M. Hu, Z. Hou and W.L. Nowinski. Supervised range-constrained thresholding, *IEEE Transactions on Image Processing*, Vol. 15, No. 1, pp. 228-240, 2006.

[58] B. Vasilic and F.W. Wehrli. A novel local thresholding algorithm for trabecular bone volume fraction mapping in the limited spatial resolution regime of in vivo MRI, *IEEE Transactions on Medical Imaging*, Vol. 24, No. 12, pp. 1574-1585, 2005.

[59] S. Shiffman, G.D. Rubin, and S. Napel. Medical image segmentation using analysis of isolable-contour maps, *IEEE Transactions on Medical Imaging*, Vol. 19, No. 11, pp. 1064-1074, 2000.

[60] M. Kass, A. Witkin, and D. Terzopoulos. Snakes: Active contour models, *International Journal of Computer Vision*, Vol. 1, No. 4, pp. 321-331, 1987.

[61] J. Tang, S. Millington, S.T. Acton, J. Crandall and S. Hurwitz. Surface extraction and thickness measurement of the articular cartilage from MR images using directional gradient vector flow snakes, *IEEE Transactions on Biomedical Engineering*, Vol. 53, No. 5, pp. 896-907, 2006.

[62] J. Xu, O. Chutatape and P. Chew. Automated optic disk boundary detection by modified active contour model, *IEEE Transactions on Biomedical Engineering*, Vol. 54, No. 3, pp. 473-482, 2007.

[63] J.B.T.M. Roerdink and A. Meijster. The watershed transform: Definitions, algorithms and parallelization strategies, *Fundamental Informaticae*, Vol. 41, pp. 187-228, 2000.

[64] J.E. Cates, R.T. Whitaker and G.M. Jones. Case study: An evaluation of user-assisted hierarchical watershed segmentation, *Medical Image Analysis*, Vol. 9, No. 6, pp. 566-578, 2005.

[65] H. Tek and H.C. Aras. Local watershed operators for image segmentation, *Proceedings of the 7th International Conference on Medical Image Computing and Computer-Assisted Intervention, MICCAI*, pp. 127-134, 2004.

[66] R. Rodriguez, T.E. Alarcon and O. Pacheco. A new strategy to obtain robust markers for blood vessels segmentation by using the watersheds method, *Computers in Biology and Medicine*. Vol. 35, No. 8, pp. 665-686, 2005.

[67] D.L. Pham and J.L. Prince. Adaptive fuzzy segmentation of magnetic resonance images, *IEEE Transactions on Medical Imaging*. Vol. 18, No. 9, pp. 737-752, 1999.

[68] M.N. Ahmed and S.M. Yamany. A modified fuzzy C-means algorithm for bias field estimation and segmentation of MRI data, *IEEE Transactions on Medical Imaging*. Vol. 21, No. 3, pp. 193-199, 2002.

[69] S. Shen, W. Sandham, M. Granat and A. Sterr. MRI fuzzy segmentation of brain tissue using neighborhood attraction with neural-network optimization, *IEEE Transactions on Information Technology in Biomedicine*. Vol. 9, No. 3, pp. 459-467, 2005.

[70] J.C. Bezdek, L.O. Hall and L.P. Clarke. Review of MR image segmentation techniques using pattern recognition, *Medical Physics*. Vol. 20, No. 4, pp. 1033-1048, 1993.

[71] T. Kanungo, D.M. Mount, N.S. Netanyahu, C.D. Piatko, R. Silverman and A.Y. Wu. An efficient K-means clustering algorithm: analysis and implementation, *IEEE Transactions on Pattern Analysis and Machine Intelligence*. Vol. 24, No. 7, pp. 881-892, 2002.

[72] M. Laszio and S. Mukherjee. A genetic algorithm using hyper-quadtrees for low-dimensional K-means clustering, *IEEE Transactions on Pattern Analysis and Machine Intelligence*. Vol. 28, No. 4, pp. 533-543, 2006.

[73] C.W. Chen, J. Luo and K.J. Parker. Image segmentation via adaptive K-mean clustering and knowledge based morphological operations with biomedical applications, *IEEE Transactions on Image Processing*. Vol. 7, No. 12, pp. 1673-1683, 1998.

[74] V.K. Leemput, F. Maes, D. Vandermeulen and P. Suetens. Automated model-based tissue classification of MR images of the brain, *IEEE Transactions on Medical Imaging*, Vol. 18, No. 10, pp. 897-908, 1999.

[75] A.C.S. Chung. Vascular segmentation of phase contrast magnetic resonance angiograms based on statistical mixture modeling and local phase coherence, *IEEE Transactions on Medical Imaging*, Vol. 23, No. 12, pp. 1490-1507, 2004.

[76] M.S. Hassouna, A.A. Farag, S. Hushek and T. Moriarty. Cerebrovascular segmentation from TOF using stochastic models, *Medical Image Analysis*, Vol. 10, No. 1, pp. 2-18, 2006.

[77] Y. Qiao, Q.M. Hu, G.Y. Qian, S.H. Luo and W.L. Nowinski. Thresholding based on variance and intensity contrast, *Pattern Recognition*, Vol. 40, No. 2, pp. 596-608, 2007.

[78] J.C. Bezdek. *Pattern recognition with fuzzy objective function algorithm*, New York, Plenum, 1981.

[79] Q. Hu, G. Qian and W.L. Nowinski. Fast connected-component labelling in three-dimensional binary images based on iterative recursion, *Computer Vision and Image Understanding*, Vol. 99, No. 3, pp. 414-434, 2005.

[80] J. Canny. A computational approach to edge detection, *IEEE Transactions on Pattern Analysis and Machine Intelligence*, Vol. 8, No. 4, pp. 679-698, 1986.

[81] Q. Hu and W.L. Nowinski. A rapid algorithm for robust and automatic extraction of the midsagittal plane of the human cerebrum from neuroimages based on local symmetry and outlier removal, *NeuroImage*, Vol. 20, No. 4, pp. 2153-2165, 2003.

[82] K. Fukunaga and D.M. Hummels. Leave-one-out procedures for nonparametric error estimates, *IEEE Transactions on Pattern Analysis and Machine Intelligence*, Vol. 11, No. 4, pp. 421-423, 1989.

[83] Z.J. Hou, Q.M. Hu and W.L. Nowinski. On minimum variance thresholding, *Pattern Recognition Letters*, Vol. 27, No. 14, pp. 1732-1743, 2006.

[84] D.L. Pham, J.L. Prince, A.P. Dagher and C. Xu. An automated technique for statistical characterization of brain tissues in magnetic resonance image, *International Journal of Pattern Recognition and Artificial Intelligence*, Vol. 11, No. 8, pp. 1189-1211, 1997.

[85] Y. Ge, J.M. Fitzpatrick, B.M. Dawant, J. Bao, R.M. Kessler and R.A. Margolin. Accurate localization of cortical convolutions in MR brain images, *IEEE Transactions on Medical Imaging*, Vol. 15, No. 4, pp. 418-428, 1996.

[86] H.P. Ng, S.H. Ong, K.W.C. Foong, P.S. Goh and W.L. Nowinski. Automatic segmentation of muscles of mastication from magnetic resonance images using prior knowledge, *Proceedings of the 28th Annual International Conference IEEE Engineering in Medicine and Biology Society*, pp. 5294-5297, 2006.

[87] W.L. Nowinski, J. Liu and A, Thirunavuukarasuu. Quantification of three-dimensional inconsistency of the subthalamic nucleus in the Schaltenbrand-Wahren brain atlas, *Stereotactic and Functional Neurosurgery*, Vol. 84, No. 1, pp. 46-55, 2006.

[88] A.X. Falcao, J.K. Udupa and F.K. Miyazawa. An ultra-fast user-steered image segmentation paradigm: live wire on the fly, *IEEE Transactions on Medical Imaging*, Vol. 19, No. 1, pp. 55-62, 2000.

[89] A. Lundervold, N. Duta, T. Taxt and A.K. Jain. Model-guided segmentation of corpus callosum in MR images, *Proceedings of IEEE Conference on Computer Vision and Pattern Recognition*, pp. 231-237, 1999.

[90] M. Bello, T. Ju, J. Carson, J. Warren, W. Chiu and I.A. Kakadiaris. Learning-based segmentation framework for tissue images containing gene expression data, *IEEE Transactions on Medical Imaging*, Vol. 26, No. 5, pp. 728-744, 2007.

[91] D. Seghers, D. Loeckx, F. Maes, D. Vandermeulen and P. Suetens. Minimal shape and intensity cost path segmentation, *IEEE Transactions on Medical Imaging*, Vol. 26, No. 8, pp. 55-62, 2007.

[92] H.P. Ng, K.W.C. Foong, S.H. Ong and W.L. Nowinski. Watershed transform for the segmentation of MRI images, *Proceedings of the 2nd International Conference Advanced Digital Technology in Head and Neck*, Paper No. 82, 2005.

[93] H.P. Ng, S.H. Ong, K.W.C. Foong, and W.L. Nowinski. An improved watershed algorithm for medical image segmentation, *Proceedings of the 12th International Conference on Biomedical Engineering*, 2005.

[94] H.P. Ng, S.H. Ong, K.W.C. Foong, P.S. Goh and W.L. Nowinski. Medical image segmentation using K-means clustering and improved watershed algorithm, *Proceedings of the 7th IEEE Southwest Symposium on Image Analysis and Interpretation*, pp. 61-65, 2006.

[95] H.P. Ng, S.H. Ong, K.W.C. Foong, P.S. Goh and W.L. Nowinski. Masseter segmentation using an improved watershed algorithm with unsupervised classification, *Computers in Biology and Medicine*, 2007. (Accepted)

[96] H.P. Ng, S.H. Ong, P.S. Goh, K.W.C. Foong, and W.L. Nowinski. Template-based automatic segmentation of facial muscle using prior knowledge, *Proceedings of the 7th IEEE Southwest Symposium on Image Analysis and Interpretation*, pp. 208-212, 2006.

[97] H.P. Ng, S.H. Ong, K.W.C. Foong, P.S. Goh and W.L. Nowinski. Automatic segmentation of muscles of mastication from magnetic resonance images using prior knowledge, *Proceedings of the 18th International Conference on Pattern Recognition*, pp. 968-971, 2006.

[98] H.P. Ng, S.H. Ong, Q. Hu, K.W.C. Foong, P.S. Goh and W.L. Nowinski. Muscles of mastication model-based MR image segmentation, *International Journal of Computer Assisted Radiology and Surgery*, Vol. 1, No. 3, pp. 137-148, 2006.

[99] H.P. Ng, K.W.C. Foong, S.H. Ong, J. Liu, P.S. Goh and W.L. Nowinski. Shape determinative slice localization for patient-specific masseter modeling using shape-based interpolation, *International Journal of Computer Assisted Radiology and Surgery*, Vol. 2, Suppl. 1, pp. 398-400, 2007.

[100] H.P. Ng, K.W.C. Foong, S.H. Ong, J. Liu, P.S. Goh and W.L. Nowinski. A study on shape determinative slices for the masseter muscle, *Proceedings of the 29th Annual International Conference IEEE Engineering in Medicine and Biology Society*, pp. 5585-5588, 2007.

[101] H.P. Ng, S.H. Ong, K.W.C. Foong, J. Liu, S. Huang, P.S. Goh and W.L. Nowinski, "Salient features useful for the accurate segmentation of masticatory muscles from minimum slice subsets of magnetic resonance images", *Machine Vision and Applications*, 2007. (under revision)

[102] H.P. Ng, S.H. Ong, J. Liu, S. Huang, K.W.C. Foong, P.S. Goh and W.L. Nowinski, "3D segmentation and quantification of a masticatory muscle from MR data using patient-specific models and matching distributions", *Journal of Digital Imaging*, 2008. (in press)

Awards and Publications

Awards

1. *Outstanding Paper Award* awarded by 12th ICBME

   H.P. Ng, K.W.C. Foong, S.H. Ong, P.S. Goh and W.L. Nowinski,

   "Moving towards the construction of a highly realistic pre-surgical facial model",

   12th International Conference on Biomedical Engineering, December, 2005.

2. *Certificate of Achievement* awarded by Pattern Recognition and Machine Intelligence Association (PREMIA)

   H.P. Ng, S.H. Ong, K.W.C. Foong, P.S. Goh and W.L. Nowinski,

   "Automatic segmentation of muscles of mastication from magnetic resonance images using prior knowledge"

   18th International Conference on Pattern Recognition, August, 2006.

International Journal Papers

3. H.P. Ng, S.H. Ong, Q. Hu, K.W.C. Foong, P.S. Goh and W.L. Nowinski, "Muscles of mastication model-based MR image segmentation", *International Journal of Computer Assisted Radiology and Surgery*, Vol. 1, No. 3, pp. 137-148, 2006.

4. H.P. Ng, Q.M. Hu, S.H. Ong, K.W.C. Foong, P.S. Goh and W.L. Nowinski, "Segmentation of the temporalis from MR data", *International Journal of Computer Assisted Radiology and Surgery*, Vol. 2, No. 1, pp. 19-30, 2007.

5. H.P. Ng, K.W.C. Foong, S.H. Ong, J. Liu, P.S. Goh and W.L. Nowinski, "Shape determinative slice localization for patient-specific masseter modeling using shape-based interpolation", *International Journal of Computer Assisted Radiology and Surgery*, Vol. 2, Suppl. 1, pp. 398-400, 2007.

6. H.P. Ng, S.H. Ong, K.W.C. Foong, P.S. Goh and W.L. Nowinski, "Masseter segmentation using an improved watershed algorithm with unsupervised classification", *Computers in Biology and Medicine*, Vol. 38, No. 2, pp. 171-184, 2008.

7. H.P. Ng, S.H. Ong, J. Liu, S. Huang, K.W.C. Foong, P.S. Goh and W.L. Nowinski, "3D segmentation and quantification of a masticatory muscle from MR data using patient-specific models and matching distributions", *Journal of Digital Imaging*, 2008. (in press)

8. H.P. Ng, K.W.C. Foong, S.H. Ong, P.S. Goh, S. Huang, J. Liu and W.L. Nowinski, "Quantitative analysis of human masticatory muscles using magnetic resonance imaging", *Dentomaxillofacial Radiology*, 2008. (in press)

9. H.P. Ng, S.H. Ong, K.W.C. Foong, J. Liu, S. Huang, P.S. Goh and W.L. Nowinski, "Salient features useful for the accurate segmentation of masticatory muscles from minimum slice subsets of magnetic resonance images", *Machine Vision and Applications*, 2007. (under revision)

International Conference Papers

10. H.P. Ng, K.W.C. Foong, S.H. Ong and W.L. Nowinski, "Watershed transform for the segmentation of MRI images", *2nd International Conference Advanced Digital Technology in Head and Neck*, Banff, Alberta, Canada, Paper No. 82, March, 2005.

11. H.P. Ng, K.W.C. Foong, S.H. Ong and W.L. Nowinski, "Towards construction of a 3D virtual human head for clinical purposes", *1ˢᵗ International Conference on Complex Medical Engineering*, Takamatsu, Japan, pp. 297-301, May, 2005.

12. H.P. Ng, S.H. Ong, K.W.C. Foong, and W.L. Nowinski, "An improved watershed algorithm for medical image segmentation", *12ᵗʰ International Conference on Biomedical Engineering*, Singapore, Proceedings on CD-ROM, December, 2005.

13. H.P. Ng, K.W.C. Foong, S.H. Ong and W.L. Nowinski, "Moving towards the construction of a highly realistic pre-surgical facial model", *12ᵗʰ International Conference on Biomedical Engineering*, Singapore, Proceedings on CD-ROM, December, 2005.

14. H.P. Ng, S.H. Ong, P.S. Goh, K.W.C. Foong, and W.L. Nowinski, "Template-based automatic segmentation of facial muscle using prior knowledge", *7ᵗʰ IEEE Southwest Symposium on Image Analysis and Interpretation*, Denver, Colorado, USA, pp. 208-212, March, 2006.

15. H.P. Ng, S.H. Ong, K.W.C. Foong, P.S. Goh and W.L. Nowinski, "Medical image segmentation using K-means clustering and improved watershed algorithm", *7ᵗʰ IEEE Southwest Symposium on Image Analysis and Interpretation*, Denver, Colorado, USA, pp. 61-65, March, 2006.

16. H.P. Ng, S.H. Ong, K.W.C. Foong, P.S. Goh and W.L. Nowinski, "Automatic segmentation of muscles of mastication from magnetic resonance images using prior knowledge", *18ᵗʰ International Conference on Pattern Recognition*, Hong Kong, pp. 968-971, August, 2006.

17. H.P. Ng, S.H. Ong, K.W.C. Foong, P.S. Goh and W.L. Nowinski, "Knowledge-driven 3-D extraction of the masseter from MR data", *28th Annual International Conference IEEE Engineering in Medicine and Biology Society*, New York, USA, pp. 5294-5297, August, 2006.

18. H.P. Ng, K.W.C. Foong, S.H. Ong, P.S. Goh and W.L. Nowinski, "Medical image segmentation using feature-based GVF snake", *29th Annual International Conference IEEE Engineering in Medicine and Biology Society*, Lyon, France, pp. 800-803, August, 2007.

19. H.P. Ng, K.W.C. Foong, S.H. Ong, J. Liu, P.S. Goh and W.L. Nowinski, "A study on shape determinative slices for the masseter muscle", *29th Annual International Conference IEEE Engineering in Medicine and Biology Society*, Lyon, France, pp. 5585-5588, August, 2007.